UNIVERSITY OF CALIFORNIA SAN DIEGO

Surveying the metastatic single cell state

A dissertation submitted in partial satisfaction of the requirements for the degree Doctor of Philosophy

in

Biology

by

Andres Jose Nevarez

Committee in charge:

Professor Nan Hao, Chair
Professor Gurol Seul
Professor Wei Wang
Professor Dong-Er Zhang
Professor Kun Zhang

2022

The Dissertation of Andres Jose Nevarez is approved, and it is acceptable in quality and form for publication on microfilm and electronically.

University of California San Diego

2022

DEDICATION

Without the support of my partner, Alishia, the support of my parents, Pilar and Hortencia, and my dogs, Bane, Ralph, Ruger, Lupita, and Maxx, this would not have been possible. This is for my children Leia and Andres and for the young Latin children looking to see themselves as scientists.

EPIGRAPH

"Intentaron enterrarnos. No sabían que éramos semillas."

"They tried to bury us. They did not know we were the seeds."

Aztec Proverb

TABLE OF CONTENTS

LIST OF FIGURES

ACKNOWLEDGEMENTS

I would like to acknowledge Professor Nan Hao for his support as the chair of my committee. Thank you for seeing in me what at times I could not see and providing the support and enthusiasm for me to see it as well.

Chapter 1, in part is currently being prepared for submission for publication of the material. Nevarez, Andres; Hao, Nan. The dissertation author was the primary investigator and author of this material.

Chapter 2, in full, is a reprint of the material as it appears in Cell Systems 2021. Zaritsky, Assaf*; Jamieson, Andrew R.*; Welf, Erik S.*; Nevarez, Andres*; Cillay, Justin; Eskiocak, Ugur; Cantarel, Brandi L.; Danuser, G. Interpretable deep learning uncovers cellular propertiesin label-free live cell images that are predictive of highly metastatic melanoma. The dissertation author was the co-primary investigator and author of this paper.

Chapter 3, in part is currently being prepared for submission for publication of the material. Nevarez, Andres; Mudla, Anusorn; Zabary, Yishaia; Hao, Nan. The dissertation author was the primary investigator and author of this material.

VITA

2014 B.S. in Biology, California State University Fresno

2018 M.S. in Biomedical Sciences, University of Texas Southwestern Medical Center Dallas

2022 Ph.D. in Biology, University of California San Diego

PUBLICATIONS

A. Zaritsky*, AR. Jamieson*, ES. Welf*, A. Nevarez*, Justin Cillay, Ugur Eskiocak, Brandi L. Cantarel G. Danuser. Interpretable deep learning uncovers cellular propertiesin label-free live cell images that are predictive of highly-metastatic melanoma. *Cell Systems. 2021. Vol 12.* (*equal contribution)

A Nevarez, and N. Hao. Quantitative cell imaging approaches to metastatic state profiling. BioRxiv. 2022.

A Nevarez, A. Mudla, Y. Zabary, and N. Hao. Dissection the connection between Telomerase promoter mutations and metastatic potential. BioRxiv. 2022.

FIELDS OF STUDY

Major Field: Biology

Studies in Quantitative Biology

Professors Dr. Nan Hao

ABSTRACT OF THE DISSERTATION

Surveying the metastatic single cell state

by

Andres Jose Nevarez

Doctor of Philosophy in Biology

University of California San Diego, 2022

Professor Nan Hao, Chair

Metastases arise from a small subset of cells, less than 1%, in the primary tumor. Metastasis is responsible for most cancer-related deaths and plays a significant role in therapy resistance, yet this hallmark of cancer is poorly understood. Metastasis is not determined by a genetic coding pattern among metastatic tumors pan-cancer. Identifying roots of metastatic potential is crucial for long-term research for the field; to this end, we must identify metastatic phenotypes for targeted therapy. Instead of the therapies we have now, metastatic cells can still avoid. First, we employ a generative neural network in combination with supervised machine learning

to classify patient-derived melanoma xenografts as "efficient" or "inefficient" metastatic, validate predictions regarding melanoma cell lines with unknown metastatic efficiency in mouse xenografts, and use the network to generate in silico cell images that amplify the critical predictive cell properties. These exaggerated images unveiled metastatic phenotypes of pseudopodial extensions and increased light scattering as hallmark properties of metastatic cells. We found from our mouse experiments that the metastatic melanoma samples with TPMs had increased metastasis in the mice and were predicted to have increased metastatic potential from our deep learned model. Recently, sequencing the non-coding regions of patient metastatic tumors reveals two monoallelic TPMs, C228T and C250T. TPMs are found in the primary tumor but become highly enriched in metastatic tumor sites suggesting a functional role of the TPMs in metastatic potential. To determine the functional role of TPMs in metastasis, we have taken a phenotypic-driven interrogation. We have shown through bioinformatic analysis that C250T TPM has increased metastatic potential and penetrance in mice studies. We observed that TPMs increase the collective cell migration rate and distance with significant spatiotemporal features. We highlighted the increased gene expression heterogeneity due to the TPMs. We have shown differences between the TPMs and WT through machine learning using imaging cytometry focusing on morphological and

light scattering features. This shows the trend that C250T has an advantage over C228T and WT, while C228T has an advantage over WT Telomerase in metastatic tumors.

Chapter 1

Quantitative cell imaging approaches to metastatic state profiling

Andres J. Nevarez[1,2], and Nan Hao[1]

[1]Section of Molecular Biology, Division of Biological Sciences, University of California SanDiego, 9500 Gilman Drive, La Jolla, CA 92093, USA

[2]@technicolordres

Keywords: metastasis, cellular morphology, quantitative imaging, light microscopy, machine learning, deep learning

Abstract

Genetic heterogeneity of metastatic dissemination has proven challenging to identify exploitable markers of metastasis. Cellular morphology is a robust readout of cellular state due to the connections of the underlying complex signaling pathways. Recent advancements in quantitative cellular imaging have allowed the detection of subtle morphological phenotype changes that would be missed by human operators specific to metastasis. This review focuses on the recent developments in using machine and deep learning to gain more information about the metastatic cell state using light microscopy. We

describe the latest studies using quantitative cell imaging approaches to identify cell appearance-based metastatic patterns. We offer these quantitative cancer biologists can use these frameworks to work backward toward exploitable hidden drivers in the metastatic cascade.

Cannot grind and find them all: Genomics hits the metastatic wall

While we have made enormous progress regarding our understanding of cancer, it is still a leading cause of death worldwide. The cause of this high lethality is primarily due to the metastatic stage of the disease; metastasis occurs when cells from the primary tumor leave the local environment and colonize a distant organ (Chiang and Massagué 2008; Hanahan and Weinberg 2011; Reddy et al. 2012; Bogenrieder and Herlyn 2003; Gupta and Massagué 2006; Dillekås et al. 2016). Metastasis, and therefore therapy resistance, is the last frontier of cancer treatment; metastasis and therapy-resistant cells share many common properties (Fares et al. 2020). Nevertheless, less than 1% of the cells from the primary location can create tumors in distant organs. While metastatic cells may be rare events, they possess extraordinary abilities to survive an onslaught of insults that the cells must endure disseminating, colonizing, and thriving in a new microenvironment. Either a single "leader" migratory cell or clusters of migratory cells define the initial invasion (Cheung and Ewald 2016;

Padmanaban et al. 2019). The cells must adapt to an anchorless mobile state (Adeshakin et al. 2021) and navigate the surrounding microenvironment. They may enter the circulatory and must withstand shear stress due to blood pressure (Huang et al. 2018) and enter drainage sits such as the lymphatic systems (Bockhorn, Jain, and Munn 2007; Reymond, d'Água, and Ridley 2013; Friedl and Alexander 2011). Then the cells need to adapt to immune surveillance (Janssen et al. 2017) and numerous environmental changes in the new location (Baghban et al. 2020). Metastatic cells must possess cell properties that are entirely different from their primary, stationary counterparts. This way, metastatic cells adapt to evolutionary pressures by creating polyclonal populations, some of which survive each stressor (Cheung et al. 2016; Kok et al. 2021; Lo et al. 2020) to thrive in distinct niches ultimately (Tasdogan et al. 2020; Piskounova et al. 2015; Gal et al. 2015) from the primary tumor site. Due to clonal and genetic heterogeneity (Marusyk et al. 2014; Yates and Campbell 2012; Calbo et al. 2011), the seed and soil hypothesis (Paget 1889), and the disputes in acquired or somatic mutations relation to metastatic ability (Bernards and Weinberg 2002; Ramaswamy et al. 2003; Van't Veer et al. 2002), there is a debate on the genomic etiology of metastasis. Surprisingly, the deluge of mutations from genomic studies has landed on stereotypical metastatic signaling states (Klein 2009) reminiscent of the Waddington landscape

(Waddington 1959), although not converging on the metastatic target pathway. The landscape has led the field to use phenotypic-driven interrogations of metastasis to work towards identifying the hidden drivers in the metastatic cell state.

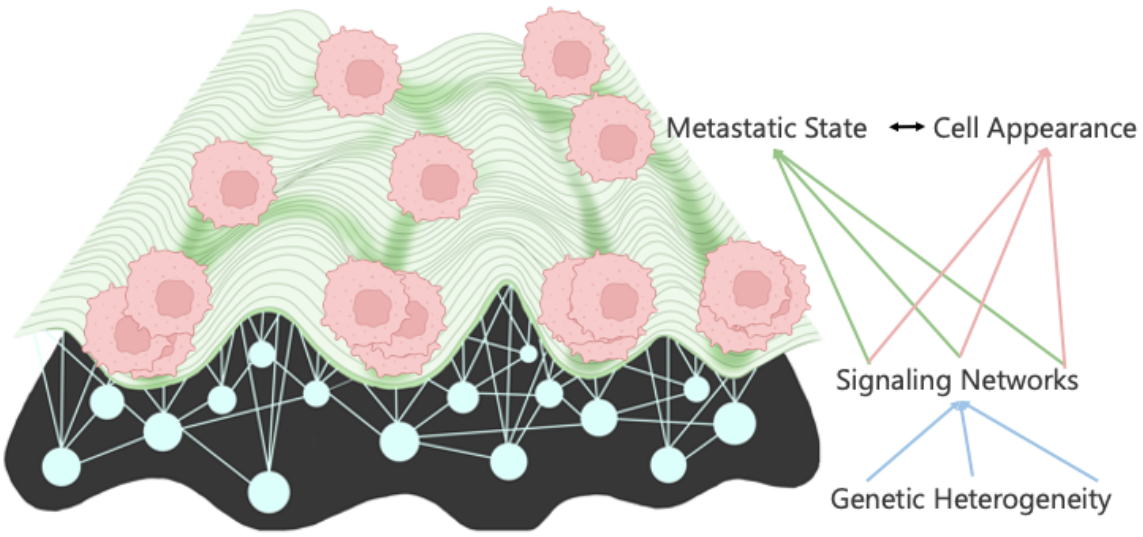

Figure 1.1 Schematic of metastatic landscape connects cell appearance through the underlying signaling networks determined by the underlying various mutations.

Appearances can be revealing

Subtle changes in metastatic cell states should manifest in detectable phenotypic changes (**Fig 1.1**). The subtle differences are due to the morphological connection to the cytoskeleton changes necessary for invasion in the metastatic cascade. Initially, these changes were quantified through static shape morphometrics and connected to changes in metastatic potential. Cell appearance is a reliable monitor of cell signaling

pathways (Yin et al. 2013; Bakal et al. 2007; Gordonov et al. 2016; Goodman and Carpenter 2016; Pascual-Vargas et al. 2017; Scheeder, Heigwer, and Boutros 2018; Sero and Bakal 2017) due to the strong connection to the cytoskeleton (Moujaber and Stochaj 2020). The strong relationships allow for a readout of metastatic expression profiles (Nguyen et al. 2016) and a cell's invasion ability (Minn et al. 2005). Recent studies have shown explicitly that cell appearance phenotypes have a solid connection to the metastatic phenotype (Lyons et al. 2016; Cooper et al. 2015; Wu et al. 2020). Morphological changes to identify invasive cancers stem from recognizing the epithelial to mesenchymal transition (EMT) (Lu and Kang 2019; Li and Balazsi 2018). Not only this, but pathologists often see gross morphological changes from primary to metastatic site biopsy samples, which allow for disease staging and grading (Lee et al. 2020). This review highlights studies that push forward the morphological analysis of metastatic cells and offers an experimental and analytical platform on which others can build their investigations, such as quantitative metastatic assays for probing the metastatic single-cell state.

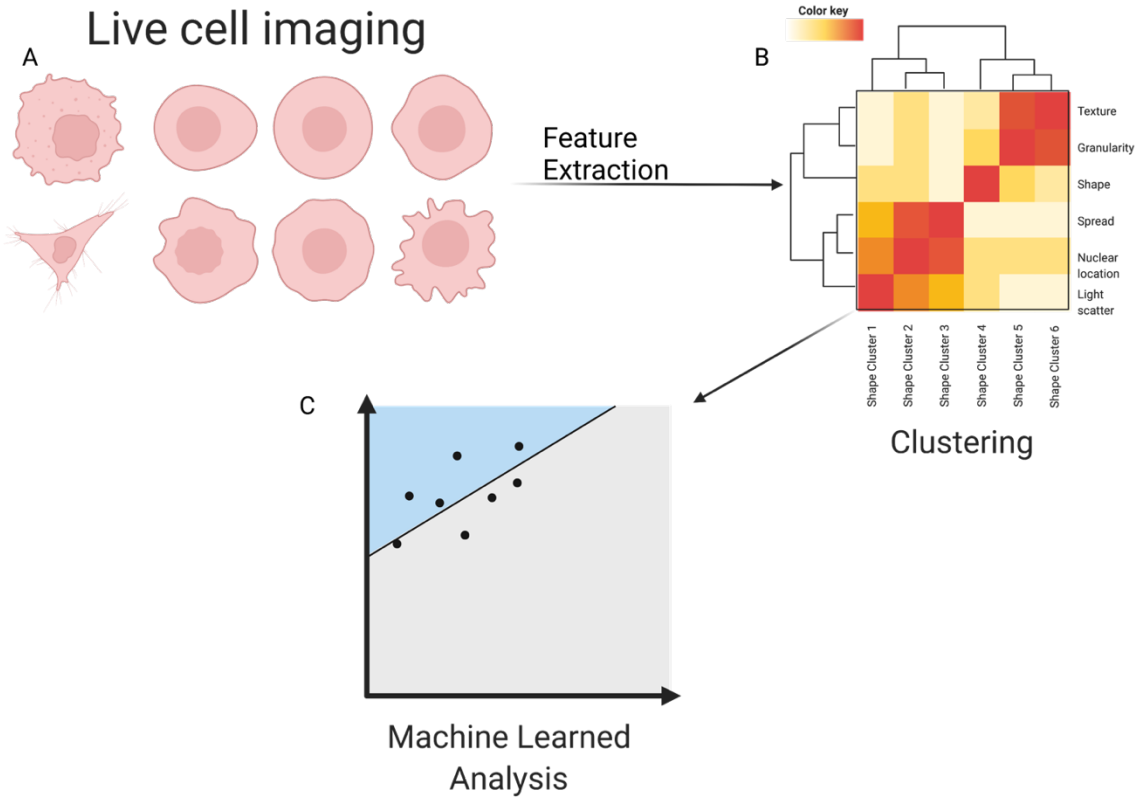

Figure 1.2 Machine learning of live cell imaging for metastatic classification. **(A)** Cell appearance from live-cell imaging quantified through supervised feature extraction, consisting of dozens of features that describe the cell appearance in many ways. Often these are clustered **(B)** into classes as input for a machine-learned model for classification **(C)**.

In the beginning, there were shapes: two-dimensional cell morphology and machine learning to classify metastatic cell state

Using two-dimensional (2D) live-cell imaging (**Fig 1.2A**), engineered features to describe metastatic cells (**Fig 1.2B**), and machine learning (**Fig 1.2C**) has taught us the value of cell appearance and its relation to metastatic ability. Recently the role of mechanotransduction's effect on metastasis as readout by 2D cell shape has shown to be an opportunistic avenue to assay metastatic potential (Riehl et al. 2021; Holenstein et al.

2019). Lyons et al. showed a deep connection between shape and metastatic potential compared to paired non-metastatic parental cells (Lyons et al. 2016). They investigated the effect of three different surfaces with varying hydrophobicity; glass detergent washed and air-dried, glass acid-etched and air-dried, and last, a siliconized ethanol-treated surface. Using four paired osteosarcomas, one with low metastatic potential and one with high metastatic potential from the same cell lineage. They showed that metastatic cells display different morphometric features using twenty-nine cellular and nuclear shape features. We must note that they focused on interpretable geometric shape features and not expansion shape features. They distilled these twenty-nine shape features into five morphological properties: projected cell size, cell roundness versus elongation, shape variability, nuclear size, and nuclear shape. They noted that high metastatic potential cells differ from their low potential counterparts in projected cell area and volume, then experimentally validated in vivo. Examining only the nuclear shape features showed no clear low versus high metastatic potential trends. Using only a single cellular feature highlights the pitfalls of using one morphometric as a classification tool, especially with prospects for clinical applications. However, they overcome this using machine learning feeding all shape features into a multilayer perceptron to classify cells. They showed their classifier had good accuracy against high and low cells from the same

lineages across cell surfaces and aggregate classes such as high versus low metastatic potential. This early work, and others like it, laid the foundation for computer vision and machine learning techniques to investigate metastatic cells.

Wu and company have repeatedly continued the exploration of shape features in 2D. Building upon their work in pancreatic ductal adenocarcinoma (Wu et al. 2015), they investigated the heredity of morphological traits in single-cell clones (SCC) of metastatic breast cancer cell lines. They found that each clone displayed a distinct morphology from which they investigated 14 SCC and their matched parental cell line. The 14 SCC cell morphology was described by extracting two hundred and fifteen cellular and nuclear morphometrics and using unsupervised clustering methods were distilled to seven distinct morphological profiles. Within the clones, there was morphological heterogeneity, albeit at a much lower degree, compared to the parental line indicating there are heritable morphological traits. With these quantitative morphologies relating to cell appearance, they sought to see how the different morphologies affect metastatic potential in vivo. They implanted each of the seven morphological profiles into the mouse mammary fat pad and examined the metastatic potential of each morphology. They observed that, depending

on the morphology class, there were differences in metastatic potential and tumorigenesis compared to the parental line in vivo. They found a range of aggressiveness of the SCC: low tumorigenicity, tumorigenic, metastatic, and hypermetastatic. While they had several interesting findings regarding metastasis, tumor volume, and circulating tumor cells burden, they identified that cells with a high aspect ratio do not have higher metastatic potential, contradicting other findings in the literature by Lyons et al. Interestingly, SCCs with the same morphology displayed similar in vivo outcomes of tumorigenicity, circulating tumor cells, and metastatic potential; this highlights the connection between cellular appearance and metastasis. Stratifying the morphologies into high and low metastatic potential with corresponding expression profiles allowed Wu et al. to identify potential predictive genes of metastasis for their cell line of choice. This correlative study of metastatic morphological phenotypes highlights the immense impact that homogenous heritable morphological traits condense the heterogeneous genomic landscape to stereotypical cell morphologies.

Functionalized coated cell surfaces further 2D morphological profiling of metastasis

Instead of using traditional plastic culture dishes or plain glass slides, Hasan et al. used 2D light microscopy of metastatic glioblastoma and

astrocytes on functionalized glass coverslips (Hasan et al. 2018). They trained a supervised classifier with an accuracy of 82% to discriminate between non-cancerous astrocytes and metastatic glioblastoma cells taken from a patient biopsy. They previously developed a glass-coated coverslip with anti-EGFR aptamer, which showed a high affinity for cells that overexpress EGFR on the cell surface (Mahmood et al. 2015; Wan et al. 2010; Wan et al. 2013; Mansur et al. 2018). Building upon this in the current study, they laid the foundation to develop a framework to identify circulating tumor cells from blood samples in glioblastoma patients. The captured cells by the aptamer were able to move about over time while anchored to the coverslip to achieve short-term time-lapse imaging. They extracted multiple cell feature vectors such as area, perimeter, and center of mass. Each segmentation model includes aspect ratio, convexity, bounding rectangle, minimum enclosing circle, and best-fitted ellipse based on single cells feature vectors. They tracked the morphodynamic changes using the feature vectors of each segmentation model using the Hausdorff distance between time frames. Hasan et al. trained three different machine learning classifiers, Support Vector Machine (SVM), Naïve Bayes Classifier, and Random Forest Tree. They decided that the Naïve Bayes Classifier yielded the best classification results. They presented a unique and label-free approach that can be quickly implemented using standard instruments and low

computational power in a clinical setting. Such a pipeline is a powerful tool, especially for those that work with cells that are hard to transfect or for samples one may not want to perturb using fluorescent proteins.

Alizadeh et al. used fluorescent imaging of over a dozen cancer cell lines, with varying metastatic potential, on fibronectin-coated glass coverslips (Alizadeh et al. 2020). To discriminate between populations, they quantified the texture of the cell, the spreading of the cell, and irregular cell shape, all of which trained an SVM or shallow layered Perceptron. They found that cell and nuclei geometric shape features, interpreted as cellular spread size, elongation, and boundary irregularity, reliably represented a cell over experimental replicates and cell types. However, label-free features such as texture are a more reliable representation of cell states. Of note in this study was the comparison of high (MDA-MB-231), low metastatic (MCF7), and normal breast cells (MCF10A) and a range of linearly progressed matched osteosarcoma cancer cell lines. Using the extracted morphological information in the reduced principal component (PCA) space, they showed no linear progression from normal to low then high metastatic morphological space; instead, there is some overlap in each morphometric category. For instance, the normal breast cells' cell hull geometry and waviness (Fourier transform) lie between low and high

metastatic potential breast cancer cell lines. However, the low metastatic potential lies between normal and high metastatic features for grayscale morphological features. Grayscale and cell geometry features displayed significant separation between the normal and osteosarcoma cancer lines for the osteosarcoma cell lines.

In contrast, waviness and hull geometry showed a high overlap of all cell lines. They tested the morphological features at the single-cell level using an SVM or Perceptron. They found that morphometric-based features are more feature-rich for classification. They can discriminate between the high and low metastatic cells of both osteosarcoma and breast cancer cell lines. They concluded that there might be stereotypical morphological transformations in the metastatic process. However, based on this study alone, it cannot be supposed how many stereotypical categories there may be for metastatic cells, which leaves an opportunity for long-term morphometric analysis of the development of normal to metastatic cells over many cancer types.

2.5D imaging and interpretable deep learning

Zaritsky et al. used label-free imaging and interpretable deep learning to identify cellular properties that discriminated between high and low

metastatic potential patient-derived xenografted (PDX) melanoma cells (Zaritsky et al. 2022). Most studies use live-cell imaging and deep learning for classification (**Fig 1.3A-C**). Zaritsky et al. generated in silico images based on latent features to identify (**Fig 1.3D**) cellular properties that opened the black box of the deeply learned model to visualize the cell appearance differences which discriminate between high and low metastatic melanoma. While not strictly 2D, they imaged the PDXs atop a thick collagen matrix to negate the physical forces of a plastic/glass and the morphological homogeneity plastic culture dishes impose. They imaged the metastatic cells over multiple time durations to gather morphological dynamics. They noticed that metastatic cells were not particularly migratory and were defined mainly by rounded shape, with surface membrane blebbing, regardless of metastatic potential; this is consistent with other studies' patient biopsies atop collagen (Sadok et al. 2015). They hypothesized that neither shape nor migratory ability would yield discriminative power between high and low metastatic cells. Instead, the discriminatory power may come from

visually unstructured information in the images; to this end, they developed an interpretable deep

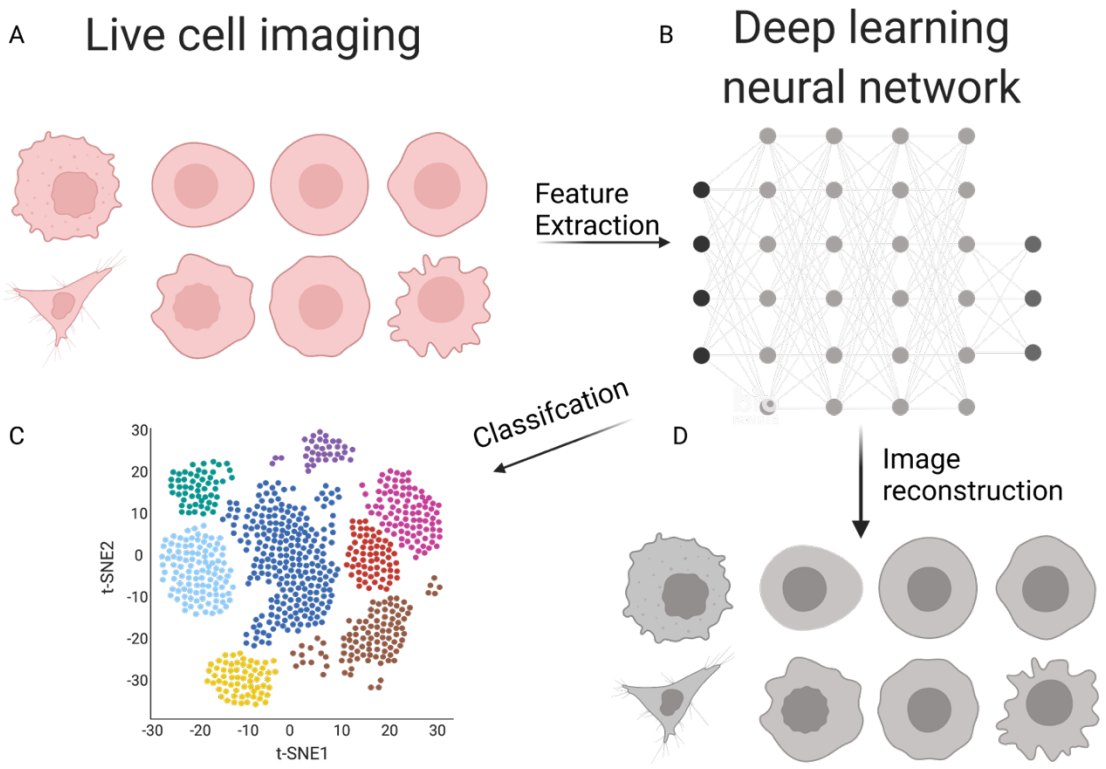

Figure 1.3 Opening the black box of deep learning to identify the features used for classification of metastatic cells. Live-cell images **(A)** feed into various deep learning neural networks **(B)** for unsupervised feature extraction. The learned features are the basis of the classification of metastatic cells **(C)**. These features are often a black box of unknown representation of cell appearance. However, there are methods to decipher the essential cellular properties through image reconstruction **(D)**.

learned model. First, they created an autoencoder, which uses a deep convolutional neural network (CNN) to encode the unstructured latent cell information. Next, they transferred the architecture (Donovan-Maiye et al. 2022) previously used to reconstruct fluorescent images for their phase-contrast images. They could designate a latent cell descriptor that contains a compressed version of single-cell image information.

Using this latent cell descriptor, they could discriminate between a panel of metastatic melanoma cell lines against fetal foreskin melanocytes. Intriguingly, the latent descriptor could discern a single cell clonal line from a parental line. Furthermore, they could successfully discriminate between the cell line and PDX metastatic melanoma panels. Incongruent with the other studies mentioned in this review, cell shape performed worse than the latent cell descriptor, and temporal information did not increase the latent descriptor's discriminative power. They were able to discriminate between high and low metastatic melanoma PDXs using the latent cell descriptor and linear discriminate analysis machine learning classifier. The authors investigated the latent descriptor encoded in cell properties while exploring existing deep learning models on a unique physiologically relevant 2D system. They identified that pseudopodial extensions and interior light scattering cell properties discriminate between high and low metastatic melanoma. It is important to note that many studies focused on using machine learning and deep learning methods to identify differences in morphologies of metastatic cells; most studies have not used interpretable methods. The lack of interpretability is common in most investigations of cell appearance connections to the metastatic state, yet it is critical to work backward from phenotype to actionable signaling targets.

Integrating spatiotemporal information for morphological profiling

While imaging in 2D has profoundly impacted the field, it was always apparent that those studies were missing the mechanical forces that affect the cytoskeleton and thus the signaling pathways to which it connects. Furthermore, cell actions imaged over time illuminate stereotyped cell behaviors (Tweedy et al. 2019). Here we focus on studies that have exploited time-lapsed imaging of dynamic morphological changes (**Fig 1.4A-C**) and three-dimensional (3D) imaging of cells in suspension (**Fig 1.4D**), in spheroid culture (**Fig 1.4E**), and embedded in collagen matrixes (**Fig 1.4F**).

Elbez et al. developed a unique approach to image single-cell dynamic morphological phenotypes using machine learning and magneto-rotation, simulating circulating tumor cell morphologies (Elbez et al. 2021). They exploited magnetic nanoparticles, which can endocytose into the cell, activating green-fluorescent protein (GFP). They used an external oscillating magnetic field to suspend and rotate cells with the nanoparticles in a microfluidic device they could image 3D morphological deformation. Using the supervised Adaboost machine learning method of single cells (identified and segmented using GFP), they were able to locate metastatic cells (MDA-MB-231) that had undergone the EMT, cells that were not metastatic (MCF-7) with an f1 score of 0.965. Next, they used the prostate cancer cell line PC-

3 as a control, then forced PC-3 cells to undergo EMT and become HR-14 cells to test if their classifier could identify the same cell lineage. Still, they could differentiate between the two states of the same cell lineage with different cell states. The unsupervised K-means clustering method (with a strict homogeneity score of 0.95) identified seven distinct morphological phenotypes within the populations. They followed up on this and determined they could differentiate between functional phenotypes of high and low migratory and invasive cells using the MDA-MB-231 cell line and a Boyden chamber. Unfortunately, they do not identify the morphological phenotypes that either machine-learned method used to discriminate between the populations; however, using interpretable learning methods remedies this issue.

Recently metastatic breast cancer cell lines embedded in collagen exhibited morphological phenotype transitions that allowed them to efficiently traverse non-uniform matrixes that mimic the ECM (Eddy et al. 2021). They developed machine learning models to quantify cell shape dynamics in 3D for up to 24 hours. Eddy et al. quantified cell appearance using twenty-one shape geometric features, including cell size, backbone curvature, surface topography, deviation from circle shape. They found the geometric space the cells sample is similar to random walk; however, they

found the morphology dynamics are subdiffusive while having superdiffusive properties in actual 3D space. Interestingly, they found the same cells exhibited increased morphodynamics sampling of geometric space on 2D surfaces than 3D embedded in ECM; this again highlights meaningful differences between 3D and 2D morphological analysis. Using manually labeled cells, they trained an SVM to classify the cells into four distinct cell morphological phenotypes, with an accuracy of 88%. The four morphological phenotypes they ranked are actin-enriched leading edge, small blebbing, filopodial, and lamellipodial. They focused on these four morphological phenotypes due to their tight connection to molecular profiles: actin-enriched have elevated actin protrusions; small blebbing has high cortical stress, which drives the blebbing; filopodial and lamellipodial phenotypes have strong ECM adhesions with polarized bodies, where the filopodial distinguish themselves with F-actin bundles running across the cell body, while the lamellipodial distinguishes itself through cellular fan shapes. They perturbed the signaling networks attached to these phenotypes and changed and also changed the ECM homogeneity. Focusing on disrupting the RHO/Rock signaling pathway, they discovered that perturbations did not force cells to favor one phenotype over another; instead, they altered phenotypes' morphodynamics.

Decreasing RHO expression led to amoeboid-to-mesenchymal transitions through the actin-enrich and lamellipodial phenotypes. In contrast, activation of RHO led to increased morphodynamics overall, which enriched the blebbing morphological phenotype. This sheds light on the required morphological plasticity to traverse heterogeneous ECM through phenotype switching. Still, this study also highlights the interpretable use of machine learning critical for furthering metastatic research.

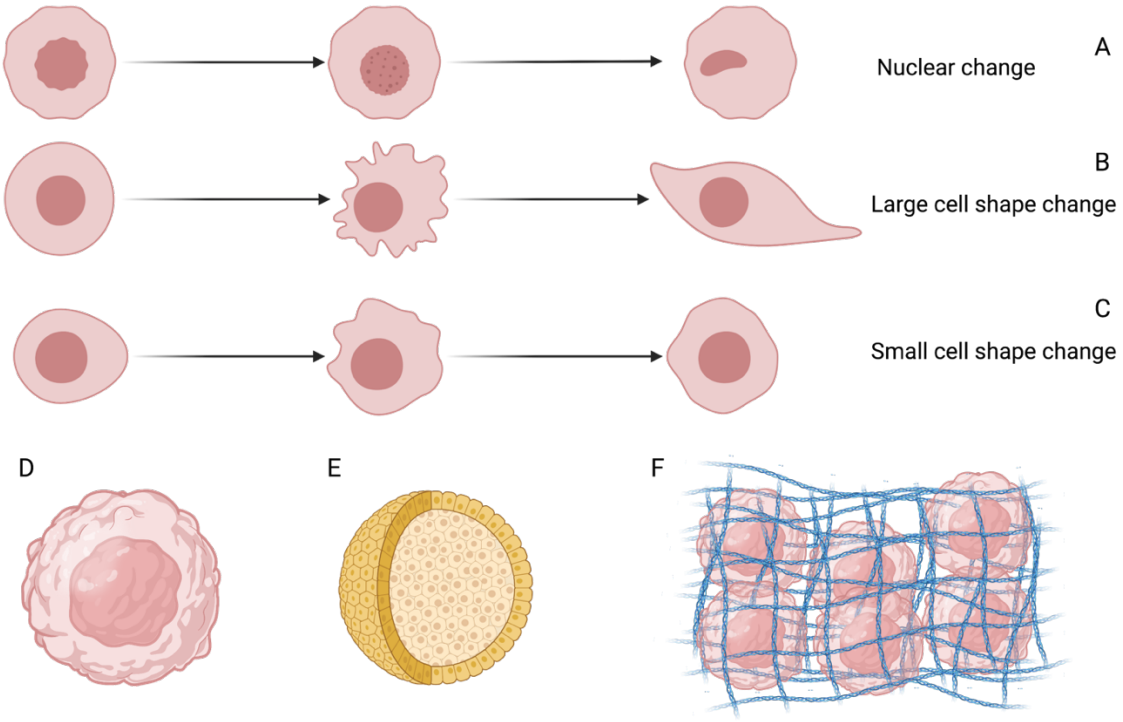

Figure 1.4 Cell appearance dynamics resolved through time-lapse imaging modalities. (A) Depicts nuclear changes over time, (B) depicts significant cell shape changes, while **(C)** depicts more minor scale shape changes. Diagram of different types of 3D cell interrogation with cells **(D)** single cells suspended, while **(E)** shows spheroid cells, and **(F)** shows single cells embedded in an extracellular matrix.

Future prospective and concluding remarks

While not used previously in identifying metastatic cells, we want to highlight Imaging Flow Cytometry (IFC). The pairing of deep learning and machine learning with different imaging technologies such as IFC can interrogate the metastatic stage in primary samples as part of the pathology pipeline. Given that these samples can be fragile and genetic engineering can perturb the cell state, IFC can probe the cell using cell light scatter and brightfield images. Both require no labels for cancer classification with deep and machine learning (Doan et al. 2021; Hennig et al. 2017). Tang and Chen et al. use this label-free deep learning analysis of 3D images (Tang et al. 2020; Chen et al. 2021). The future use of this technology and deployment of trained deep learned models can rapidly identify metastatic cell states, allowing the physician to make decisions about treatment.

We have highlighted multiple studies investigating cell appearance in varying spatiotemporal imaging modalities as a readout of metastatic potential to accelerate the discovery of metastatic specific features. With the massive expansion of deep and machine-learned models, we can process large amounts of imaging data. These works have levied the rich information found in images of metastatic cancer cells, therefore, overcoming the limits seen using the genetic code for metastatic profiling.

Using morphology, the quantified cell appearance differences have been connected to enhanced cell cycle progression, especially important for micro-metastases (Mohan et al. 2019; Molinie et al. 2019). Multiple studies have followed up on their metastatic cell appearance metrics in vivo using a mouse model. Indeed, these cell appearance changes identified using A.I. have translated to in vivo metastatic potential.

Rather than focusing on a specific gene, the works highlighted here offer a holistic quantitative phenotype-genotype approach for identifying novel or overlooked weak points of metastasis. Cell appearance is highly connected to cell state, sometimes causally; we can determine the impact of existing therapies on metastatic states. While it may seem evident that anti-cytoskeletal treatments will inhibit metastasis (Fife, McCarroll, and Kavallaris 2014; Gandalovičová et al. 2017; Aseervatham 2020), these drugs often are non-specific to metastatic tumors. They are highly cytotoxic and cardiotoxic (Stehn et al. 2013) and often fail to suppress metastasis. We believe this is due to cytoskeletal plasticity escape of targeted therapy, which Eddy et al.'s study highlights.

Understanding how cells from a primary tumor source can develop to form metastases in the brain and lung, two highly distinct environments,

each with their unique challenges to thrive, is critical to identifying these in core and liquid biopsies. The purpose of this review is to serve as an opportunity to extend these quantitative morphological assays to new frontiers probing more realistic microenvironments in which metastatic cells reside. In exciting avenues, we can use advanced imaging modalities to image immune co-culture, spheroid, and embedded cell culture. We will learn more about subtle cell appearance characteristics in a more realistic environment. Therapies do not have to target the metastatic cell or surrounding environment solely; instead, manipulating the microbiome, immune cells, and the microenvironment to inhibit metastasis are promising avenues of metastatic treatment (Sepich-Poore et al. 2021; Garner and de Visser 2020; Dmello, To, and Chand 2021). The mentioned works have made it feasible and affordable for the community to focus on the last formidable frontier of cancer treatment, metastasis.

Conflict of interest statements

Nothing declared.

Acknowledgments

Chapter 1, in part is currently being prepared for submission for publication of the material. Nevarez, Andres; Hao, Nan. The dissertation author was the primary investigator and author of this material.

This work was supported by the National Institutes of Health, National Institute of General Medical Sciences, USA, R01GM111458. We would like to acknowledge Saruna Artwork for adapting the Waddington landscape in Figure 1. We would like to acknowledge Biorender for the icons for Figures 2-4.

References

Adeshakin, Funmilayo O., Adeleye O. Adeshakin, Lukman O. Afolabi, Dehong Yan, Guizhong Zhang, and Xiaochun Wan. 2021. 'Mechanisms for Modulating Anoikis Resistance in Cancer and the Relevance of Metabolic Reprogramming', *Frontiers in Oncology*, 11.

Alizadeh, Elaheh, Jordan Castle, Analia Quirk, Cameron D. L. Taylor, Wenlong Xu, and Ashok Prasad. 2020. 'Cellular morphological features are predictive markers of cancer cell state', *Computers in Biology and Medicine*, 126: 104044.

Aseervatham, Jaya. 2020. 'Cytoskeletal Remodeling in Cancer', *Biology*, 9: 385.

Baghban, Roghayyeh, Leila Roshangar, Rana Jahanban-Esfahlan, Khaled Seidi, Abbas Ebrahimi-Kalan, Mehdi Jaymand, Saeed Kolahian, Tahereh Javaheri, and Peyman Zare. 2020. 'Tumor microenvironment complexity and therapeutic implications at a glance', *Cell Communication and Signaling*, 18: 59.

Bakal, Chris, John Aach, George Church, and Norbert Perrimon. 2007. 'Quantitative morphological signatures define local signaling networks regulating cell morphology', *science*, 316: 1753-56.

Bernards, René, and Robert A Weinberg. 2002. 'Metastasis genes: a progression puzzle', *Nature*, 418: 823-23.

Bockhorn, Maximilian, Rakesh K. Jain, and Lance L. Munn. 2007. 'Active versus passive mechanisms in metastasis: do cancer cells crawl into vessels, or are they pushed?', *The Lancet. Oncology*, 8: 444-48.

Bogenrieder, Thomas, and Meenhard Herlyn. 2003. 'Axis of evil: molecular mechanisms of cancer metastasis', *Oncogene*, 22: 6524-36.

Calbo, Joaquim, Erwin van Montfort, Natalie Proost, Ellen van Drunen, H Berna Beverloo, Ralph Meuwissen, and Anton Berns. 2011. 'A functional role for tumor cell heterogeneity in a mouse model of small cell lung cancer', *Cancer cell*, 19: 244-56.

Chen, Xinyu, Lauren Waller, Jiajie Chen, Rui Tang, Zunming Zhang, Ivan Gagne, Bien Gutierrez, Sung Hwan Cho, Chi-Yang Tseng, Ian Y. Lian, and Yu-Hwa Lo. 2021. 'Label-free image-encoded microfluidic cell sorter with a scanning Bessel beam', *APL Photonics*, 6: 076101.

Cheung, Kevin J., and Andrew J. Ewald. 2016. 'A collective route to metastasis: Seeding by tumor cell clusters', *Science (New York, N.Y.)*, 352: 167-69.

Cheung, Kevin J., Veena Padmanaban, Vanesa Silvestri, Koen Schipper, Joshua D. Cohen, Amanda N. Fairchild, Michael A. Gorin, James E. Verdone, Kenneth J. Pienta, Joel S. Bader, and Andrew J. Ewald. 2016. 'Polyclonal breast cancer metastases arise from collective dissemination of keratin 14-expressing tumor cell clusters', *Proceedings of the National Academy of Sciences*, 113: E854-E63.

Chiang, Anne C, and Joan Massagué. 2008. 'Molecular basis of metastasis', *New England Journal of Medicine*, 359: 2814-23.

Cooper, Sam, Amine Sadok, Vicky Bousgouni, and Chris Bakal. 2015. 'Apolar and polar transitions drive the conversion between amoeboid and mesenchymal shapes in melanoma cells', *Molecular biology of the cell*, 26: 4163-70.

Dillekås, Hanna, Romano Demicheli, Ilaria Ardoino, Svein AH Jensen, Elia Biganzoli, and Oddbjørn Straume. 2016. 'The recurrence pattern following delayed breast reconstruction after mastectomy for breast cancer suggests a systemic effect of surgery on occult dormant micrometastases', *Breast cancer research and treatment*, 158: 169-78.

Dmello, R. S., S. Q. To, and A. L. Chand. 2021. 'Therapeutic Targeting of the Tumour Microenvironment in Metastatic Colorectal Cancer', *Int J Mol Sci*, 22.

Doan, Minh, Claire Barnes, Claire McQuin, Juan C. Caicedo, Allen Goodman, Anne E. Carpenter, and Paul Rees. 2021. 'Deepometry, a framework for applying supervised and weakly supervised deep learning to imaging cytometry', *Nature Protocols*, 16: 3572-95.

Donovan-Maiye, Rory M., Jackson M. Brown, Caleb K. Chan, Liya Ding, Calysta Yan, Nathalie Gaudreault, Julie A. Theriot, Mary M. Maleckar, Theo A. Knijnenburg, and Gregory R. Johnson. 2022. 'A deep generative model of 3D single-cell organization', *PLOS Computational Biology*, 18: e1009155.

Eddy, Christopher Z., Helena Raposo, Aayushi Manchanda, Ryan Wong, Fuxin Li, and Bo Sun. 2021. 'Morphodynamics facilitate cancer cells to navigate 3D extracellular matrix', *Scientific Reports*, 11: 20434.

Elbez, Remy, Jeff Folz, Alan McLean, Hernan Roca, Joseph M. Labuz, Kenneth J. Pienta, Shuichi Takayama, and Raoul Kopelman. 2021. 'Cell-morphodynamic phenotype classification with application to cancer metastasis using cell magnetorotation and machine-learning', *PLOS ONE*, 16: e0259462.

Fares, Jawad, Mohamad Y. Fares, Hussein H. Khachfe, Hamza A. Salhab, and Youssef Fares. 2020. 'Molecular principles of metastasis: a hallmark of cancer revisited', *Signal Transduction and Targeted Therapy*, 5: 28.

Fife, C. M., J. A. McCarroll, and M. Kavallaris. 2014. 'Movers and shakers: cell cytoskeleton in cancer metastasis', *British journal of pharmacology*, 171: 5507-23.

Friedl, Peter, and Stephanie Alexander. 2011. 'Cancer Invasion and the Microenvironment: Plasticity and Reciprocity', *cell*, 147: 992-1009.

Gal, Kristell Le, Mohamed X. Ibrahim, Clotilde Wiel, Volkan I. Sayin, Murali K. Akula, Christin Karlsson, Martin G. Dalin, Levent M. Akyürek, Per Lindahl, Jonas Nilsson, and Martin O. Bergo. 2015. 'Antioxidants can increase melanoma metastasis in mice', *Science Translational Medicine*, 7: 308re8-08re8.

Gandalovičová, A., D. Rosel, M. Fernandes, P. Veselý, P. Heneberg, V. Čermák, L. Petruželka, S. Kumar, V. Sanz-Moreno, and J. Brábek. 2017. 'Migrastatics-Anti-metastatic and Anti-invasion Drugs: Promises and Challenges', *Trends Cancer*, 3: 391-406.

Garner, Hannah, and Karin E. de Visser. 2020. 'Immune crosstalk in cancer progression and metastatic spread: a complex conversation', *Nature Reviews Immunology*, 20: 483-97.

Goodman, Allen, and Anne E Carpenter. 2016. 'High-throughput, automated image processing for large-scale fluorescence microscopy experiments', *Microscopy and Microanalysis*, 22: 538-39.

Gordonov, Simon, Mun Kyung Hwang, Alan Wells, Frank B Gertler, Douglas A Lauffenburger, and Mark Bathe. 2016. 'Time series modeling of live-cell shape dynamics for image-based phenotypic profiling', *Integrative Biology*, 8: 73-90.

Gupta, Gaorav P, and Joan Massagué. 2006. 'Cancer metastasis: building a framework', *cell*, 127: 679-95.

Hanahan, Douglas, and Robert A Weinberg. 2011. 'Hallmarks of cancer: the next generation', *cell*, 144: 646-74.

Hasan, Mohammad R., Naeemul Hassan, Rayan Khan, Young-Tae Kim, and Samir M. Iqbal. 2018. 'Classification of cancer cells using computational analysis of dynamic morphology', *Computer Methods and Programs in Biomedicine*, 156: 105-12.

Hennig, Holger, Paul Rees, Thomas Blasi, Lee Kamentsky, Jane Hung, David Dao, Anne E. Carpenter, and Andrew Filby. 2017. 'An open-source solution for advanced imaging flow cytometry data analysis using machine learning', *Methods*, 112: 201-10.

Holenstein, Claude N., Aron Horvath, Barbara Schär, Angelina D. Schoenenberger, Maja Bollhalder, Nils Goedecke, Guido Bartalena, Oliver Otto, Maik Herbig, Jochen Guck, Daniel A. Müller, Jess G. Snedeker, and Unai Silvan. 2019. 'The relationship between metastatic potential and in vitro mechanical properties of osteosarcoma cells', *Molecular biology of the cell*, 30: 887-98.

Huang, Qiong, Xingbin Hu, Wanming He, Yang Zhao, Shihui Hao, Qijing Wu, Shaowei Li, Shuyi Zhang, and Min Shi. 2018. 'Fluid shear stress and tumor metastasis', *American journal of cancer research*, 8: 763-77.

Janssen, Louise M. E., Emma E. Ramsay, Craig D. Logsdon, and Willem W. Overwijk. 2017. 'The immune system in cancer metastasis: friend or foe?', *Journal for ImmunoTherapy of Cancer*, 5: 79.

Klein, Christoph A. 2009. 'Parallel progression of primary tumours and metastases', *Nature Reviews Cancer*, 9: 302-12.

Kok, Sau Yee, Hiroko Oshima, Kei Takahashi, Mizuho Nakayama, Kazuhiro Murakami, Hiroki R. Ueda, Kohei Miyazono, and Masanobu Oshima. 2021. 'Malignant subclone drives metastasis of genetically and phenotypically heterogenous cell clusters through fibrotic niche generation', *Nature Communications*, 12: 863.

Lee, Andrew HS, Zsolt Hodi, Irshad Soomro, Vishakha Sovani, Areeg Abbas, Emad Rakha, and Ian O Ellis. 2020. 'Histological clues to the diagnosis of metastasis to the breast from extramammary malignancies', *Histopathology*, 77: 303-13.

Li, Chunhe, and Gabor Balazsi. 2018. 'A landscape view on the interplay between EMT and cancer metastasis', *npj Systems Biology and Applications*, 4: 34.

Lo, Hin Ching, Zhan Xu, Ik Sun Kim, Bradley Pingel, Sergio Aguirre, Srikanth Kodali, Jun Liu, Weijie Zhang, Aaron M. Muscarella, Sarah M. Hein, Alexander S. Krupnick, Joel R. Neilson, Silke Paust, Jeffrey M. Rosen, Hai Wang, and Xiang H. F. Zhang. 2020. 'Resistance to natural killer cell immunosurveillance confers a selective advantage to polyclonal metastasis', *Nature Cancer*, 1: 709-22.

Lu, W., and Y. Kang. 2019. 'Epithelial-Mesenchymal Plasticity in Cancer Progression and Metastasis', *Dev Cell*, 49: 361-74.

Lyons, Samanthe M., Elaheh Alizadeh, Joshua Mannheimer, Katherine Schuamberg, Jordan Castle, Bryce Schroder, Philip Turk, Douglas Thamm, and Ashok Prasad. 2016. 'Changes in cell shape are correlated with metastatic potential in murine and human osteosarcomas', *Biology open*, 5: 289-99.

Mahmood, Mohammed Arif I, Mohammad Raziul Hasan, Umair JM Khan, Peter B Allen, Young-tae Kim, Andrew D Ellington, and Samir M Iqbal. 2015. 'One-step tumor detection from dynamic morphology tracking on aptamer-grafted surfaces', *Technology*, 3: 194-200.

Mansur, Nuzhat, Mohammad Raziul Hasan, Zaid I Shah, Frank J Villarreal, Young-tae Kim, and Samir M Iqbal. 2018. 'Discrimination of metastatic breast cancer cells from indolent cells on aptamer-functionalized surface with imaging-based contour-following techniques', *Biomedical Physics & Engineering Express*, 4: 025038.

Marusyk, Andriy, Doris P Tabassum, Philipp M Altrock, Vanessa Almendro, Franziska Michor, and Kornelia Polyak. 2014. 'Non-cell-autonomous driving of tumour growth supports sub-clonal heterogeneity', *Nature*, 514: 54-58.

Minn, Andy J, Yibin Kang, Inna Serganova, Gaorav P Gupta, Dilip D Giri, Mikhail Doubrovin, Vladimir Ponomarev, William L Gerald, Ronald Blasberg, and Joan Massagué. 2005. 'Distinct organ-specific metastatic potential of individual breast cancer cells and primary tumors', *The Journal of clinical investigation*, 115: 44-55.

Mohan, Ashwathi S, Kevin M Dean, Tadamoto Isogai, Stacy Y Kasitinon, Vasanth S Murali, Philippe Roudot, Alex Groisman, Dana K Reed, Erik S Welf, and Sangyoon J Han. 2019. 'Enhanced dendritic actin network formation in extended lamellipodia drives proliferation in growth-challenged Rac1P29S melanoma cells', *Developmental cell*, 49: 444-60. e9.

Molinie, Nicolas, Svetlana N Rubtsova, Artem Fokin, Sai P Visweshwaran, Nathalie Rocques, Anna Polesskaya, Anne Schnitzler, Sophie Vacher, Evgeny V Denisov, and Lubov A Tashireva. 2019. 'Cortical branched actin determines cell cycle progression', *Cell research*, 29: 432-45.

Moujaber, O., and U. Stochaj. 2020. 'The Cytoskeleton as Regulator of Cell Signaling Pathways', *Trends Biochem Sci*, 45: 96-107.

Nguyen, Alexander, Mitsukuni Yoshida, Hani Goodarzi, and Sohail F Tavazoie. 2016. 'Highly variable cancer subpopulations that exhibit enhanced transcriptome variability and metastatic fitness', *Nature Communications*, 7: 1-13.

Padmanaban, Veena, Ilona Krol, Yasir Suhail, Barbara M. Szczerba, Nicola Aceto, Joel S. Bader, and Andrew J. Ewald. 2019. 'E-cadherin is required for metastasis in multiple models of breast cancer', *Nature*, 573: 439-44.

Paget, Stephen. 1889. 'The distribution of secondary growths in cancer of the breast', *The Lancet*, 133: 571-73.

Pascual-Vargas, Patricia, Samuel Cooper, Julia Sero, Vicky Bousgouni, Mar Arias-Garcia, and Chris Bakal. 2017. 'RNAi screens for Rho GTPase regulators of cell shape and YAP/TAZ localisation in triple negative breast cancer', *Scientific data*, 4: 1-13.

Piskounova, Elena, Michalis Agathocleous, Malea M. Murphy, Zeping Hu, Sara E. Huddlestun, Zhiyu Zhao, A. Marilyn Leitch, Timothy M. Johnson, Ralph J. DeBerardinis, and Sean J. Morrison. 2015. 'Oxidative stress inhibits distant metastasis by human melanoma cells', *Nature*, 527: 186-91.

Ramaswamy, Sridhar, Ken N Ross, Eric S Lander, and Todd R Golub. 2003. 'A molecular signature of metastasis in primary solid tumors', *Nature genetics*, 33: 49-54.

Reddy, Bobby Y, Philip K Lim, Kimberly Silverio, Shyam A Patel, Brian Wong Won, and Pranela Rameshwar. 2012. 'The microenvironmental effect in the progression, metastasis, and dormancy of breast cancer: a model system within bone marrow', *International journal of breast cancer*, 2012.

Reymond, Nicolas, Bárbara Borda d'Água, and Anne J. Ridley. 2013. 'Crossing the endothelial barrier during metastasis', *Nature Reviews Cancer*, 13: 858-70.

Riehl, Brandon D., Eunju Kim, Tasneem Bouzid, and Jung Yul Lim. 2021. 'The Role of Microenvironmental Cues and Mechanical Loading Milieus in Breast Cancer Cell Progression and Metastasis', *Frontiers in Bioengineering and Biotechnology*, 8.

Sadok, Amine, Afshan McCarthy, John Caldwell, Ian Collins, Michelle D Garrett, Maggie Yeo, Steven Hooper, Erik Sahai, Sandra Kuemper, and Faraz K Mardakheh. 2015. 'Rho kinase inhibitors block melanoma cell migration and inhibit metastasis', *Cancer research*, 75: 2272-84.

Schardt, Julian A, Manfred Meyer, Claudia H Hartmann, Falk Schubert, Oleg Schmidt-Kittler, Christine Fuhrmann, Bernhard Polzer, Marco Petronio, Roland Eils, and Christoph A Klein. 2005. 'Genomic analysis of single cytokeratin-positive cells from bone marrow reveals early mutational events in breast cancer', *Cancer cell*, 8: 227-39.

Scheeder, Christian, Florian Heigwer, and Michael Boutros. 2018. 'Machine learning and image-based profiling in drug discovery', *Current opinion in systems biology*, 10: 43-52.

Sepich-Poore, Gregory D., Laurence Zitvogel, Ravid Straussman, Jeff Hasty, Jennifer A. Wargo, and Rob Knight. 2021. 'The microbiome and human cancer', *science*, 371: eabc4552.

Sero, Julia E, and Chris Bakal. 2017. 'Multiparametric analysis of cell shape demonstrates that β-PIX directly couples YAP activation to extracellular matrix adhesion', *Cell Systems*, 4: 84-96. e6.

Stehn, J. R., N. K. Haass, T. Bonello, M. Desouza, G. Kottyan, H. Treutlein, J. Zeng, P. R. Nascimento, V. B. Sequeira, T. L. Butler, M. Allanson, T. Fath, T. A. Hill, A. McCluskey, G. Schevzov, S. J. Palmer, E. C. Hardeman, D. Winlaw, V. E. Reeve, I. Dixon, W. Weninger, T. P. Cripe, and P. W. Gunning. 2013. 'A novel class of anticancer compounds targets the actin cytoskeleton in tumor cells', *Cancer Res*, 73: 5169-82.

Tang, Rui, Zunming Zhang, Xinyu Chen, Lauren Waller, Alex Ce Zhang, Jiajie Chen, Yuanyuan Han, Cheolhong An, Sung Hwan Cho, and Yu-Hwa Lo. 2020. '3D side-scattering imaging flow cytometer and convolutional neural network for label-free cell analysis', *APL Photonics*, 5: 126105.

Tasdogan, Alpaslan, Brandon Faubert, Vijayashree Ramesh, Jessalyn M Ubellacker, Bo Shen, Ashley Solmonson, Malea M Murphy, Zhimin Gu, Wen Gu, and Misty Martin. 2020. 'Metabolic heterogeneity confers differences in melanoma metastatic potential', *Nature*, 577: 115-20.

Tweedy, Luke, Patrick Witzel, Doris Heinrich, Robert H. Insall, and Robert G. Endres. 2019. 'Screening by changes in stereotypical behavior during cell motility', *Scientific Reports*, 9: 8784.

Van't Veer, Laura J, Hongyue Dai, Marc J Van De Vijver, Yudong D He, Augustinus AM Hart, Mao Mao, Hans L Peterse, Karin Van Der Kooy, Matthew J Marton, and Anke T Witteveen. 2002. 'Gene expression profiling predicts clinical outcome of breast cancer', *Nature*, 415: 530-36.

Waddington, C. H. 1959. 'Canalization of development and genetic assimilation of acquired characters', *Nature*, 183: 1654-5.

Wan, Yuan, Young-tae Kim, Na Li, Steve K Cho, Robert Bachoo, Andrew D Ellington, and Samir M Iqbal. 2010. 'Surface-immobilized aptamers for cancer cell isolation and microscopic cytology', *Cancer research*, 70: 9371-80.

Wan, Yuan, Deepika Tamuly, Peter B Allen, Young-tae Kim, Robert Bachoo, Andrew D Ellington, and Samir M Iqbal. 2013. 'Proliferation and migration of tumor cells in tapered channels', *Biomedical microdevices*, 15: 635-43.

Weis, Sara M, and David A Cheresh. 2011. 'aV integrins in angiogenesis and cancer', *Cold Spring Harbor perspectives in medicine*, 1: a006478.

Wu, Pei-Hsun, Daniele M Gilkes, Jude M Phillip, Akshay Narkar, Thomas Wen-Tao Cheng, Jorge Marchand, Meng-Horng Lee, Rong Li, and Denis Wirtz. 2020. 'Single-cell morphology encodes metastatic potential', *Science advances*, 6: eaaw6938.

Wu, Pei-Hsun, Jude M. Phillip, Shyam B. Khatau, Wei-Chiang Chen, Jeffrey Stirman, Sophie Rosseel, Katherine Tschudi, Joshua Van Patten, Michael Wong, Sonal Gupta, Alexander S. Baras, Jeffrey T. Leek, Anirban Maitra, and Denis Wirtz. 2015. 'Evolution of cellular morpho-phenotypes in cancer metastasis', *Scientific Reports*, 5: 18437.

Yates, Lucy R, and Peter J Campbell. 2012. 'Evolution of the cancer genome', *Nature Reviews Genetics*, 13: 795-806.

Yin, Zheng, Amine Sadok, Heba Sailem, Afshan McCarthy, Xiaofeng Xia, Fuhai Li, Mar Arias Garcia, Louise Evans, Alexis R Barr, and Norbert Perrimon. 2013. 'A screen for morphological complexity identifies regulators of switch-like transitions between discrete cell shapes', *Nature Cell Biology*, 15: 860-71.

Zaritsky, Assaf, Andrew R. Jamieson, Erik S. Welf, Andres Nevarez, Justin Cillay, Ugur Eskiocak, Brandi L. Cantarel, and Gaudenz Danuser. 'Interpretable deep learning uncovers cellular properties in label-free live cell images that are predictive of highly metastatic melanoma', *Cell Systems*.

Author ORCIDs

Andres Nevarez https://orcid.org/0000-0002-8337-6454

Nan Hao https://orcid.org/0000-0003-2857-4789

Chapter Two

Interpretable deep learning uncovers cellular properties in label-free live cell images that are predictive of highly-metastatic melanoma

Assaf Zaritsky[1,2*§], Andrew R. Jamieson[1*], Erik S. Welf[1*], Andres Nevarez[1,3*], Justin Cillay[1], Ugur Eskiocak[4], Brandi L. Cantarel[l], Gaudenz Danuser[1§]

[1]Lyda Hill Department of Bioinformatics, UT Southwestern Medical Center, Dallas, TX 75390, USA

[2]Department of Software and Information Systems Engineering, Ben-Gurion University of the Negev, Beer-Sheva 84105, Israel

[3]Section of Molecular Biology, Division of Biological Sciences, University of California San Diego, 9500 Gilman Drive, La Jolla, CA 92093, USA

[4]Children's Research Institute and Department of Pediatrics, University of Texas Southwestern Medical Center, Dallas, TX 75390, USA

* Equal contribution.

§ Corresponding author.

Abstract

Deep learning has emerged as the technique of choice for identifying hidden patterns in cell imaging data, but is often criticized as 'black-box'. Here, we employ a generative neural network in combination with supervised machine learning to classify patient-derived melanoma xenografts as 'efficient' or 'inefficient' metastatic, validate predictions regarding melanoma cell lines with unknown metastatic efficiency in mouse xenografts, and use the network to generate *in silico* cell images that amplify the critical predictive cell properties. These exaggerated images unveiled pseudopodial extensions and increased light scattering as hallmark properties of metastatic cells. We validated this interpretation using live cells spontaneously transitioning between states indicative of low and high metastatic efficiency. This study illustrates how the application of Artificial Intelligence can support the identification of cellular properties that are predictive of complex phenotypes and integrated cell functions but are too subtle to be identified in the raw imagery by a human expert.

Introduction

Recent machine learning studies have impressively demonstrated that label-free images contain information on the molecular organization within the cell (Cheng et al., 2021; Christiansen et al., 2018; Guo et al., 2019; LaChance and Cohen, 2020; Ounkomol et al., 2018; Sullivan and Lundberg, 2018; Yuan et al., 2018). These studies relied on generative models that transform label-free to fluorescent images, which can indicate the organization and, in some situations, even the relative densities of molecular structures. Models were trained by using pairs of label-free and fluorescence images subject to minimizing the error between the fluorescence ground-truth image and the model-generated image. Other studies used similar concepts to enhance imaging resolution by learning a mapping from low-to-high resolution (Belthangady and Royer, 2019; Fang et al., 2019; Nehme et al., 2018; Ouyang et al., 2018; Wang et al., 2019; Weigert et al., 2018). Common to all these studies is the concept that the architecture of a deep convolutional neural network can extract from the label-free or low-resolution cell images unstructured hidden information – also referred to as *latent information* – that is predictive of the molecular organization of a cell or its high-resolution image yet escapes the human eye.

We wondered whether this paradigm could be applied also to the prediction of complex cell states that result from the convergence of numerous structural and molecular factors. We combined unsupervised generative deep neural networks and supervised machine learning to train a classifier that can predict the metastatic efficiency of human melanoma cells. The power of cell appearance for determining cell states that correlate with function has been the basis of decades of histopathology (Chan, 2014a; López, 2013a; Travis et al., 2013). Cell appearance has been established as an explicit predictor of signaling states that are directly implicated in the regulation of cell morphogenesis (Bakal et al., 2007; Goodman and Carpenter, 2016; Gordonov et al., 2015; Pascual-Vargas et al., 2017; Scheeder et al., 2018; Sero and Bakal, 2017; Yin et al., 2013). Whether cell appearance is also informative of a broader spectrum of cell signaling programs, such as those driving processes in metastasis, is less clear, although very recent work, using conventional shape-based machine learning of fluorescently labeled cell lines, suggests this may be the case (Wu et al., 2020).

The paradigm of extracting latent information via deep convolutional neural networks from label-free and time-resolved image sequences holds particularly strong promise for a task of this complexity. The design of cell

appearance metrics that encode the state of, e.g., a cellular signal that promotes cell survival or proliferation, exceeds human intuition. The flip side of learning information that classifies well but is non-intuitive is the discomfort of relying on a 'black box'. Especially in a clinical setting, the lack of a straightforward meaning of key drivers of a classifier is a widely perceived weakness of deep learning systems. Here, we demonstrate a mechanism to overcome this problem: By generating "in silico" cell images that were never observed experimentally we "reverse engineered" the physical properties of the latent image information that discriminates melanoma cells with low versus high metastatic efficiency. These results demonstrate that the internal encoding of latent variables in a deep convolutional neural network can be mapped to physical entities predictive of complex cell states. More broadly, they highlight the potential of "interpreted artificial intelligence" to augment investigator-driven analysis of cell behavior with an entirely novel set of hypotheses.

Results

Label-free imaging of living patient-derived xenograft (PDX) melanoma cells and cell lines

To test whether the latent information extracted from label-free live cell movies can predict the metastatic propensity of melanoma, we relied on a previously established patient-derived xenotransplantation (PDX) assay, in which tumor samples from stage III melanoma patients were taken and repeatedly transplanted between immuno-compromised mice (Quintana et al., 2012). All tumors grew and eventually seeded metastases in the xenograft model. Whereas some tumors seeded widespread metastases in various distant organs, referred to as a PDX with high metastatic efficiency, other tumors mainly seeded only lung metastases, referred to as a PDX with low metastatic efficiency. Low efficiency PDXs originated from patients that were cured after surgery and chemotherapeutic treatment. High efficiency PDXs originated from patients with fatal outcome (Quintana et al., 2012).

For this study, we had access to a panel of nine PDXs, seven of which had known metastatic efficiency and matching patient outcome. For the remaining two PDXs, the metastatic efficiency, including patient outcome, was unknown (Table S1). To define the genomic states of the PDXs with

known metastatic efficiency, we sequenced a panel of ~1400 clinically actionable genes and found that the PDXs span the genomic landscape of melanoma mutations, including mutations in BRAF (5/6), CKIT (2/6), NRAS (1/6), TP53 (2/6), and copy number variation (CNV) in CDKN2A (6/6) and PTEN (3/6) (Hayward et al., 2017; Hodis et al., 2012) (Table S2). For one PDX (m528), we were unable to generate sufficient genomic material for sequencing, although the cell culture was sufficiently robust for single cell imaging.

In order to prevent morphological homogenization and to better mimic the collagenous ECM of the dermal stroma, we imaged cells on top of a thick slab of collagen. The cells were plated sparsely to focus on cell-autonomous behaviors with minimal interference from interactions with other cells (Methods). For each plate, we recorded with a 20X/0.8NA lens phase contrast movies of at least 2 hours duration, sampled at 1 minute intervals (**Fig. 2.1A, Video S1-2**). Each recording sampled 10-20 randomly distributed fields of view from 1-4 plates of different cell types, each containing 8-20 individual cells.

Figure 2.1. **Unsupervised learning of a latent vector that encodes characteristic features of individual melanoma cells**. (**A**) Top: Snapshot of a representative field of view of m481 PDX cells. Scale bar = 50 μm. Bottom: Time-lapse sequence of a single cell undergoing dynamic blebbing. Scale bar = 50 μm. (**B**) Representative time-lapse images of single cells from PDX tumors exhibiting low (m498) and high (m634) metastatic efficiency. Sequential images were each acquired 1 minute apart. (**C**) Design of the adversarial autoencoder, comprising an encoder (dark red) to extract from single cell images a 56-dimensional latent vector, so that a decoder can reconstruct from the vector a similar image. The "adversarial" component (top) penalizes randomly generated latent cell descriptors q(z) that the network fails to distinguish from latent cell descriptors drawn from the distribution of observed cells p(z). (**D**) Examples of cell reconstructions. Raw cell images (top): beginning of epoch #110K (trained on 10,000 images), around midway training of epoch #11M (after 1,000,000 images), at the end of epoch #3, epoch #6, and epoch #46. (**E**) Convergence of autoencoder loss (binary cross-entropy between raw and reconstructed image). Epoch is a full data set training cycle that consists of ~1.7 million images. Mini-batch is the number of images processed on the GPU at a time. Each mini-batch includes 50 cell images randomly selected for each network parameter learning update. For every epoch, the images order is scrambled and then partitioned into ordered sets of 50 for each mini-batch.

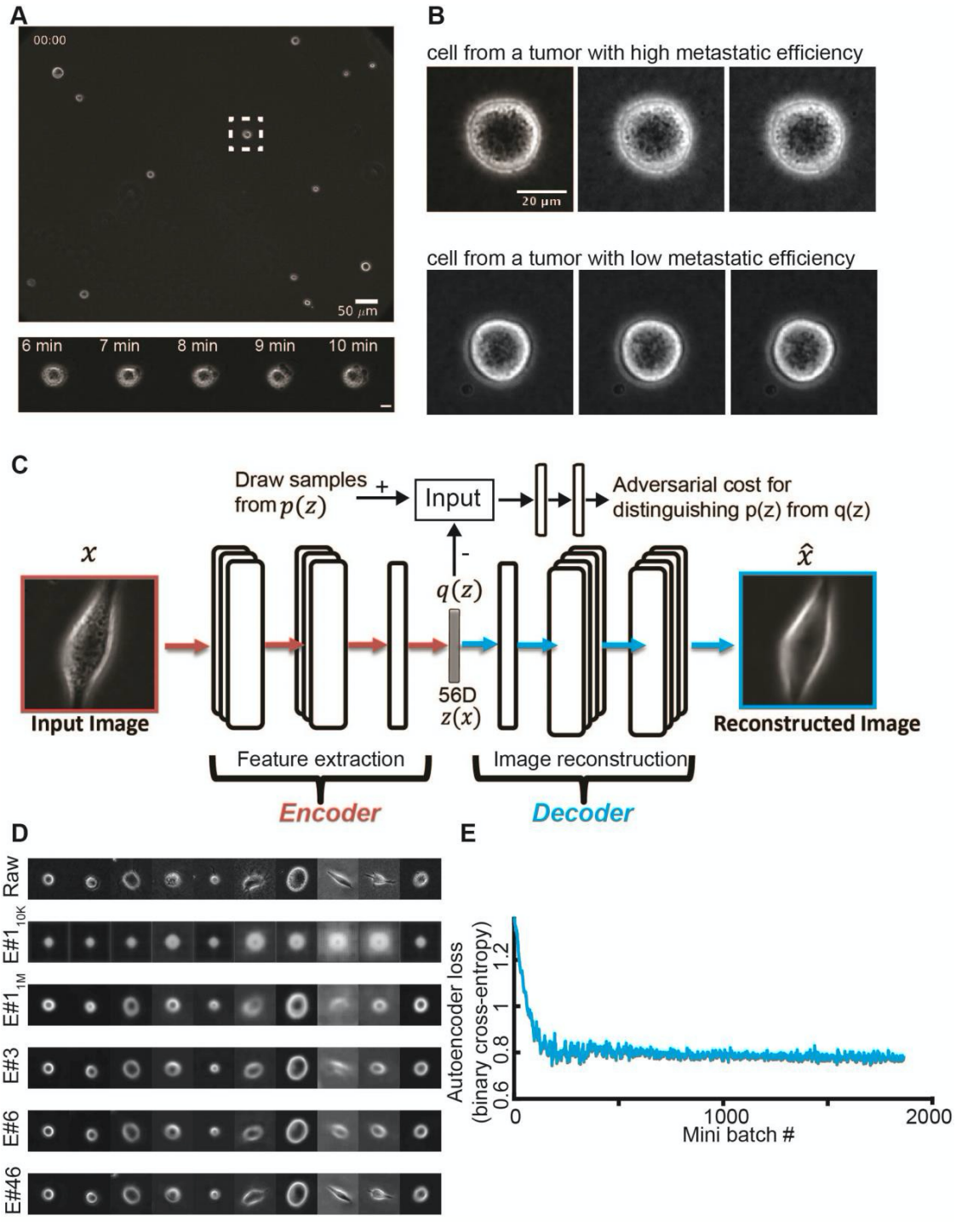
A
00:00
50 μm
6 min
7 min
8 min
9 min
10 min
B
cell from a tumor with high metastatic efficiency
20 μm
cell from a tumor with low metastatic efficiency
C
Draw samples from $p(z)$
Input
Adversarial cost for distinguishing p(z) from q(z)
x
$q(z)$
$\hat{x}$
56D $z(x)$
Input Image
Reconstructed Image
Feature extraction
Image reconstruction
Encoder
Decoder
D
Raw
E#1$_{10K}$
E#1$_{1M}$
E#3
E#6
E#46
E
Autoencoder loss (binary cross-entropy)
0.6
0.8
1
1.2
0
1000
2000
Mini batch #

We complemented the PDX data set with equivalently acquired time-lapse sequences of two untransformed melanocyte cell lines and six melanoma cell lines. The former served as a control to test whether the latent information allows at minimum the distinction of untransformed and metastatic cells. The latter served as a control to test whether the latent information allows the distinction of different cell populations, which, by the long-term selection of passaging in the lab, likely have drifted to a spectrum of molecular and regulatory states that differs from the PDX.

In total, our combined data set comprises time-lapse image sequences of more than 12,000 single melanoma cells, resulting in approximately 1,700,000 raw images. The cells were typically not migratory but displayed variable morphology and local dynamics (Video S3). Many of the cells were characterized by an overall round cell shape and dynamic surface blebbing (Fig. S1A, Video S1-2), regardless of whether they belonged to the melanoma group with high or low metastatic efficiency (Fig. 1B, Fig. S1B), which is consistent with reports of primary melanoma behavior *in vivo* (Pinner and Sahai, 2008; Sadok et al., 2015; Sahai and Marshall, 2003) and on soft substrates *in vitro* (Cantelli et al., 2015; Welf et al., 2016). Thus, we speculated that cell shape or motion might not be informative of the metastatic state of a melanoma cell. Nonetheless, we still noted textural

variation and dynamics between individual cell images. Thus, we wondered whether these images contain visually unstructured signal that could predict the metastatic propensity of a cell.

Design of adversarial autoencoders for unsupervised feature extraction

After detection and tracking of single cells over time (Methods), we used the cropped single cell images as atomic units to train an adversarial autoencoder (Makhzani et al., 2015) (**Fig. 2.1C, Methods**). The autoencoder comprises a deep convolutional neural network to "encode" the image data of a single cell in a vector of latent information, from which a structurally symmetric deep convolutional neural network "decodes" synthetic images (Fig. 2.1C). The networks are trained to minimize the discrepancy between input and reconstructed images. The adversarial component penalizes randomly generated latent cell descriptors q(z) that the network fails to distinguish from latent cell descriptors drawn from the distribution of observed cells p(z), thus ensuring regularization of the latent information space. Our network architecture employed the part of the network previously used to reconstruct landmarks of the cell nucleus and cytoplasm (Johnson et al., 2017) in fluorescence microscopy images. We supplied the network with

phase-contrast images instead of fluorescence images and found that the adversarial autoencoder displayed fast convergence in reconstructing phase-contrast cell images (**Fig. 2.1D-E, Video S4, Fig. S1C**). Furthermore, the trained network's latent space defined a faithful metric for discriminating images of cells that appear morphologically different (Methods, Fig. S2). The network training was agnostic to the subsequent classification task. The goal of this step was to determine for each melanoma cell an unsupervised latent cell descriptor that holds a compressed representation of a cell image for further classification of cell states.

The latent cell descriptor can discriminate between different cell categories

In our label-free imaging assay, the latent space cell descriptors seemed to be distorted by batch effects related to inconsistencies in different imaging sessions such as operator, microscope, and gel preparation (Methods, Fig. S3). These systematic but meaningless variations in the data are a major hurdle in classification tasks (Boutros et al., 2015; Caicedo et al., 2017; Chandrasekaran et al., 2020). To address this issue, we transformed the auto-encoder latent space into a classifier space that was robust to inter-day confounding factors, but discriminated between different cell categories. A cell category was defined as a set of multiple cell types

with a common property. For example, the category "cell line" comprises six different cell types: A375, MV3, WM3670, WM1361, WM1366, and SKMEL2. The discrimination was accomplished by training supervised machine learning models on the normalized latent cell descriptor using Linear Discriminant Analysis (LDA) at the single cell level. Our intuition was that the diversity of the training data, in terms of cell categories and range of batch effects, makes the LDA classifier space robust. We validated the models in multiple rounds of training and testing, each round with the imaging data of one cell type (i.e., a specific cell line or PDX) designated as the test-set, while the rest of the data was used as the training set (Fig. 2.2A). Hence, the discriminative model was trained with information fully independent of the cell type it was tested on (Jones, 2019).

The number of cells from each category was balanced during training to eliminate sampling bias. To overcome the limited statistical power due to the small number of cell types (two melanocytes, four clonal expansions, six cell lines and nine PDXs), we also considered test datasets defined by all cells from one cell type imaged in one day. In this case, the training dataset included the remainder of all imaging data, except cells of any type imaged on the same day or cells of the same type on any other day (Fig. S4A). These

approaches were successful in discriminating transformed melanoma cell lines from non-transformed melanocyte cell lines (**Fig. 2.2B-D, Fig. S4B-C**), melanoma cell lines from clonal expansions of these cell lines (**Fig. 2.2E-G, Fig. S4D-E, Methods**), and melanoma cell lines from patient-derived xenografts (PDX) (**Fig. 2.2H-J, Fig. S4F-G**). We also found that in pairwise comparisons most cell types could be discriminated from one another (Fig. S4H). Our latent space descriptor surpassed simple shape-based descriptors attained by phase contrast single cell segmentation (Winter et al., 2016), and it did not benefit from either explicit incorporation of temporal information or mean square displacement analysis of trajectories (Methods, Figs. S5). Based on these findings we used the time-averaged latent space cell descriptors as the basic feature set for cell classification throughout the remainder of our study.

Although the classification performance was moderate at the single cell level (e.g., AUC of cell lines versus PDXs was 0.71, **Fig. 2.2H**), each imaging session included enough cells to accurate categorize cells at the population level (e.g., 14/15 successful cell lines versus PDXs predictions at the population level, **Fig. 2.2I**). Altogether, these results established that the latent cell descriptor captures information on the functional cell state that is distinct for different cell categories and types.

Figure 2.2. **Discrimination of different melanoma cell categories**: melanoma cell line versus melanocytes (B-D), cell lines versus clonal expanded cell lines (E-G), and cell lines versus PDXs (H-J). (**A**) Blinding the cell type. A cell type was defined as a specific cell line or PDX. Categories encompass multiple cell types. Multiple rounds of training and testing were performed. In each round, data from one cell type was used as the test dataset, defining a single observation that was composed of many single cell classifications. The training set contained the rest of the data relevant for the task (e.g., all melanoma cell lines and all PDXs when discriminating these two categories). The trained model was completely blind to the cell type used in each test set. The trained model classified each single cell in the test set. (**B**) Receiver-Operator Characteristic (ROC) curve for the distinction of the category 'cell lines' from the category 'melanocytes'. AUC = 0.635. (**C**) Accuracy in predicting for a cell type its association with the category 'cell lines' versus the category 'melanocytes'. Each data point indicates the outcome of testing a particular cell type by the fraction of individual cells classified as 'cell line'. N = 8 cell types: 6 melanoma cell lines, 2 melanocyte lines. 7/8 successful predictions. Wilcoxon rank-sum and Binomial statistical tests on the null hypothesis that the classifier scores of a cell line and of melanocytes are drawn from the same distribution, p = 0.071 (Wilcoxon), p = 0.035 (Binomial), see Methods for justification of the statistical tests. (**D**) Bootstrap distribution of the prediction of a cell type as a member of the 'cell lines' category. For each cell type, we generated 1000 observations by repeatedly selecting 20 random cells and recorded the fraction of these cells that were classified as 'cell lines'. Horizontal line – median. Wilcoxon rank-sum test $p < 0.0001$ rejecting the null hypothesis that the classifiers scores of observations from the two categories stem from the same distribution. This analysis demonstrated the ability to discriminate cell lines versus melanocytes from random samples of 20 cells in a cell type. (**E**) ROC curve for the distinction of the category 'cell lines' from the category 'clonal' (expansion line). (**F**) Accuracy in predicting for a cell type its association with the category 'cell lines' versus the category 'clonal'. Each data point indicates the outcome of testing a particular cell type by the fraction of individual cells classified as 'cell line'. N = 10 cell types: 6 melanoma cell lines, 4 clonal expansion lines. 10/10 successful predictions. Wilcoxon rank-sum and Binomial statistical test on the null hypothesis that the classifier scores of a cell line and of a clonal expansion line are drawn from the same distribution, p = 0.010 (Wilcoxon), $p < 0.001$ (Binomial). (**G**) Bootstrap distribution of the prediction of a cell type as a member of the 'cell lines' category. See panel D. Horizontal line - median. Wilcoxon rank-sum test $p < 0.0001$ rejecting the null hypothesis that the classifiers scores of observations from the two categories stem from the same distribution. (**H**) ROC curve for the distinction of the category 'cell lines' from the category 'PDXs'. AUC = 0.714. (**I**) Accuracy in predicting for a cell type its association with the category 'cell lines' versus the category 'PDXs'. Each data point indicates the outcome of testing a particular cell type by the fraction of individual cells classified as 'cell line'. N = 15 cell types: 6 cells lines, 9 PDXs. 14/15 successful predictions. Wilcoxon rank-sum and Binomial statistical test on the null hypothesis that the classifier scores of cell lines and of PDX are drawn from the same distribution, $p < 0.0004$ (Wilcoxon), $p < 0.0005$ (Binomial). (**J**) Bootstrap distribution of the prediction of a cell type as a member of the 'cell lines' category. See panel D. Horizontal line – median. Wilcoxon rank-sum test $p < 0.0001$ rejecting the null hypothesis that the classifiers scores of observations from the two categories stem from the same distribution. For all panels we used the time-averaged latent space vector over the entire movie as a cell's descriptor.

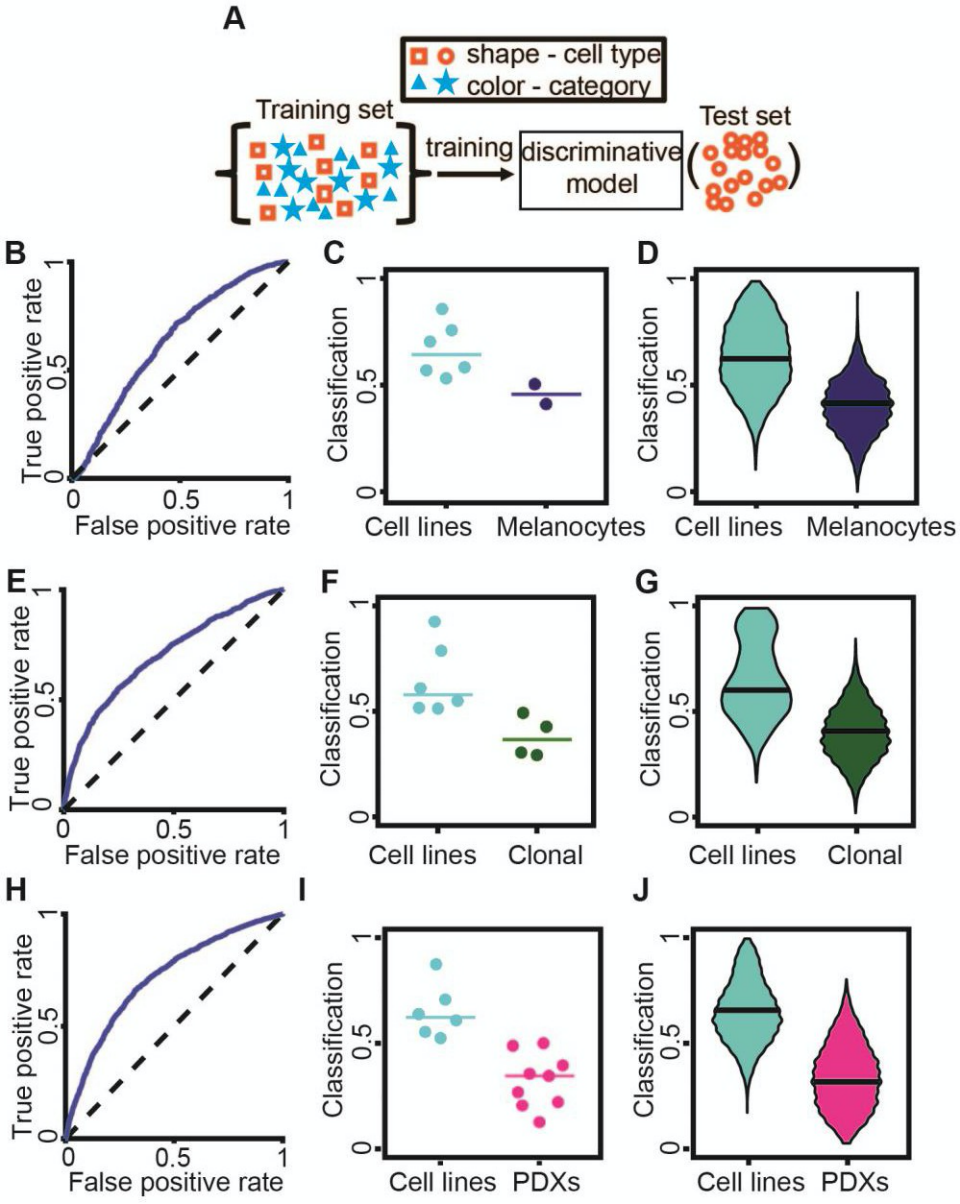
A
shape - cell type
color - category
Training set
training
discriminative model
Test set
B
True positive rate
False positive rate
C
Classification
Cell lines
Melanocytes
D
Classification
Cell lines
Melanocytes
E
True positive rate
False positive rate
F
Classification
Cell lines
Clonal
G
Classification
Cell lines
Clonal
H
True positive rate
False positive rate
I
Classification
Cell lines
PDXs
J
Classification
Cell lines
PDXs

Classification of melanoma metastatic efficiency

Equipped with the latent space cell descriptors and LDA classifiers, we tested our ability to predict the metastatic efficiency of single cells from melanoma stage III PDXs (**Fig. 2.3A**). Our approach was able to perfectly discriminate between the categories melanomas with high versus low metastatic efficiency (**Fig. 2.3B-D**). It was also successful at distinguishing single cells from PDXs with low versus high metastatic efficiency that were imaged on a single day (small n), by classifiers that were blind to the PDX and to the day of imaging (**Fig. S4A, Fig. 2.3E-G**). Cell shape information (Fig. S6A) and mean square displacement analysis of trajectories (Fig. S6B-C) could not stratify PDXs along these two categories. Classifiers trained with the latent space cell descriptor were robust to artificial blurring (**Fig. 2.3H**), and illumination changes (**Fig. 2.3I**). These results established the potential of the proposed imaging and analytical pipeline as a diagnostic, live cytometry approach.

Figure 2.3. **Discrimination of PDXs with low versus high metastatic efficiency as defined by the correlation between outcomes in mouse and man** (**A**) (Quintana et al., 2012). Classifiers were trained to predict metastatic efficiency at the single cell level (panels B, E). The association of a particular PDX with either the category 'Low' [metastatic efficiency] or the category 'High' [metastatic efficiency] was determined at the population level – either considering the fraction of all cells of a PDX predicted as 'Low' (C, F) or a bootstrap sample of 20 cells (D, G). (**B**) Receiver Operating Characteristic (ROC) curve for single cell classification. AUC = 0.71. (**C**) Accuracy in predicting for a single PDX (cell type) its association with the category 'Low' versus the category 'High'. Each data point indicates the outcome of testing a particular cell type by the fraction of individual cells classified as 'Low'. N = 7 PDXs: 4 low efficiency, 3 high efficiency metastasizers. 7/7 predictions are correct. Wilcoxon rank-sum and Binomial statistical test on the null hypothesis that the classifier scores of PDX with low versus high metastatic efficiency are drawn from the same distribution, $p = 0.0571$ (Wilcoxon), $p \leq 0.00782$ (Binomial), see Methods for justification of the statistical tests. (**D**) Bootstrap distribution of the prediction of a PDX as a member of the 'Low' category. For each PDX we generated 1000 observations by repeatedly selecting 20 random cells and recorded the fraction of these cells that were classified as 'Low'. Horizontal line - median. Wilcoxon rank-sum test $p < 0.0001$ rejecting the null hypothesis that the classifiers scores of observations from the two categories stem from the same distribution. This analysis demonstrated the ability to predict metastatic efficiency from samples of 20 random cells. (E-G) Discrimination results using classifiers that were blind to the cell type and day of imaging (Fig. S4A, more observations, smaller n - number of cells for each observation). (**E**) Receiver Operating Characteristic (ROC) curve; AUC = 0.723. (**F**) Accuracy in predicting for one PDX on a particular day (cell type) its association with the category 'Low' versus the category 'High'. Each data point indicates the outcome of testing one PDX on a particular day by the fraction of individual cells classified as 'Low'. N = 49 cell types and days: 25 low metastatic efficiency, 24 high metastatic efficiency. 32/49 predictions were correct. Wilcoxon rank-sum and Binomial statistical test on the null hypothesis that the classifier scores of PDX with low versus high metastatic efficiency are drawn from the same distribution $p = 0.0042$ (Wilcoxon), $p \leq 0.0222$ (Binomial). (**G**) Bootstrap distribution of the prediction of a PDX imaged in one day as member of the 'Low' category. See panel D. Horizontal line - median. Wilcoxon rank-sum test $p < 0.0001$ rejecting the null hypothesis that the classifiers scores of observations from the two categories stem from the same distribution. (**H**) Robustness of classifier against image blur. Blur was simulated by filtering the raw images with Gaussian kernels of increased size. The PDX m528 was used to compute AUC changes as a function of blur. Representative blurred image (middle) and its reconstruction (bottom). (**I**) Robustness of classifier to illumination changes. AUC as a function of altered illumination (top). Representative image of m528 cell after simulated illumination alteration (middle), and its reconstruction (bottom).

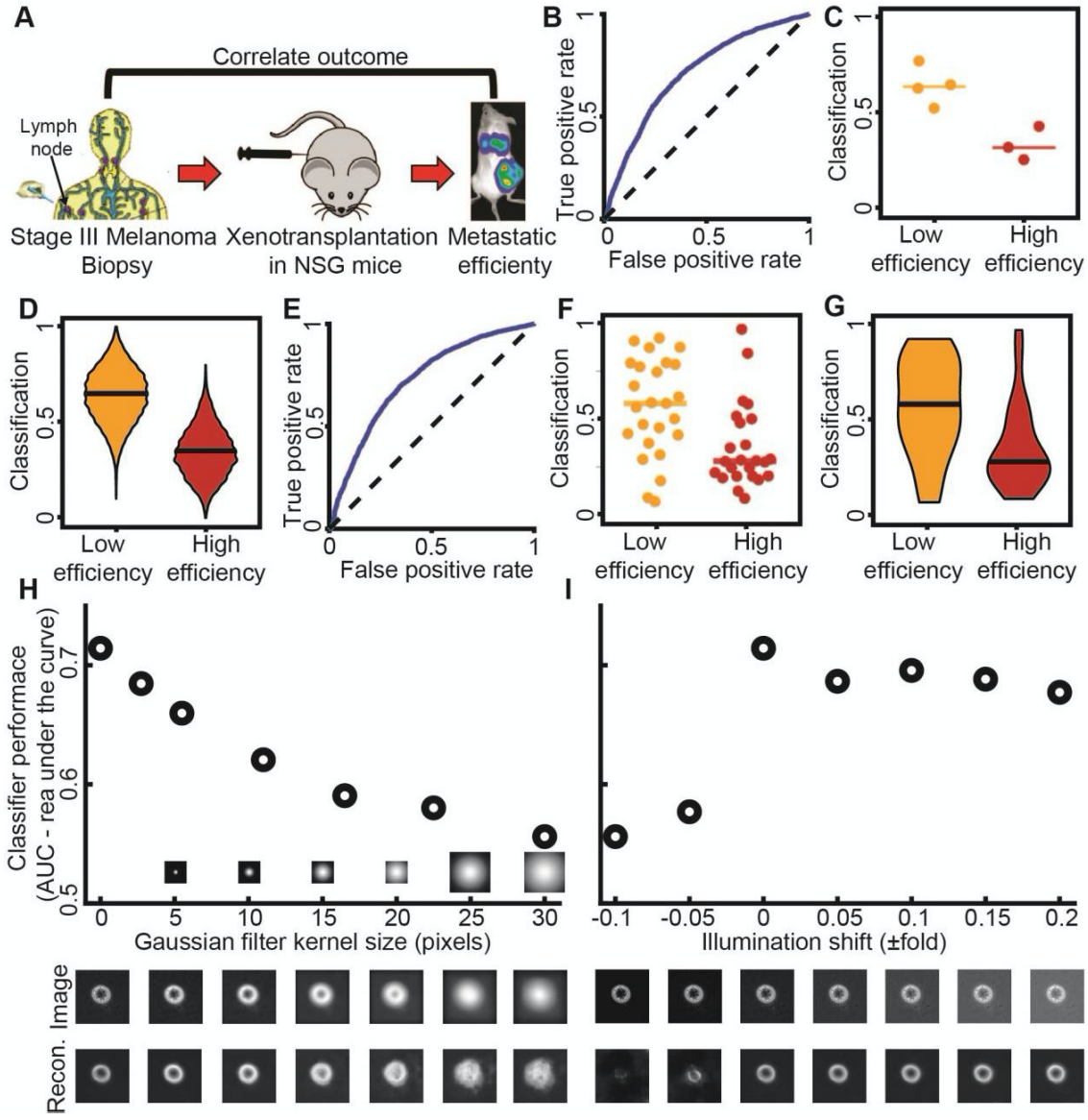
A
Correlate outcome
Lymph node
Stage III Melanoma Biopsy
Xenotransplantation in NSG mice
Metastatic efficienty
B
True positive rate
False positive rate
C
Classification
Low efficiency
High efficiency
D
Classification
Low efficiency
High efficiency
E
True positive rate
False positive rate
F
Classification
Low efficiency
High efficiency
G
Classification
Low efficiency
High efficiency
H
Classifier performace (AUC - rea under the curve)
Gaussian filter kernel size (pixels)
I
Illumination shift (±fold)
Image
Recon.

Identification of classification-driving features in autoencoder latent space

Our results thus far established the predictive power of the latent cell descriptor for the diagnosis of metastatic potential. However, the power of these deep networks to recognize statistically meaningful image patterns that escape the attention of a human observer is also its biggest weakness (Belthangady and Royer, 2019; Caicedo et al., 2017; Chandrasekaran et al., 2020): What is the information extracted in the latent space that drives the accurate classification of low versus high metastatic PDXs? When we plotted a series of cell snapshots from one PDX in rank order of the LDA-based classifier score of metastatic efficiency, there was no pattern that could intuitively explain the score shift (**Fig. 2.4A**). This outcome was not too surprising given that much of the cell appearance is likely unrelated to metastasis-enabling functions, including the image signals associated with batch effects (Boyd et al., 2020) (Fig. S3).

To probe which features encapsulated in the latent cell descriptor are most discriminative of the metastatic state we first correlated each of the 56 features to the classifier score (**Fig. 2.4B-C**). The correlations were calculated independently for each PDX using a classifier blind to the PDX (**see Fig. 2.2A**). For all 7 PDXs the last feature #56 stood out as highly negatively correlated

to the classifier scores (**Fig. 2.4C-D**). The correlation values fell outside the range of correlations observed for any other feature (**Fig. 2.4E-F**). The distributions of values of feature #56 for individual cells clearly separated tumors with high versus low metastatic efficiency (**Fig. 2.4G & H**). However, as with the classifier score (**Fig. 2.4A**), a series of random cell snapshots from one PDX in rank order of feature #56 values did not reveal a cell image pattern that could intuitively explain the meaning of this feature (**Fig. 2.4I**). This suggests that feature #56 encoded a multifaceted image property reflecting the metastatic potential of melanoma PDXs that cannot readily be grasped by visual inspection.

Figure 2.4. **Metastatic efficiency is encoded by a single component of the latent space cell descriptor.** (**A**) Gallery of snapshots of cells from a PDX (m610) ordered by their corresponding classifier score. (**B**) Approach: Each feature in the latent space cell descriptor is correlated with the score of the classifier trained to distinguish PDXs with high versus low metastatic efficiency. (**C**) Correlation between all 56 features (y-axis) and classifier scores for 7 PDXs (x-axis). (**D**) Value of feature #56 and classifier scores for individual cells color-grouped by PDX. (**E**) Distribution of the correlations from panel B; feature #56 (red arrow) is an obvious outlier. Left: distribution. Right: plot of log frequency for better visualization of feature #56. (**F**) Normalized correlation values (Z-scores) all 56 features (y-axis) and classifier scores (x-axis). Z-scores are calculated using the mean value and standard deviation of the distribution of correlation values in panel D. (**G**) Distribution of feature #56 values for cells grouped by association with a PDX. (**H**) Distribution of feature #56 values for cells grouped by association with low and high metastatic efficiency. (**I**) Gallery of snapshots of cells from PDX m610 in ascending order of the normalized value of feature #56. Note, high metastatic efficiency relates to negative, low metastatic efficiency to positive values of feature #56.

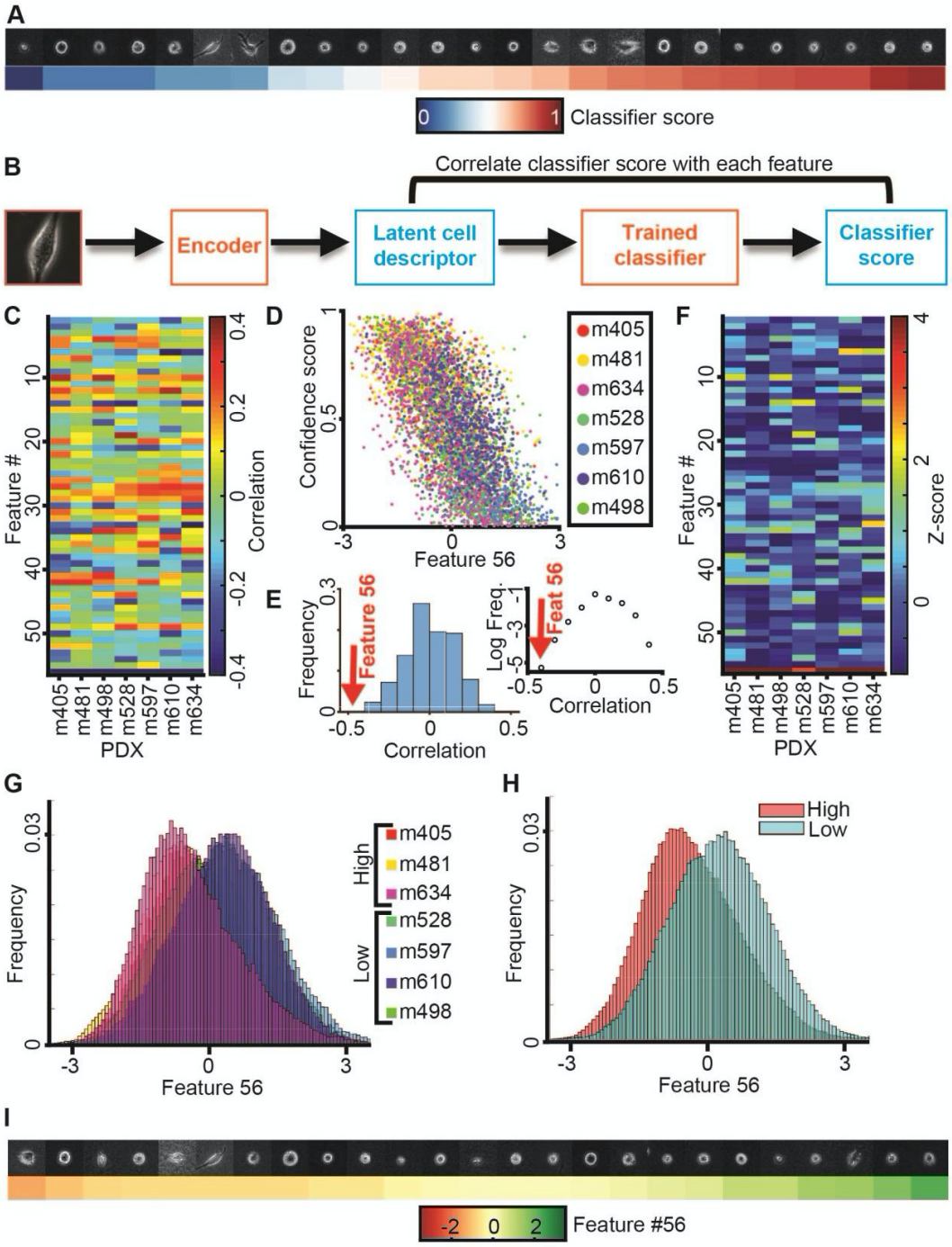
A
0
1
Classifier score
B
Correlate classifier score with each feature
Encoder
Latent cell descriptor
Trained classifier
Classifier score
C
Feature #
PDX
m405
m481
m498
m528
m597
m610
m634
Correlation
D
Confidence score
Feature 56
m405
m481
m634
m528
m597
m610
m498
E
Feature 56
Frequency
Correlation
Feat 56
Log Freq.
F
Feature #
PDX
Z-score
G
Frequency
Feature 56
High
Low
H
High
Low
Frequency
Feature 56
I
-2
0
2
Feature #56

Interpretation of classification-driving latent feature using generative models and spontaneous cell plasticity

Neither a series of cell images rank-ordered by classification scores of high vs low metastatic efficiency nor a series rank-ordered by feature #56 offered a visual clue as to which image properties may determine a cell's metastatic efficiency. We concluded that the natural variation of feature #56 values in our data was too low to give such clues and/or that the natural variation of features unrelated to metastatic efficiency largely masked image shifts related to the variation of feature #56 between PDXs with low and high metastatic efficiency. To glean some of the image properties that are controlled by feature #56 we exploited the network decoder to generate a series of "in silico" cell images in which, given a particular location of a cell in the latent space, feature #56 was gradually altered while fixing all other features (**Fig. 2.5A**). As expected, the changes in feature #56 negatively correlated with the changes they caused in the classifier score, regardless of the metastatic efficiency of the cells from which the images were derived (**Fig. 2.5B**). The generative modeling brought two advantages over our previous attempts of visually interpreting feature #56: First, it allowed us to observe 'pure' image changes along a principal axis of metastatic efficiency change. Second, it allowed us to shift the value of feature #56 outside the value range of the natural distribution and thus to analyze the

exaggerated cell images for emergent properties in cell appearance. Upon morphing a PDX cell classified as low metastatic efficiency within a normalized z-score range for feature #56 of [-3.5, 3.5], we observed two properties emerging with the high metastatic efficiency domain. The formation of pseudopodial extensions and changes in the level of cellular light scattering as observed by brighter image intensities at the cell periphery and interior (**Fig. 2.5C**). The pseudopodial activity was visually best appreciated when compiling the morphing sequences into videos that shift a cell classified as low metastatic towards the high metastatic efficiency domain (Video S5) and, vice versa, a cell classified as highly metastatic towards the low metastatic efficiency domain (Video S6).

Repeating the morphing for many PDX cells (Fig. S7, Video S7) underscores pseudopod formation and enhanced light scattering as the systematic factors that distinguish cells with low feature #56 values/high metastatic efficiency from those with high feature #56 values/low metastatic efficiency. Moreover, by variation of all other latent space features one-by-one we visually confirmed this combination of morphological properties was specifically controlled by feature #56 (Fig. S8).

To corroborate our conclusion from synthetic images we tested whether "plastic" cells, which change their classifier score during the time course of acquisition from low to high efficiency or vice versa, displayed visually identifiable image transitions. First, we verified that temporal fluctuations in feature #56 negatively correlated with the temporal fluctuations in the classifier scores (**Fig. 2.5D-F**). Second, we confirmed that PDX cells spontaneously transitioning from a predicted low to a predicted high metastatic efficiency displayed increased light scattering (**Fig. 2.5G, Video S8**). We were not able to conclusively validate the enhanced protrusive activity in the time courses of experimental data. The subtlety and perhaps also the subcellular localization of this phenotype requires visualization outside the natural variation of the latent feature space.

Figure 2.5. **Generative modeling of cell images to interpret the meaning of feature #56**. (**A**) Approach: alter feature #56 while fixing all other features in the latent space cell descriptor to identify interpretable cell image properties encoded by feature #56. (**B**) Shifts in feature #56 (y-axis, measured in z-score) negatively correlated with variation in the classifier scores. (**C**) In silico cells generated by decoding the latent cell descriptor of a representative m498 PDX cell under gradual shifts in feature #56 ("Recon."). Visualization of the intensity differences between consecutive virtual cells (Izscore - Izscore+0.5), only positive difference values are shown ("Diff+"). Changes in feature #56 are indicated in units of the z-score. The corresponding classifier's score and value of feature #56 are shown. (**D**) Approach: correlating temporal fluctuations of each feature to fluctuations in the classifiers' score. (**E**) Summary of correlations. Y-axis - different classifiers for each PDX. X-axis - features. Bin (x,y) records the Pearson correlation coefficients between temporal fluctuations in feature #x and the score of classifier #y over all cells of the PDX. (**F**) Normalization of correlation coefficients as a Z-score. Mean value and standard deviation are derived from the correlation values in panel E. (**G**) Following a m610 PDX cell spontaneously switching from the low to the high metastatic efficiency domain (as predicted by the classifier). Live imaging for 10 minutes. Left (top-to-bottom): raw cell image, diff+ images, classifier's score, feature #56 values. Right: visualization of the classifier score as a function of time, switching from "low" to "high" in less than 10 minutes.

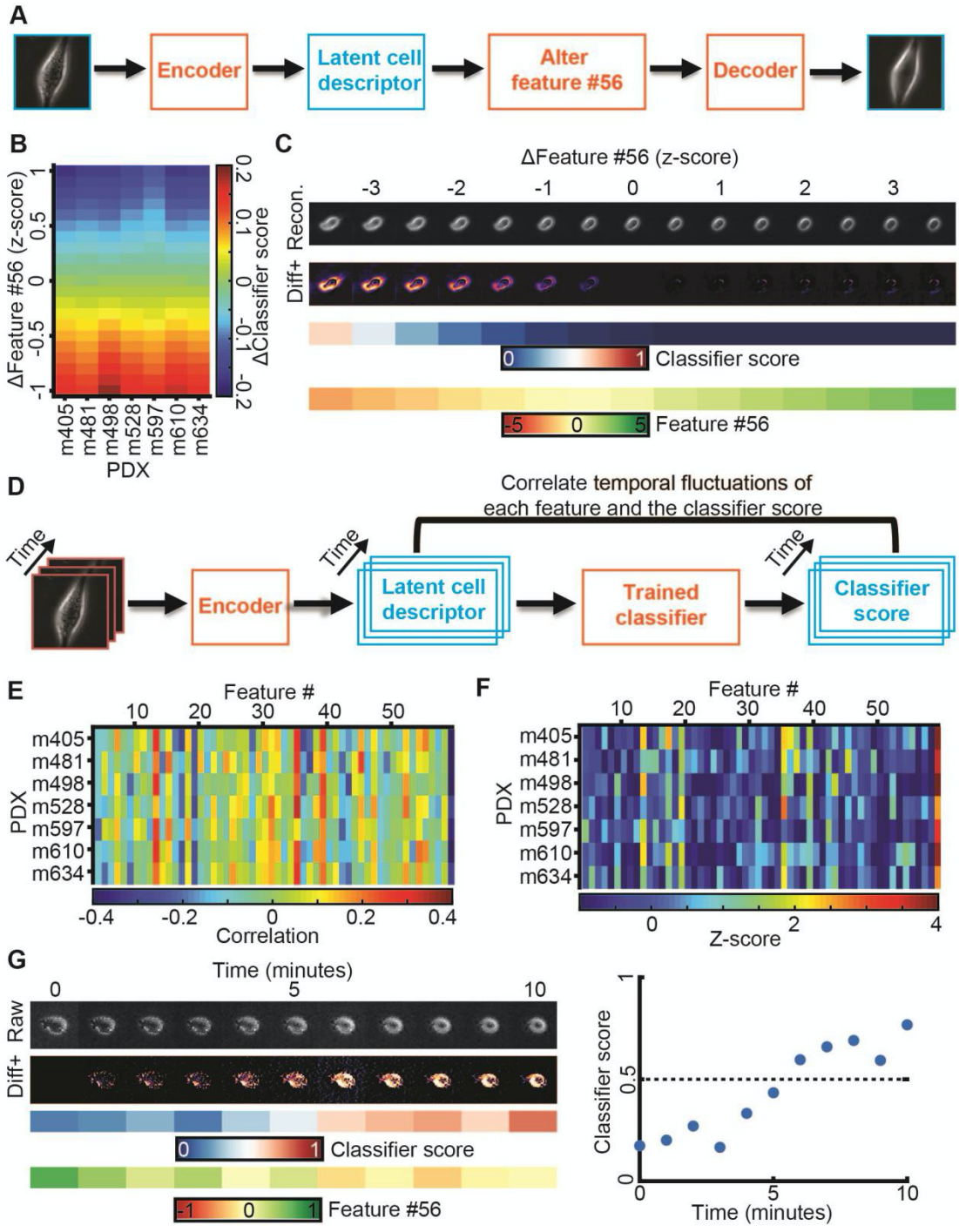
A
Encoder
Latent cell descriptor
Alter feature #56
Decoder
B
ΔFeature #56 (z-score)
ΔClassifier score
m405
m481
m498
m528
m597
m610
m634
PDX
C
ΔFeature #56 (z-score)
Recon.
Diff+
Classifier score
Feature #56
D
Correlate temporal fluctuations of each feature and the classifier score
Time
Encoder
Latent cell descriptor
Trained classifier
Classifier score
E
Feature #
PDX
Correlation
F
Feature #
PDX
Z-score
G
Time (minutes)
Raw
Diff+
Classifier score
Feature #56
Classifier score
Time (minutes)

Generalizing the interpretation to high dimensions

When we applied the same feature-to-score correlation analysis to classifiers trained for discrimination of cell lines from PDXs, we found the three features #26, #27, and #36 as classification-driving (Fig. S9A-B). This result underscores two key properties of our interpretation of the latent space: First, distinct classification tasks are driven by different feature subsets in the latent space cell descriptor, which capture distinguishing cell properties. In all generality, the classification task is driven not by a single but by multiple latent space cell descriptors. To enable interpretation of such multi-feature drivers, we generalized the traversal of the latent space by computing a trajectory that follows in every location the gradient of the classifier score. Since LDA is a linear classifier, the gradient follows throughout the entire latent space the directions determined by the classifier coefficients (Fig. S9C-D). Thus, we traversed the latent space up and down in steps that are weighted by the LDA coefficients (Methods). For the classifier distinguishing PDXs from cell lines, the latent space traversal to positions beyond the natural variation in the data suggests that PDX cells exhibit a wider range of non-round morphologies than cell lines (Fig. S9E). However, for one cell the simulated PDX image outside the natural data range displays an artefactual

break-up of the cell volume, indicating an example of occasional failure of the described extrapolation strategy.

As a second test case, we trained another (unsupervised) adversarial autoencoder (**Fig. 2.1C**) to capture an alternative latent space representation of cell appearance. The network training was performed on the same dataset of PDXs, cell lines, clones and melanocyte images as the first network, and was followed by training LDA classifiers to discriminate between high and low metastatic efficient PDXs, each blind to the PDX in test. Because of the stochasticity in selecting mini-batches, the training converged to a different latent space cell image representation. In this representation, several features, and not only feature #56, correlated with the classifier score (Fig. S10A), as also reflected by multiple LDA coefficients with high magnitudes (Fig. S10B-C). Tracing PDX cells along the LDA coefficients to latent space locations outside the natural variation of the data confirmed light scattering and pseudopodial extensions as the determinants between cells with high versus low metastatic efficiency by shifting feature #56 in the latent representation determined by the original autoencoder network (compare Fig. S10D). These results establish the generalization of in silico latent features amplification to higher-dimensional discriminant feature sets.

PDX-trained classifier can predict the metastatic potential of melanoma cell lines in mouse xenografts

We were interested in the capacity of PDX-trained classifiers to predict the spontaneous metastasis of tumor-forming melanoma cell line xenografts. We hypothesized that, despite the distinct morphologies of PDX and cell lines indicated by the classifier in **Fig. 2.2H-J**, the core differentiating properties between low and high efficiency metastatic PDXs would be conserved for melanoma cell lines. Using the PDX-trained classifiers, A375, a BRAFV600E-mutated and NRAS wild-type melanoma cell line, originally excised from a primary malignant tumor (Davies et al., 2002; Ghandi et al., 2019; Giard et al., 1973; Kozlowski et al., 1984; Rozenberg et al., 2010; Tanami et al., 2004), was predicted as the most aggressive metastasizer (**Fig. 2.6A**). MV3, a BRAF wild-type and NRAS-mutated melanoma cell line, originally excised from a metastatic lymph node and described as highly metastatic (Quax et al., 1991; Schrama et al., 2008; van Muijen et al., 1991), was predicted by the PDX-trained classifiers as the least aggressive (**Fig. 2.6A**). Consistent with our previous analyses of the influence of the latent space features on classification, feature #56 was lower for A375 than for MV3 (**Fig. 2.6B**). We subcutaneously injected luciferase-labeled versions of A375 and MV3 cells into the flanks of NSG mice (Methods). Both cell models formed robust

primary tumors at the site of injection (**Fig. 2.6C-D**) as well as metastases in the lungs and in multiple other remote organs (**Fig. 2.6E-F**). Bioluminescence imaging of individual excised organs showed a higher spreading to organs other than the lungs in mice injected with A375 cells compared to those injected with MV3 cells (**Fig. 2.6E-F**). It was previously determined that the most robust measure of metastatic efficiency in this model was visually identifiable macrometastases in organs other than the lungs (Quintana et al., 2012). As confirmation that the A375 cells metastasized more efficiently in this model, we found macrometastases in other organs in 5/5 mice xenografted with A375 cells versus in 1/5 mice xenografted with MV3 cells (**Fig. 2.6G**). Intriguingly, primary tumors in MV3-injected mice grew much faster than in A375-injected mice (**Fig. 2.6H**), in contrast to being less aggressive in spreading to remote organs, suggesting that primary tumor growth is uncoupled from the ability to produce remote metastases (Ganesh et al., 2020; Quintana et al., 2012; Viceconte et al., 2017). Under the assumption that overall tumor burden would be limiting for metastatic dissemination instead of time after injection, we conclude, in agreement with the prediction of our classifier, that A375 cells are more metastatically efficient than MV3 cells in this model. Broadly, these data confirm that properties captured by the latent space cell descriptor define a specific

gauge of the metastatic potential of melanoma that is independent of the tumorigenic potential.

Figure 2.6. **PDX-trained classifiers predict the potential for spontaneous metastasis of mouse xenografts from melanoma cell lines**. (**A**) All 7 PDX-trained classifiers consistently predicted that among the 6 analyzed cell lines A375 has the highest and MV3 the lowest metastatic efficiency. (**B**) The distribution of single cell values of feature #56 is lower for A375 than the distribution of values for MV3 cells. (**C, E**) Bioluminescence (BLI) of NSG mouse sacrificed 24-35 days after subcutaneous transplantation of 100 Luciferase-GFP+ cells from the A375 melanoma cell line (C) versus from the MV3 cell line (E). (**D, F**) Bioluminescence of organs dissected from the A375 xenografted mouse (D) and from the MV3-xenografted mouse (F). 1, Gastrointestinal Tract (GI); 2, Lungs and Heart; 3, Pancreas and Spleen; 4, Liver; 5, Kidneys and Adrenal glands. In the MV3, mouse metastases were mostly found in the lungs. Black shades are mats on which the organs and mice are imaged (Methods). (G) Summary of metastatic efficiency for A375 and MV3 melanoma cell lines in 5 mice. "BLI Lungs": Detection of BLI in the lungs. "BLI other organs": BLI in multiple organs beyond the lungs. "Remote macro mets": Macrometastases in remote organs (excluding lungs), identification of "visceral metastasis", macrometastases visually identifiable without BLI, the measure used to define metastatic efficiency to the PDXs in (Quintana et al., 2012). (H) Primary tumors in MV3 xenografts grow faster than in A375 xenografts. Mice were sacrificed 24 days after injection with MV3, 35 days after injection with A375 cells. N = 5 mice for A375 and MV3 cell line. Statistics for tumor size after 24 days p-value = 0.0079 (Wilcoxon rank-sum test), fold = 1.6241.

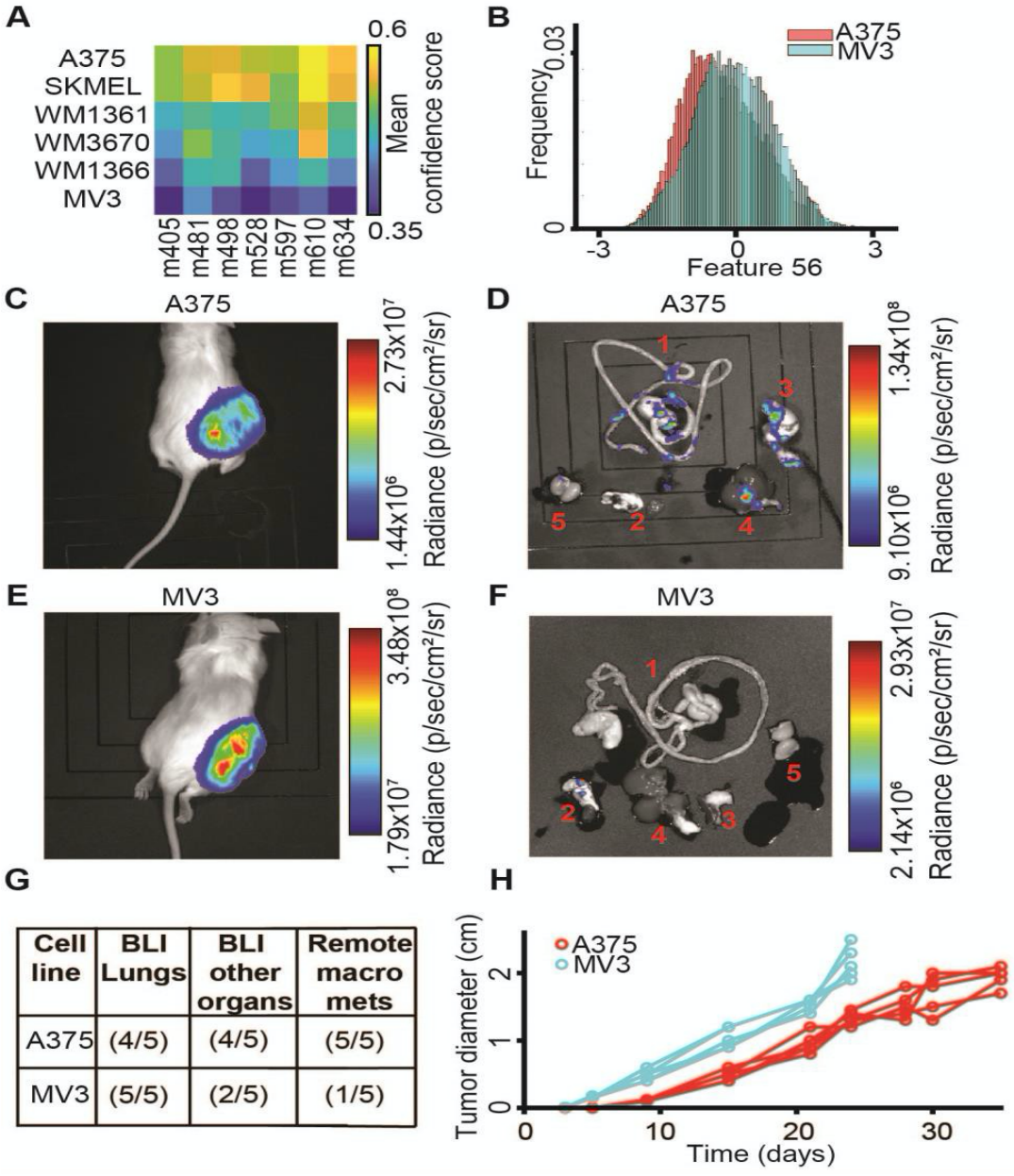

Cell line	BLI Lungs	BLI other organs	Remote macro mets
A375	(4/5)	(4/5)	(5/5)
MV3	(5/5)	(2/5)	(1/5)

Image-based classifiers are more predictive of metastatic potential than the mutational profile

Following initial diagnosis, it is standard practice for a melanoma biopsy to undergo mutational sequencing analysis to determine the best course of therapy. But, to our knowledge it has not been determined if there is a general mutational profile associated with more aggressively metastatic disease. While metastatic melanoma are expected to harbor a 'standard' set of primary mutations, such as those in BRAF or NRAS (Jakob et al., 2012) – and indeed all our PDX models and metastatic cell lines do contain an activating mutation in either one of these genes (Table S2) – we were curious as to whether secondary mutations in the genomic profiles of these cell models would encode information on the metastatic efficiency. To address this question we examined the distributions of genomic distances among the PDX cell models and two cell lines vis-à-vis the distance distributions in the latent feature space. The conclusion from these experiments was that the states of oncogenic/likely-oncogenic mutations in the 20 most mutated genes in melanoma (Hodis et al., 2012) were insufficient for a prediction of the metastatic efficiency (Fig. S11). In fact, the oncogenic/likely-oncogenic mutations in the genes were not more predictive than non-oncogenic mutations or an unbiased analysis of a full panel of 1400 genes for metastatic states. Thus, image-based classifiers can identify more metastatically

aggressive cancers, which is not currently possible for clinical diagnostics based on genomics.

Discussion

Visually unstructured properties of cell image appearance enable robust cell type classification

Morphology has long been a cue for cell biologists and pathologists to recognize cell category and abnormalities related to disease (Bakal et al., 2007; Chan, 2014b; Eddy et al., 2018; Gordonov et al., 2015; Gurcan et al., 2009; López, 2013b; Pavillon et al., 2018; Wu et al., 2020; Yin et al., 2013). In this study, we rely on the exquisite sensitivity of deep learned artificial neural networks in recognizing subtle but systematic image patterns to classify different cell categories and cell states. To assess this potential we chose phase contrast light microscopy, an imaging modality that uses simple transmission of white or monochromatic light through an unlabeled cell specimen and thus minimizes experimental interference with the sensitive patient samples that we used in our study. A further advantage of phase contrast microscopy is that the imaging modality captures visually unstructured properties, which relate to a variety of cellular properties,

including surface topography, organelle organization, cytoskeleton density and architecture, and interaction with fibrous extracellular matrix.

Our cell type classification rests on the combination of an unsupervised deep learned autoencoder for extraction of meaningful but visually hidden features followed by conventional supervised classifier that discriminates between distinct cell categories. The choice of this two-step implementation allowed us to construct several different cell classifiers for different tasks using a one-time learned, common feature space. Thus, the task of distinguishing, for example, melanoma cell lines from normal melanocytes could benefit from the information extracted from PDXs, while PDXs could be divided into groups with high versus low metastatic propensity with the support of information extracted from melanoma cell lines and untransformed melanocytes. Accordingly, sensitive classifiers could be trained on relatively small data subsets – much smaller than would be required to train an *ab initio* deep-learned classifier for the same task. The approach is not only data-economical, but it greatly reduces computational costs as the deep learning procedure is performed only once on the full dataset. Indeed, in our study we learned a single latent feature space using time lapse sequences from over 12,000 cells (~1.7 million snapshots); and then trained classifiers on data subsets that included labeled

categories smaller than 1,000 cells. As an additional benefit of the orthogonalization of unsupervised feature extraction and supervised classifier training, we were able to evaluate the performance of our classifiers by repeated leave-one-out validation, verifying that the discriminative model training is completely independent of the cell type at test. A similar evaluation strategy, requiring the repeated re-training of a deep learned classifier, would likely become computationally prohibitive.

Application of cell type classification to the prediction of metastatic efficiency

Among the cell classification tasks, we were able to distinguish the metastatic efficiency of stage III melanoma harvested from a xenotransplantation assay that had previously been shown to maintain the patient outcome (Quintana et al., 2012). While the distinction was perfect at the level of PDXs, at the single cell level the classifier accuracy dropped to 70%. This is not necessarily a weakness of the classifier but speaks to the fact that tumor cells grown from a single cell clone are not homogeneous in function and/or appearance. Our estimates of classifier accuracy relies on leave-one-out strategies where the training set and the test set were completely non-overlapping, both with regards to the classified cell

category and to the days the classified category was imaged. Thus, it can be assumed that the reported accuracies can be reproduced on new, independent PDXs.

Besides numerical testing, we validated the accuracy of our classifiers high versus low metastatic efficiency in a fully orthogonal experiment. We applied the PDX-trained classifiers to predict the metastatic efficiency of well-established melanoma cell lines and validated their predictions in mouse xenografts. We emphasize that the PDX-trained classifier has never encountered a cell line and that despite the significant differences between cell lines and PDXs (**Fig. 2.2H-J**), the classifier correctly predicted high metastatic potential for the cell line A375 and low potential for MV3 (**Fig. 2.6**). Moreover, a recent paper that demonstrated the use of in vivo barcoding as a readout for metastatic potential of cancer cell lines engrafted in mice showed that A375 is more aggressive than SKMEL2 (Jin et al., 2020), in agreement with our classifier's prediction (**Fig. 2.6A**). Intriguingly, the aggressiveness in primary tumor growth was reversed between A375 and MV3, supporting the notion that tumorigenesis and metastasis are unrelated phenomena (Ganesh et al., 2020; Jin et al., 2020; Quintana et al., 2012; Viceconte et al., 2017) (**Fig. 2.6H**). This shows that the latent feature space encodes cell properties that specifically contribute to cell functions required

for metastatic spreading and that these features are orthogonal to features that distinguish cell lines from PDX models.

Interpretation of latent features discriminating high and low metastatic cell propensity

Deep Learning Artificial Neural Networks have revolutionized machine learning and computer vision as powerful tools for complex pattern recognition, but there is increasing mistrust in results produced by 'black-box' neural networks(Belthangady and Royer, 2019). Aside from increasing the confidence, the interpretation of the properties – also referred to as 'mechanisms' – of the pattern recognition process can potentially generate insight of a biological/physical phenomenon that escapes the analysis driven by human intuition.

In medical imaging the quest for interpretability has been responded by identifying image sub-regions of special importance for trained deep neural networks (Ash et al., 2018; Courtiol et al., 2019; Cruz-Roa et al., 2013; Fu et al., 2019; Pan et al., 2019; Shamai et al., 2019). A similar idea was implemented in fluorescent microscopy images, in the context of classification of protein subcellular localization, to visualize the supervised

network activation patterns (Kraus et al., 2017). Localization of sub-regions that were particularly important for the classifier result permitted a visual assessment and pathological interpretation of distinctive image properties. Such approaches are only suitable when the classification-driving information is localized in one image region over another, and when highlighting the region is sufficient to establish a biological hypothesis. For cellular phenotyping, this is not the case. Because of the orthogonalization of feature space construction and classifier training we could elegantly extract visual cues for the inspection of classifier-relevant cell appearances. By exploiting the single cell variation of the latent feature space occupancy and the associated variation in the scoring of a classifier discriminating high from low metastatic melanoma, we identified feature #56 as predominant in prescribing metastatic propensity. Of note, the feature-to-classifier correlation analysis is not restricted to determining a single discriminatory feature (Fig. S9, S10) and is directly applicable to non-linear classifiers.

Visual inspection of cell images ranked by the classifier score or feature #56 did not reveal any salient cell image appearance that would distinguish efficiently from inefficiently metastasizing cells (**Fig. 2.4A,I**). These particular image properties were masked by cell appearances that are unrelated to the metastatic function. Moreover, the function-driving feature

#56 represents a nonlinear combination of multiple image properties that are not readily discernible. To test whether feature #56 encodes image properties that are human-interpretable but buried in the intrinsic heterogeneity of cell image appearances, we exploited the generative power of our autoencoder. We 'shifted' cells along the latent space axis of feature #56 while leaving the other 55 feature values fixed. The approach also allowed us to examine how cell appearances would change with feature #56 values outside the natural range of our experimental data. Hence, the combination of purity and exaggeration allowed us to generate human discernible changes in image appearance that correspond to a shift in metastatic efficiency.

The outcome of a single feature, i.e., feature #56, driving the classification between two cell categories is by chance. As we show for the classification of PDXs versus cell lines, multiple features may strongly correlate with the classifier score. In this case, interpretation by visual inspection of exaggerated images has to be achieved by traversing the latent space in trajectories that follow in every location the gradient of the classifier score. In the particular case of the LDA classifier, the gradient is spatially invariant and follows the combination of the LDA coefficients. Thus, the proposed

mechanism of visual latent space interpretation does not hinge on the identification of a single driver feature.

Once exaggerated in silico images offered a glimpse of key image properties distinguishing efficient from inefficient metastasizers, we could validate the predicted appearance shifts in experimental data. This was especially important to exclude the possibility that our extrapolation of feature values introduced image artifacts. We screened our data set for cells whose classification score and feature #56 values drifted from a low to high metastatic state or vice versa. We supposed that during such spontaneous dynamic events the variation in cell image appearances would be dominated, for a brief time window, by the variation in feature #56 and only marginally influenced by other features. Therefore, time-resolved data may present transitions in cell image appearance comparable to those induced by selective manipulation of latent space values along the direction of feature #56. It is highly unlikely to find a similarly pure transition between a pair of cells, explaining why we were unable to discern differences between cells with low and high metastatic efficiency in feature #56 ordered cell image series (**Fig 2.4A**).

Analyses of appearance shifts in both exaggerated in silico images and selected experimental images unveiled cellular properties of highly metastatic melanoma. First, these cells seemed to form pseudopodial extensions (**Fig. 2.5C, Fig. S7, Video S5, Video S6**). Because of its subtlety, this phenotype was more difficult to discern visually during spontaneous transitions of cell states (**Fig. 2.5G**). Second, images of cells in a highly metastatic state displayed brighter cell peripheral and interior signals, indicative of alteration in cellular light scattering. Because light scattering affects the image signal globally, this phenotype was clearly apparent in simulations (**Fig. 2.5C, Fig. S7, Video S5, Video S6**) and in experimental time lapse sequences of transitions between cells states (**Fig. 2.5G, Video S8**). Neither one of the two cell phenotypes follows a mathematically intuitive formalism that could be implemented as an ab initio feature detector. This highlights the power of deep learned networks in extracting complex cell function-driving image appearances.

Pseudopodial extensions play critical roles in cell invasion and migration. However, at least in a simplified migration assay in tissue culture dishes, the highly metastatic cell population did not exhibit enhanced migration (Fig. S6). Recent work has suggested mechanistic links between enhanced branched actin formation in lamellipodial and enhanced cell

cycle progression (Mohan et al., 2019; Molinie et al., 2019), especially in micro-metastases. Therefore, we offer as a hypothesis that the connection between pseudopod formation and metastatic efficiency predicted by our analysis relates to the lamellipodia-driven upregulation of proliferation and survival signals (Nikolaou and Machesky, 2020; Swaminathan et al., 2020).

The observation that light scattering can indicate metastatic efficiency suggests that the cellular organelles and processes captured by light scattering are relevant to the metastatic process (Schürmann et al., 2015). Indeed, differences in light scattering upon acetic acid treatment are often used to detect cancerous cells in patients (Marina et al., 2012). Although the mechanisms underlying light scattering of cells are unclear, intracellular organelles such as phase separated droplets (Falke et al., 2019) or lysosomes will be detected by changes to light scattering (Choi et al., 2007). With the establishment of our machine-learning based classifier, we are set to systematically probe the intersection of hypothetical metastasis-driving molecular processes, actual metastatic efficiency, and cell image appearance in follow-up studies.

Acknowledgements

Chapter 2, in full, is a reprint of the material as it appears in Cell Systems 2021. Zaritsky, Assaf*; Jamieson, Andrew R.*; Welf, Erik S.*; Nevarez, Andres*; Cillay, Justin; Eskiocak, Ugur; Cantarel, Brandi L.; Danuser, G. Interpretable deep learning uncovers cellular propertiesin label-free live cell images that are predictive of highly metastatic melanoma. The dissertation author was the co-primary investigator and author of this paper.

This work was supported by the Cancer Prevention and Research Institute of Texas (CPRIT R160622 to GD), the National Institutes of Health (R35GM126428 to GD; K25CA204526 to ESW), and the Israeli Council for Higher Education (CHE) via Data Science Research Center, Ben-Gurion University of the Negev, Israel (to AZ). We thank Sean Morrison for PDX-derived cell models. We thank Andrew R. Cohen for LEVER.

Author Contributions

Conceptualization, A.Z., E.S.W. and G.D.; Methodology, A.Z., A.R.J., and E.S.W.; Software, A.R.J.; Formal Analysis, B.L.C.; Investigation, A.Z., A.R.J., A.N., and J.C.; Resources, U.E.; Writing – Original Draft, A.Z.; Writing – Review & Editing, A.Z., A.R.J., A.N., E.W.S. and G.D.; Supervision, G.D.; Funding Acquisition, G.D.

Declaration of Interests

The authors declare no competing interests.

Inclusion and diversity

One or more of the authors of this paper self-identifies as an underrepresented ethnic minority in science. One or more of the authors of this paper self-identifies as living with a disability. One or more of the authors of this paper received support from a program designed to increase minority representation in science.

STAR Methods

RESOURCE AVAILABILITY

Lead contact: Further information and requests for resources and reagents should be directed to and will be fulfilled by the Lead Contact, Assaf Zaritsky (assafza@bgu.ac.il) or Gaudenz Danuser (gaudenz.Danuser@utsouthwestern.edu).

Materials Availability: This study did not generate new materials.

Data and Code Availability:

Raw image data, raw single cell images, corresponding metadata, the trained neural network, and the feature representation of all cells source data have been deposited at the Image Data Resource (Williams et al., 2017), https://idr.openmicroscopy.org, and are publicly available under the accession numbers: idr0109.

- Original source code and test data is publicly available at https://github.com/DanuserLab/openLCH (doi: https://doi.org/10.5281/zenodo.4619858)
- Scripts used to generate the figures presented in this paper are not provided in this paper but are available from the Lead Contact on request.

- Any additional information required to reproduce this work is available from the Lead Contact.

METHOD DETAILS

Patient-derived xenograft (PDX) melanoma cells

Populations of primary melanoma cells were created from tumors grown in murine xenograft models as described previously (Quintana et al., 2010). Briefly, cells were suspended in Leibovitz's L-15 Medium (ThermoFisher) containing mg/ml bovine serum albumin, 1% penicillin/streptomycin, 10 mM HEPES and 25% high protein Matrigel (product 354248; BD Biosciences). Subcutaneous injections of human melanoma cells were performed in the flank of NOD.CB17-*Prkdc*^{scid} *Il2rg*^{tm1Wjl}/SzJ (NSG) mice (Jackson Laboratory). These experiments were performed according to protocols approved by the animal use committees at the University of Texas Southwestern Medical Center (protocol 2011-0118). After surgical removal, tumors were mechanically dissociated and subjected to enzymatic digestion for 20 min with 200 U ml−1 collagenase IV (Worthington), 5 mM CaCl2, and 50 U ml−1 DNase at 37oC. Cells were filtered through a 40 μm cell strainer to break up cell clumps and washed through the strainer to remove cells from large tissue pieces.

Cell culture and origin

Cell cultures were grown on polystyrene tissue culture dishes to confluence at 37°C and 5% CO2. Melanoma cells derived from murine PDX models were gifts from Sean Morrison (UT Southwestern Medical Center, Dallas, TX) and cultured in medium containing the Melanocyte Growth Kit and Dermal Cell Basal Medium from ATCC. Primary melanocytes were obtained from ATCC (PCS-200-013) and grown in medium containing the Melanocyte Growth Kit and Dermal Cell Basal Medium from ATCC. The m116 melanocytes, a gift from J. Shay (UT Southwestern Medical Center, Dallas), were derived from fetal foreskin and were cultured in medium 254 (Fisher). A375 cells were obtained from ATCC (CRL-1619). SK-Mel2 cells were obtained from ATCC (HTB-68). MV3 cells were a gift from Peter Friedl (MD Anderson Cancer Center, Houston, TX). MV3 and A375 cells were cultured in DMEM with 10% FBS. WM3670, WM1361, and WM1366 were obtained directly from the Wistar Institute and cultured in the recommended medium (80% MCDB1653, 20%, 2% FBS, CaCl2 and bovine insulin).

PDX-derived cell culture

We found that melanoma cell cultures derived from PDX tumors exhibited variable responses to traditional cell culture practices. Although

some of the cell cultures retained high viability and proliferated readily, others exhibited extensive cell death and failed to proliferate. We determined that frequent media changes (<24 hrs) and subculturing only at high (>50%) confluence dramatically increased the viability and proliferation of PDX-derived cell cultures. Although we observed no correlation between metastatic efficiency and robustness in cell culture, we followed these general cell culture practices for all PDX-derived cultures.

Clonal cell line experiments

To create cell populations "cloned" from a single cell, cells were released from the culture dish via trypsinization and passed through a cell strainer (Fischer; 07-201-430) to ensure single-cell solution, counted and then seeded on a 10 cm polystyrene tissue culture dish at low density of 350,000 cells/10 ml of phenol-red free DMEM. Single cells were identified via phase-contrast microscopy. The single cells were isolated using cloning rings (Sigma; C1059) and expanded within the ring. For clonal medium changes, the medium was aspirated within the cloning rings. Subsequently, conditioned medium from a culture dish with corresponding confluent cells were passed through a filter (Fischer; 568-0020), which removed any cells and cell debris and then added to each cloning ring. Once confluent within the cloning

ring, the clonal populations were released via trypsinization inside the cloning ring, transferred to individual cell culture dishes, and allowed to expand until confluence.

Bioluminescence imaging of NSG mice with melanoma cell lines

Injection of melanoma cells, monitoring of mice, dissection of mice, and imaging were all done as described in Quintana & Piskounova et al. (Quintana et al., 2012). Briefly, 100 Luciferase-GFP+ cells were injected into the right flank. Mice were monitored until the tumor at the site of injection reached 2 cm in diameter. Mice injected with MV3 were sacrificed 24 days after injection and A375 sacrificed 35 days after injection. The stomach, gut, rectum, and esophagus were labeled as the gastrointestinal tract. The black shades are mats that were used to image the mice's organs. Some mouse/organ images have mats with (Fig. 6D) and without (Fig. 6F) gridlines.

Quantification of metastatic efficiency in NSG mice

We used three measures to assess metastatic efficiency (Quintana et al., 2012). First, detection of BLI in the lungs. Second, detection of BLI in multiple organs beyond the lungs. Third, identification of "visceral metastasis", macrometastases visually identifiable without BLI, see details in

(Quintana et al., 2012). We refrained from a more quantitative analysis of the BLI intensity for two reasons: 1) cells from some tumors lose expression of luciferase and 2) differences in melanin expression in melanoma cells and in tissue absorption can affect luminescence independent of cell density.

Targeted sequencing cancer-related genes and copy number variation analysis

Targeted sequencing of exons of 1385 cancer-related genes was performed by the Genomics and Molecular Pathology Core at UT Southwestern Medical Center as previously described (Zhang et al., 2020). Sequencing was performed on 6 out of 7 PDXs and the two cell lines A375 and MV3. Due to the difficulty in expanding the cells of PDX m528 in culture, we were not able to sequence this PDX. From the raw variant calling files, high confidence variants were determined by filtering variants found to have (a) strand bias, (b) depth of coverage < 20 reads and alt allele frequency < 20%. Common variants were filtered if they were in > 1% allele frequency in any population (Karczewski et al., 2020). Oncogenic potential was assess using oncokb-annotator (https://github.com/oncokb/oncokb-annotator). Summary tables of high-confidence variants of melanoma PDXs and cell lines were assembled in Table S2.

Live cell imaging

Live cell phase contrast imaging was performed on a Nikon Ti microscope equipped with an environmental chamber held at 37oC and 5% CO2 in 20x magnification (pixel size of 0.325μm). In order to prevent morphological homogenization and to better mimic the collagenous ECM of the dermal stroma, we imaged cells on top of a thick slab of collagen. Collagen slabs were made from rat tail collagen Type 1 (Corning; 354249) at a final concentration of 3 mg/mL, created by mixing with the appropriate volume of 10x PBS and water and neutralized with 1N NaOH. A total of 200 μL of collagen solution was added to the glass bottom portion of a Gamma Irradiated 35MM Glass Bottom Culture Dish (MatTek P35G-0-20-C). The dish was then placed in an incubator at 37°C for 15 minutes to allow for polymerization.

Cells were seeded on top of the collagen slab at a final cell count of 5000 cells in 400 uL of medium per dish. This solution was carefully laid on top of the collagen slab, making sure not to disturb the collagen or spill any medium off of the collagen and onto the plastic of the MatTek dish. The dish was then placed in a 37°C incubator for 4 hours. Following incubation, one mL of medium was gently added to the dish. The medium was gently stirred

to suspend debris and unattached cells. The medium was then drawn off and gently replaced with two mL of fresh medium.

Single cell detection and tracking

We took advantage of the observation that image regions associated with "cellular foreground" had lower temporal correlation than the background regions associated with the collagen slab because of their textured and dynamic nature. This allowed us to develop an image analysis pipeline that detected and tracked cells without segmenting the cell outline. This approach allowed us to deal with the vast variability in the appearance of the different cell models and batch imaging artifacts in the phase-contrast images. The detection was performed in super-pixels with a size equivalent to a 10 x 10 μm patch. For each patch in every image, we recorded two measurements, one temporal- and the other intensity-dependent (see details later), generating two corresponding downsampled images reflecting the local probability of a cell being present. We used these as input to a particle tracking software, which detected and tracked local maxima of particularly high probability (Aguet et al., 2013). The first measurement captures the patch's maximal spatial cross-correlation from frame *t* to frame *t+1* within a search radius that can capture cell motion up

to 60 μm/hour. The second measurement used the mean patch intensity in the raw image to capture the slightly brighter intensity of cells in relation to the background in phase-contrast imaging. Notably, our reduced resolution in the segmentation-free detection and tracking approach would break for imaging in higher cell densities. A bounding box of 70 x 70 μm around each cell was defined and used for single cell segmentation and feature extraction (details will follow). We excluded cells within 70μm from the image boundaries to avoid analyzing cells entering or leaving the field of view and to avoid the characteristic uneven illumination in these regions. Tracking of single cells over 8 hours was performed manually using the default settings in CellTracker v1.1 (Piccinini et al., 2016).

Unsupervised feature extraction with Adversarial Autoencoders

We have developed an unsupervised, generative representation for capturing cell image features using Adversarial Autoencoders (AAE) (Goodfellow et al., 2014; Makhzani et al., 2015). The autoencoder learns a compressed representation of cell images by encoding the images using a series of convolution and pooling layers leading ultimately to a lower dimensional embedding, or latent space. Points in the embedding space can then be decoded by a symmetric series of layers flowing in the opposite

direction to reconstruct an image that, once trained, ideally appears nearly identical to the original input (Hinton et al., 2006). The training/optimization of the AAE is regularized (by using a second network during training) such that points close together in the embedding space will generate images sharing close visual resemblance/features (Makhzani et al., 2015). This convenient property can also generate synthetic/imaginary cell images to interpolate the appearance of cells from different regions of the space. We used the architecture from Johnson et al. (Johnson et al., 2017), that was based on the network presented in (Makhzani et al., 2015). Johnson's network includes an AAE that learns to reconstruct landmarks of the cell nucleus and cytoplasm. The adversarial component teaches the network to discriminate between features derived from real cells and those drawn randomly from the latent space. We trained the regularized AAE with bounding boxes of phase-contrast single cell images (of size 70μm x 70 μm, or 217 x 217 pixels) that were rescaled to 256x256 pixels. The network was trained to extract a 56-dimensional image encoding representation of cell appearance. This representation and its variation over time were used as descriptors for cell appearance and action. We adapted Torch code from https://github.com/AllenCellModeling/torch_integrated_cell (Arulkumaran, 2017; Johnson et al., 2017) for unsupervised AAEs, and adjusted it to execute on our high-performance computing cluster. Torch (Collobert et al., 2011) is

a Lua script-based scientific computing framework oriented towards machine learning algorithms with an underlying C/CUDA implementation.

The adversarial autoencoder latent vector preserves a visual similarity measure

We verified that the 56-dimensional latent vector preserves a visual similarity measure for cell appearance, i.e., increasing distances between two data points in the latent space correspond to increasing differences between the input images. We first validated that variations in the latent vector cause variations in cell appearances (Fig. S2A). To accomplish this we numerically perturbed the latent vector after encoding a cell image with varying amounts of noise and calculated the mean squared error between the raw and reconstructed images. As expected, the mean squared error between reconstructed and raw images monotonically increased with increasing amount of noise added in the latent space (Fig. S2B). Hence, the trained encoder generates a locally differentiable latent space. Second, we interpolated a linear trajectory in the latent space between two experimentally observed cells, as well as between two random points, and confirmed, visually and quantitatively, that the decoded images gradually transform from one image to the other (Fig. S2C-D, Video S9). Hence, the

trained encoder generates a latent space without discontinuities. Third, we calculated the latent space distances between a cell at time *t* and the same cell at *t*+100 minutes and between a cell at time *t* and a neighboring cell in the same sample at time *t*. The distances between time-shifted latent space vectors for the same cell were shorter than those between neighboring cells (Fig. S2E). Hence, the combined effects of time variation in global imaging parameters and of morphological changes on displacements in the latent space tend to be smaller than the difference between cells.

Determining batch effects (inter-day variability)

In the case of the presented label-free imaging assay, batch effects may arise from uncontrolled experimental variables such as variations in the properties of the collagen gel, illumination artifacts, or inconsistencies in the phase ring alignment between sessions. Autoencoders are known to be very effective in capturing subtle image patterns. Therefore, they may pick up batch effects that mask image appearances related to the functional state of a cell. Under the assumption that intra-patient/cell line variability in image appearance is less than inter-patient/cell line appearance, we expect the latent cell descriptors of the same cell category on different days to be more

similar than the descriptors of different cell categories imaged on the same day.

To test how strong batch effects may be in our data, we simultaneously imaged four different PDXs in an imaging session that we replicated on different days. Every cell was represented by the time-averaged latent space vector over the entire movie. We then computed the Euclidean distance as a measure of dissimilarity between descriptors from the *same* PDX imaged on *different days* to the distribution of Euclidean distances between *different* PDXs imaged on the *same* day (Fig. S3A). For three of the four tested PDXs we could not find a clear difference between the intra-PDX/inter-day similarity and the intra-day/inter-PDX similarity (Fig. S3B). Only PDX m610 displayed greater intra-PDX/inter-day similarity than intra-day/inter-PDX similarity. Consistent with this assessment, visualization of all time-averaged cell descriptors over all PDXs and days using PCA (Jolliffe, 2011) or tSNE (Maaten and Hinton, 2008) projections neither showed cell clusters associated with different PDXs nor with different imaging days, except for m610 (Fig. S3C-D). These results suggest that the latent space cell descriptors are impacted by both experimental batch effects and putative differences in the functional states between PDXs.

Single cell segmentation in phase-contrast imaging and shape feature extraction

To compare the performance of the deep-learned cell descriptors to conventional, shape-based descriptors of cell states (Bakal et al., 2007; Goodman and Carpenter, 2016; Gordonov et al., 2015; Pascual-Vargas et al., 2017; Scheeder et al., 2018; Sero and Bakal, 2017; Yin et al., 2013) we segmented phase contrast cell images of multiple cell types with diverse appearances.

Label-free cell segmentation is a challenging task, especially in the diverse landscape of shapes and appearance of the different melanoma cell systems we used. We used the LEVER (Winter et al., 2016) (downloaded from https://git-bioimage.coe.drexel.edu/opensource/lever), a designated phase-contrast cell segmentation algorithm to segment single cells within the bounding boxes identified by the previously described segmentation-free cell tracking. Briefly, the LEVER segmentation is based on minimum cross entropy thresholding and additional post-processing. While the segmentation was not perfect, it generally performed robustly to cells from different origins and varied imaging conditions (Fig. S5A-B). We used MATLAB's function *regionprops* to extract 13 standard shape features from

the segmentation masks produced by LEVER. These included: Area, MajorAxisLength, MinorAxisLength, Eccentricity, Orientation, ConvexArea, FilledArea, EulerNumber, EquivDiameter, Solidity, Extent, Perimeter, PerimeterOld.

Encoding temporal information

We compared three different approaches to incorporating temporal information when using either the autoencoder-based representation or the shape-based representation of cell appearance (Fig. S5C). First, static snapshot images ignoring the temporal information. Second, averaging the cell static descriptors along a cell's trajectory, canceling noise for cells that do not undergo dramatic changes. Notably, the resulting cell descriptor matches the static descriptor in size and features. Accordingly, classifiers that were trained on average temporal descriptors could be applied to static snapshot descriptors (see Figs. 4-5). In the third encoding we relied on the 'bag of words' (BOW) approach (Sivic and Zisserman, 2009), in which each trajectory is represented by the distribution of discrete cell states, termed 'code words'. A 'dictionary' of 100 code words was predetermined by k-means clustering (MacQueen, 1967) on the full dataset of cell descriptors.

We found that purely shape-based descriptors could not distinguish cell lines from PDXs (Fig. S5D). This indicates that the autoencoder latent space captures information from the phase-contrast images that is missed by the shape features. Incorporation of temporal information, especially the time-averaging, slightly (but significantly) boosted the classification performance of LDA models derived from latent space cell descriptors (Fig. S5E). This outcome is consistent with computer vision studies concluding that explicit modeling of time may lead to only marginal gains in classification performance (Karpathy et al., 2014).

Dimensionality reduction

We used tSNE (Fig. S3C) and PCA (Fig. S3D) for dimensionality reduction. Each cell was represented by its time-averaged descriptors in the latent space. For tSNE we used a GPU-accelerated implementation, https://github.com/CannyLab/tsne-cuda (Chan et al., 2018).

Discrimination analysis

We used Matlab's vanilla implementation of Linear Discriminant Analysis (LDA) for the discrimination tasks (Figs. 2-3) and to identify the cellular phenotypes that correlate with low or high metastatic efficiency (Figs. 4-5).

The feature vector for each cell was given by the normalized latent cell descriptor extracted by the autoencoder. Normalization of each latent cell descriptor component to a z-score feature was accomplished as follows. The mean (μ) and standard deviation (σ) of a latent cell descriptor component were calculated across the full data set of cropped cell images and used to calculate the corresponding z-score measure: $x_{norm} = (x - \mu)/\sigma$, i.e., the variation from the mean values in units of standard deviation that can later be compared across different features.

For each classification task, the training data was kept completely separate from the testing data. Training and testing sets were assigned according to two methodologies. First, hold out all data from one cell type and train the classifier using all other cell types (Fig. 2A). Second, hold out all data from one cell type imaged in one day as the test set ("cell type - day", e.g., Fig. 3F) and train the classifier on all other cell types excluding the data imaged on the same day as the test set (Fig. S4A). This second approach trained models that had never seen the cell type or data imaged on the same day of testing. In both classification settings we balanced the instances from each category for training by randomly selecting an equal number of observations from each class. This scheme was used for classification tasks involving categories containing more than one cell type: cell lines versus

melanocytes, cell lines versus clonally expanded cell lines, cell lines versus PDXs, low versus high metastatic efficiency in PDXs (Figs. 2-3). For statistical analysis, all the cells in a single test set are considered as a single independent observation. Hence, "cell type - day" testing sets provide more independent observations (N) at the cost of fewer cells imaged in each day compared to testing set of the form of "cell type".

We used bootstrapping to statistically test the ability to predict metastatic efficiency from samples of 20 random cells. This was performed for "cell type" (Fig. 3D) or "cell type - day" (Fig. 3G) test sets. For each test set, we generated 1000 observations by repeatedly selecting 20 random cells (with repetitions), recorded the fraction of these cells that were classified as low efficiency and the 95% confidence interval of the median. Statistical significance in all settings was inferred using two statistical tests using each test set classifier's mean score: (1) The nonparametric Wilcoxon signed-rank test, considering the null hypothesis that the classifiers scores of observations from the two categories stem from the same distribution; (2) The Binomial test, considering the null hypothesis that the classifier prediction is random in respect to the ground truth labels. For inference of phenotypes that correlate with metastatic efficiency (Fig. 5) we used the classifier that was trained on the mean latent cell description along its trajectory (which

proved to be superior to training with single snapshots) on latent cell descriptors derived from single snapshots, which hold the same, just noisier features.

The area under the Receiver Operating Characteristic (ROC) curve was recorded to assess and compare the discriminative accuracy of different tasks (Figs. 2-3). The true-positive rate (TPR) or sensitivity is the percentage of "low" metastatic cells classified correctly. The false-positive rate (FPR) or (1-specificity) is the percent of "high" metastatic cells incorrectly classified as "low". Area under the ROC curve (AUC) was used as a measure of discrimination power. Note that the scores of all cells from all relevant cell types were pooled together for this analysis. Different classifiers can produce different scores, which means that our analysis provides a lower bound (pessimistic estimation). ROC analysis could not be applied for individual (held-out) test sets because they consist of only a single ground truth label.

We used the web-application PlotsOfData (Postma and Goedhart, 2019) to generate all boxplots.

In silico traversal weighted according to LDA coefficients

To generalize the in silico cell image amplification to multiple features, we traversed the high dimensional latent space according to the corresponding LDA coefficients. More specifically, we moved up/down the classifier's score gradient by adding/subtracting multiples of one standard deviation of the unit vector weighted according to the LDA classifier coefficients.

Correlating classifier scores to genomic mutation markers

We calculated a distance matrix to assess the similarity between all pairs of PDXs and the cell lines A375 and MV3. The distances were calculated in terms of the classifier score and of genomic mutation panels. m528 was excluded from the analysis due missing sequencing data (see above). For the distance matrix of the classifier score, we calculated the Jensen-Shannon (JS) divergence (Lin, 1991) between the distributions of single cell classifier scores using the corresponding PDX-based classifiers (see discrimination analysis section in the Methods). For the cell lines, a new classifier was trained using all cells from all seven PDXs. This classifier was used to determine the classifier score for A375 and MV3. For each cell type, the

distribution was approximated with a 25 bin histogram. JS divergence was calculated on pairs of cell type classifier score distributions.

To calculate distance matrices based genomic mutations we considered three panels of established melanoma genomic mutation markers. Two genomic mutation panels were derived from variation of exomes associated with 1385 cancer-related genes (see above). Mutations in commonly mutated genes in melanoma (Hodis et al., 2012) were annotated using OncoKB (Chakravarty et al., 2017) and divided into (i) oncogenic or likely oncogenic (Table S3, Fig. S11B) and (ii) benign or unannotated ("non-oncogenic") (Table S4, Fig. S11C). Mutational based genetic distances were derived by converting mutation scores to a binary state (1=presence, 0=absence) and computing the Jaccard index (Jaccard, 1912) between cell types. In Fig. S11D we calculated distances using MASH (Ondov et al., 2016), which compared the K-mer profiles between samples, thus giving a distance of the raw sequence data, without biases introduced in the alignment and variant calling analysis.

The distance matrices derived from classifier scores and mutational states were correlated (Pearson correlation) to assess whether the genomic

mutation state and image-derived classifier scores for low and high metastatic efficacies were linked.

QUANTIFICATION AND STATISTICAL ANALYSIS

For each classification task, the training data was kept completely separate from the testing data. For statistical analysis, all the cells in a single test set were considered as a single independent observation. We used bootstrapping to statistically test the ability to predict a category from samples of 20 random cells (Fig. 2D, Fig. 2G, Fig. 2J, Fig. 3D, Fig. 3G). Statistical significance in category classification of "cell type" (Fig. 2C, Fig. 2F, Fig. 2I, Fig. 3C) or "cell type - day" (Fig. 3F, Fig. S4C, Fig. S4E, Fig. S4G) was inferred using two statistical tests. (1) The nonparametric Wilcoxon signed-rank test, considering the null hypothesis that the classifiers scores of observations from the two categories stem from the same distribution; (2) The Binomial test, considering the null hypothesis that the classifier prediction is random in respect to the ground truth labels. The purpose of testing two different null hypotheses was to increase thoroughness, especially given the small sample sizes (number of cell types). Statistical significance of discrimination using cell shape and temporal information (Fig. S5D-F, Fig. S6A) was inferred using the Wilcoxon signed-rank test. Full details on the statistical issues can be found in

sub-section entitled Discrimination analysis in the Methods. Statistical details of all experiments can be found in the figure legends including the statistical tests used, exact value of n, and clear descriptions of what n represents.

References

Aguet, F., Antonescu, C.N., Mettlen, M., Schmid, S.L., and Danuser, G. (2013). Advances in analysis of low signal-to-noise images link dynamin and AP2 to the functions of an endocytic checkpoint. Developmental cell *26*, 279-291.
Arulkumaran, K. (2017). Autoencoders.

Ash, J.T., Darnell, G., Munro, D., and Engelhardt, B.E. (2018). Joint analysis of gene expression levels and histological images identifies genes associated with tissue morphology. bioRxiv, 458711.

Bakal, C., Aach, J., Church, G., and Perrimon, N. (2007). Quantitative morphological signatures define local signaling networks regulating cell morphology. Science *316*, 1753-1756.

Belthangady, C., and Royer, L.A. (2019). Applications, promises, and pitfalls of deep learning for fluorescence image reconstruction. Nature methods, 1-11.

Boutros, M., Heigwer, F., and Laufer, C. (2015). Microscopy-based high-content screening. Cell *163*, 1314-1325.

Boyd, J.C., Pinheiro, A., Del Nery, E., Reyal, F., and Walter, T. (2020). Domain-invariant features for mechanism of action prediction in a multi-cell-line drug screen. Bioinformatics *36*, 1607-1613.

Caicedo, J.C., Cooper, S., Heigwer, F., Warchal, S., Qiu, P., Molnar, C., Vasilevich, A.S., Barry, J.D., Bansal, H.S., and Kraus, O. (2017). Data-analysis strategies for image-based cell profiling. Nature methods *14*, 849.

Cantelli, G., Orgaz, J.L., Rodriguez-Hernandez, I., Karagiannis, P., Maiques, O., Matias-Guiu, X., Nestle, F.O., Marti, R.M., Karagiannis, S.N., and Sanz-Moreno, V. (2015). TGF-β-induced transcription sustains amoeboid melanoma migration and dissemination. Current biology *25*, 2899-2914.

Chakravarty, D., Gao, J., Phillips, S., Kundra, R., Zhang, H., Wang, J., Rudolph, J.E., Yaeger, R., Soumerai, T., and Nissan, M.H. (2017). OncoKB: a precision oncology knowledge base. JCO precision oncology *1*, 1-16.

Chan, D.M., Rao, R., Huang, F., and Canny, J.F. (2018). t-SNE-CUDA: GPU-Accelerated t-SNE and its Applications to Modern Data. Paper presented at: 2018 30th International Symposium on Computer Architecture and High Performance Computing (SBAC-PAD) (IEEE).

Chan, J.K. (2014a). The wonderful colors of the hematoxylin-eosin stain in diagnostic surgical pathology. Int J Surg Pathol *22*, 12-32.

Chan, J.K. (2014b). The wonderful colors of the hematoxylin–eosin stain in diagnostic surgical pathology. International journal of surgical pathology *22*, 12-32.

Chandrasekaran, S.N., Ceulemans, H., Boyd, J.D., and Carpenter, A.E. (2020). Image-based profiling for drug discovery: due for a machine-learning upgrade? Nat Rev Drug Discov.

Cheng, S., Fu, S., Kim, Y.M., Song, W., Li, Y., Xue, Y., Yi, J., and Tian, L. (2021). Single-cell cytometry via multiplexed fluorescence prediction by label-free reflectance microscopy. Science Advances *7*, eabe0431.

Choi, W., Fang-Yen, C., Badizadegan, K., Oh, S., Lue, N., Dasari, R.R., and Feld, M.S. (2007). Tomographic phase microscopy. Nature methods *4*, 717-719.

Christiansen, E.M., Yang, S.J., Ando, D.M., Javaherian, A., Skibinski, G., Lipnick, S., Mount, E., O'Neil, A., Shah, K., and Lee, A.K. (2018). In silico labeling: Predicting fluorescent labels in unlabeled images. Cell *173*, 792-803. e719.

Collobert, R., Kavukcuoglu, K., and Farabet, C. (2011). Torch7: A matlab-like environment for machine learning. Paper presented at: BigLearn, NIPS workshop.

Courtiol, P., Maussion, C., Moarii, M., Pronier, E., Pilcer, S., Sefta, M., Manceron, P., Toldo, S., Zaslavskiy, M., and Le Stang, N. (2019). Deep learning-based classification of mesothelioma improves prediction of patient outcome. Nature medicine, 1-7.

Cruz-Roa, A.A., Arevalo Ovalle, J.E., Madabhushi, A., and González Osorio, F.A. (2013). A deep learning architecture for image representation, visual interpretability and automated basal-cell carcinoma cancer detection. Med Image Comput Comput Assist Interv *16*, 403-410.

Davies, H., Bignell, G.R., Cox, C., Stephens, P., Edkins, S., Clegg, S., Teague, J., Woffendin, H., Garnett, M.J., and Bottomley, W. (2002). Mutations of the BRAF gene in human cancer. Nature *417*, 949.

Eddy, C.Z., Wang, X., Li, F., and Sun, B. (2018). The morphodynamics of 3D migrating cancer cells. arXiv preprint arXiv:180710822.

Falke, S., Brognaro, H., Martirosyan, A., Dierks, K., and Betzel, C. (2019). A multi-channel in situ light scattering instrument utilized for monitoring protein aggregation and liquid dense cluster formation. Heliyon *5*, e03016.

Fang, L., Monroe, F., Novak, S.W., Kirk, L., Schiavon, C., Seungyoon, B.Y., Zhang, T., Wu, M., Kastner, K., and Kubota, Y. (2019). Deep Learning-Based Point-Scanning Super-Resolution Imaging. bioRxiv, 740548.

Fu, Y., Jung, A.W., Torne, R.V., Gonzalez, S., Vohringer, H., Jimenez-Linan, M., Moore, L., and Gerstung, M. (2019). Pan-cancer computational histopathology reveals mutations, tumor composition and prognosis. bioRxiv, 813543.

Ganesh, K., Basnet, H., Kaygusuz, Y., Laughney, A.M., He, L., Sharma, R., O'Rourke, K.P., Reuter, V.P., Huang, Y.-H., and Turkekul, M. (2020). L1CAM defines the regenerative origin of metastasis-initiating cells in colorectal cancer. Nature Cancer *1*, 28-45.

Ghandi, M., Huang, F.W., Jané-Valbuena, J., Kryukov, G.V., Lo, C.C., McDonald, E.R., Barretina, J., Gelfand, E.T., Bielski, C.M., and Li, H. (2019). Next-generation characterization of the Cancer Cell Line Encyclopedia. Nature *569*, 503.

Giard, D.J., Aaronson, S.A., Todaro, G.J., Arnstein, P., Kersey, J.H., Dosik, H., and Parks, W.P. (1973). In vitro cultivation of human tumors: establishment of cell lines derived from a series of solid tumors. Journal of the National Cancer Institute *51*, 1417-1423.

Goodfellow, I., Pouget-Abadie, J., Mirza, M., Xu, B., Warde-Farley, D., Ozair, S., Courville, A., and Bengio, Y. (2014). Generative adversarial nets. Paper presented at: Advances in neural information processing systems.

Goodman, A., and Carpenter, A.E. (2016). High-Throughput, Automated Image Processing for Large-Scale Fluorescence Microscopy Experiments. Microscopy and Microanalysis *22*, 538-539.

Gordonov, S., Hwang, M.K., Wells, A., Gertler, F.B., Lauffenburger, D.A., and Bathe, M. (2015). Time series modeling of live-cell shape dynamics for image-based phenotypic profiling. Integrative Biology *8*, 73-90.

Guo, S.-M., Krishnan, A.P., Folkesson, J., Ivanov, I., Chhun, B., Cho, N., Leonetti, M., and Mehta, S.B. (2019). Revealing architectural order with polarized light imaging and deep neural networks. bioRxiv, 631101.

Gurcan, M.N., Boucheron, L.E., Can, A., Madabhushi, A., Rajpoot, N.M., and Yener, B. (2009). Histopathological image analysis: A review. IEEE reviews in biomedical engineering *2*, 147-171.

Hayward, N.K., Wilmott, J.S., Waddell, N., Johansson, P.A., Field, M.A., Nones, K., Patch, A.-M., Kakavand, H., Alexandrov, L.B., and Burke, H. (2017). Whole-genome landscapes of major melanoma subtypes. Nature *545*, 175.

Hinton, G.E., Osindero, S., and Teh, Y.-W. (2006). A fast learning algorithm for deep belief nets. Neural computation *18*, 1527-1554.

Hoadley, K.A., Yau, C., Hinoue, T., Wolf, D.M., Lazar, A.J., Drill, E., Shen, R., Taylor, A.M., Cherniack, A.D., and Thorsson, V. (2018). Cell-of-origin patterns dominate the molecular classification of 10,000 tumors from 33 types of cancer. Cell *173*, 291-304. e296.

Hodis, E., Watson, I.R., Kryukov, G.V., Arold, S.T., Imielinski, M., Theurillat, J.-P., Nickerson, E., Auclair, D., Li, L., and Place, C. (2012). A landscape of driver mutations in melanoma. Cell *150*, 251-263.

Jaccard, P. (1912). The distribution of the flora in the alpine zone. 1. New phytologist *11*, 37-50.

Jakob, J.A., Bassett Jr, R.L., Ng, C.S., Curry, J.L., Joseph, R.W., Alvarado, G.C., Rohlfs, M.L., Richard, J., Gershenwald, J.E., and Kim, K.B. (2012). NRAS mutation status is an independent prognostic factor in metastatic melanoma. Cancer *118*, 4014-4023.

Jin, X., Demere, Z., Nair, K., Ali, A., Ferraro, G.B., Natoli, T., Deik, A., Petronio, L., Tang, A.A., Zhu, C.*, et al.* (2020). A metastasis map of human cancer cell lines. Nature *588*, 331-336.

Johnson, G.R., Donovan-Maiye, R.M., and Maleckar, M.M. (2017). Generative Modeling with Conditional Autoencoders: Building an Integrated Cell. arXiv preprint arXiv:170500092.

Jolliffe, I. (2011). Principal component analysis (Springer).
Jones, D.T. (2019). Setting the standards for machine learning in biology. Nature Reviews Molecular Cell Biology, 1-2.

Karczewski, K.J., Francioli, L.C., Tiao, G., Cummings, B.B., Alföldi, J., Wang, Q., Collins, R.L., Laricchia, K.M., Ganna, A., and Birnbaum, D.P. (2020). The mutational constraint spectrum quantified from variation in 141,456 humans. bioRxiv, 531210.

Karpathy, A., Toderici, G., Shetty, S., Leung, T., Sukthankar, R., and Fei-Fei, L. (2014). Large-scale video classification with convolutional neural networks. Paper presented at: Proceedings of the IEEE conference on Computer Vision and Pattern Recognition.

Kozlowski, J.M., Fidler, I.J., Campbell, D., Xu, Z.-l., Kaighn, M.E., and Hart, I.R. (1984). Metastatic behavior of human tumor cell lines grown in the nude mouse. Cancer research *44*, 3522-3529.

Kraus, O.Z., Grys, B.T., Ba, J., Chong, Y., Frey, B.J., Boone, C., and Andrews, B.J. (2017). Automated analysis of high-content microscopy data with deep learning. Mol Syst Biol *13*, 924.

LaChance, J., and Cohen, D.J. (2020). Practical Fluorescence Reconstruction Microscopy for High-Content Imaging. bioRxiv.

Lin, J. (1991). Divergence measures based on the Shannon entropy. IEEE Transactions on Information theory *37*, 145-151.

López, J.I. (2013a). Renal tumors with clear cells. A review. Pathol Res Pract *209*, 137-146.

López, J.I. (2013b). Renal tumors with clear cells. A review. Pathology-Research and Practice *209*, 137-146.

Maaten, L.v.d., and Hinton, G. (2008). Visualizing data using t-SNE. Journal of machine learning research 9, 2579-2605.

MacQueen, J. (1967). Some methods for classification and analysis of multivariate observations. Paper presented at: Proceedings of the fifth Berkeley symposium on mathematical statistics and probability (Oakland, CA, USA.).

Makhzani, A., Shlens, J., Jaitly, N., Goodfellow, I., and Frey, B. (2015). Adversarial autoencoders. arXiv preprint arXiv:151105644.

Marina, O.C., Sanders, C.K., and Mourant, J.R. (2012). Effects of acetic acid on light scattering from cells. Journal of biomedical optics *17*, 085002.

Mohan, A.S., Dean, K.M., Isogai, T., Kasitinon, S.Y., Murali, V.S., Roudot, P., Groisman, A., Reed, D.K., Welf, E.S., and Han, S.J. (2019). Enhanced Dendritic Actin Network Formation in Extended Lamellipodia Drives Proliferation in Growth-Challenged Rac1P29S Melanoma Cells. Developmental cell *49*, 444-460. e449.

Molinie, N., Rubtsova, S.N., Fokin, A., Visweshwaran, S.P., Rocques, N., Polesskaya, A., Schnitzler, A., Vacher, S., Denisov, E.V., and Tashireva, L.A. (2019). Cortical branched actin determines cell cycle progression. Cell research *29*, 432-445.

Nehme, E., Weiss, L.E., Michaeli, T., and Shechtman, Y. (2018). Deep-STORM: super-resolution single-molecule microscopy by deep learning. Optica *5*, 458-464.

Nikolaou, S., and Machesky, L.M. (2020). The stressful tumour environment drives plasticity of cell migration programmes, contributing to metastasis. J Pathol *250*, 612-623.

Ondov, B.D., Treangen, T.J., Melsted, P., Mallonee, A.B., Bergman, N.H., Koren, S., and Phillippy, A.M. (2016). Mash: fast genome and metagenome distance estimation using MinHash. Genome biology *17*, 132.

Ounkomol, C., Seshamani, S., Maleckar, M.M., Collman, F., and Johnson, G.R. (2018). Label-free prediction of three-dimensional fluorescence images from transmitted-light microscopy. Nature methods *15*, 917.

Ouyang, W., Aristov, A., Lelek, M., Hao, X., and Zimmer, C. (2018). Deep learning massively accelerates super-resolution localization microscopy. Nature biotechnology *36*, 460-468.

Pan, C., Schoppe, O., Parra-Damas, A., Cai, R., Todorov, M.I., Gondi, G., von Neubeck, B., Böğürcü-Seidel, N., Seidel, S., and Sleiman, K. (2019). Deep Learning Reveals Cancer Metastasis and Therapeutic Antibody Targeting in the Entire Body. Cell *179*, 1661-1676. e1619.

Pascual-Vargas, P., Cooper, S., Sero, J., Bousgouni, V., Arias-Garcia, M., and Bakal, C. (2017). RNAi screens for Rho GTPase regulators of cell shape and YAP/TAZ localisation in triple negative breast cancer. Scientific Data *4*, 170018.

Pavillon, N., Hobro, A.J., Akira, S., and Smith, N.I. (2018). Noninvasive detection of macrophage activation with single-cell resolution through machine learning. Proceedings of the National Academy of Sciences *115*, E2676-E2685.

Piccinini, F., Kiss, A., and Horvath, P. (2016). CellTracker (not only) for dummies. Bioinformatics *32*, 955-957.

Pinner, S., and Sahai, E. (2008). Imaging amoeboid cancer cell motility in vivo. Journal of microscopy *231*, 441-445.

Postma, M., and Goedhart, J. (2019). PlotsOfData—A web app for visualizing data together with their summaries. PLoS biology *17*, e3000202.

Quax, P., Van Muijen, G., Weening-Verhoeff, E., Lund, L., Danø, K., Ruiter, D., and Verheijen, J. (1991). Metastatic behavior of human melanoma cell lines in nude mice correlates with urokinase-type plasminogen activator, its type-1 inhibitor, and urokinase-mediated matrix degradation. The Journal of cell biology *115*, 191-199.

Quintana, E., Piskounova, E., Shackleton, M., Weinberg, D., Eskiocak, U., Fullen, D.R., Johnson, T.M., and Morrison, S.J. (2012). Human melanoma metastasis in NSG mice correlates with clinical outcome in patients. Science translational medicine *4*, 159ra149-159ra149.

Quintana, E., Shackleton, M., Foster, H.R., Fullen, D.R., Sabel, M.S., Johnson, T.M., and Morrison, S.J. (2010). Phenotypic heterogeneity among tumorigenic melanoma cells from patients that is reversible and not hierarchically organized. Cancer cell *18*, 510-523.

Rozenberg, G.I., Monahan, K.B., Torrice, C., Bear, J.E., and Sharpless, N.E. (2010). Metastasis in an orthotopic murine model of melanoma is independent of RAS/RAF mutation. Melanoma research *20*, 361.

Sadok, A., McCarthy, A., Caldwell, J., Collins, I., Garrett, M.D., Yeo, M., Hooper, S., Sahai, E., Kuemper, S., and Mardakheh, F.K. (2015). Rho kinase inhibitors block melanoma cell migration and inhibit metastasis. Cancer research *75*, 2272-2284.

Sahai, E., and Marshall, C.J. (2003). Differing modes of tumour cell invasion have distinct requirements for Rho/ROCK signalling and extracellular proteolysis. Nature cell biology *5*, 711-719.

Scheeder, C., Heigwer, F., and Boutros, M. (2018). Machine learning and image-based profiling in drug discovery. Current opinion in systems biology.

Schrama, D., Keller, G., Houben, R., Ziegler, C.G., Vetter-Kauczok, C.S., Ugurel, S., and Becker, J.C. (2008). BRAFV600E mutations in malignant melanoma are associated with increased expressions of BAALC. Journal of carcinogenesis *7*, 1.

Schürmann, M., Scholze, J., Müller, P., Chan, C.J., Ekpenyong, A.E., Chalut, K.J., and Guck, J. (2015). Refractive index measurements of single, spherical cells using digital holographic microscopy. In Methods in cell biology (Elsevier), pp. 143-159.

Sero, J.E., and Bakal, C. (2017). Multiparametric analysis of cell shape demonstrates that β-PIX directly couples YAP activation to extracellular matrix adhesion. Cell systems *4*, 84-96. e86.

Shamai, G., Binenbaum, Y., Slossberg, R., Duek, I., Gil, Z., and Kimmel, R. (2019). Artificial intelligence algorithms to assess hormonal status from tissue microarrays in patients with breast cancer. JAMA network open *2*, e197700-e197700.

Sivic, J., and Zisserman, A. (2009). Efficient visual search of videos cast as text retrieval. IEEE transactions on pattern analysis and machine intelligence *31*, 591-606.

Sullivan, D.P., and Lundberg, E. (2018). Seeing More: A Future of Augmented Microscopy. Cell *173*, 546-548.

Swaminathan, K., Campbell, A., Papalazarou, V., Jaber-Hijazi, F., Nixon, C., McGhee, E., Strathdee, D., Sansom, O.J., and Machesky, L.M. (2020). The RAC1 Target NCKAP1 Plays a Crucial Role in the Progression of Braf;Pten-Driven Melanoma in Mice. J Invest Dermatol.

Tanami, H., Imoto, I., Hirasawa, A., Yuki, Y., Sonoda, I., Inoue, J., Yasui, K., Misawa-Furihata, A., Kawakami, Y., and Inazawa, J. (2004). Involvement of overexpressed wild-type BRAF in the growth of malignant melanoma cell lines. Oncogene *23*, 8796.

Travis, W.D., Brambilla, E., Noguchi, M., Nicholson, A.G., Geisinger, K., Yatabe, Y., Ishikawa, Y., Wistuba, I., Flieder, D.B., Franklin, W., *et al.* (2013). Diagnosis of lung adenocarcinoma in resected specimens: implications of the 2011 International Association for the Study of Lung Cancer/American Thoracic Society/European Respiratory Society classification. Arch Pathol Lab Med *137*, 685-705.

van Muijen, G.N., Jansen, K.F., Cornelissen, I.M., Smeets, D.F., Beck, J.L., and Ruiter, D.J. (1991). Establishment and characterization of a human melanoma cell line (MV3) which is highly metastatic in nude mice. International journal of cancer *48*, 85-91.

Viceconte, N., Dheur, M.-S., Majerova, E., Pierreux, C.E., Baurain, J.-F., van Baren, N., and Decottignies, A. (2017). Highly aggressive metastatic melanoma cells unable to maintain telomere length. Cell reports *19*, 2529-2543.

Wang, H., Rivenson, Y., Jin, Y., Wei, Z., Gao, R., Gunaydin, H., Bentolila, L.A., Kural, C., and Ozcan, A. (2019). Deep learning enables cross-modality super-resolution in fluorescence microscopy. Nat Methods *16*, 103-110.

Weigert, M., Schmidt, U., Boothe, T., Müller, A., Dibrov, A., Jain, A., Wilhelm, B., Schmidt, D., Broaddus, C., Culley, S., *et al.* (2018). Content-aware image restoration: pushing the limits of fluorescence microscopy. Nature methods *15*, 1090.

Welf, E.S., Driscoll, M.K., Dean, K.M., Schäfer, C., Chu, J., Davidson, M.W., Lin, M.Z., Danuser, G., and Fiolka, R. (2016). Quantitative multiscale cell imaging in controlled 3D microenvironments. Developmental cell *36*, 462-475.

Williams, E., Moore, J., Li, S.W., Rustici, G., Tarkowska, A., Chessel, A., Leo, S., Antal, B., Ferguson, R.K., Sarkans, U., *et al.* (2017). The Image Data Resource: A Bioimage Data Integration and Publication Platform. Nat Methods *14*, 775-781.

Winter, M., Mankowski, W., Wait, E., Temple, S., and Cohen, A.R. (2016). LEVER: software tools for segmentation, tracking and lineaging of proliferating cells. Bioinformatics *32*, 3530-3531.

Wu, P.-H., Gilkes, D.M., Phillip, J.M., Narkar, A., Cheng, T.W.-T., Marchand, J., Lee, M.-H., Li, R., and Wirtz, D. (2020). Single-cell morphology encodes metastatic potential. Science Advances 6, eaaw6938.

Yin, Z., Sadok, A., Sailem, H., McCarthy, A., Xia, X., Li, F., Garcia, M.A., Evans, L., Barr, A.R., and Perrimon, N. (2013). A screen for morphological complexity identifies regulators of switch-like transitions between discrete cell shapes. Nature cell biology *15*, 860.
Yuan, H., Cai, L., Wang, Z., Hu, X., Zhang, S., and Ji, S. (2018). Computational modeling of cellular structures using conditional deep generative networks. Bioinformatics *35*, 2141-2149.

Zhang, W., Williams, T.A., Bhagwath, A.S., Hiermann, J.S., Peacock, C.D., Watkins, D.N., Ding, P., Park, J.Y., Montgomery, E.A., and Forastiere, A.A. (2020). GEAMP, a novel gastroesophageal junction carcinoma cell line derived from a malignant pleural effusion. Laboratory Investigation *100*, 16-26.

Appendix

All appendix materials are found and hosted at https://www.cell.com/cell-systems/fulltext/S2405-4712(21)00158-7#supplementaryMaterial

Table S1. Panel of melanoma cell types used for this study: cell lines, melanocytes and patient-derived xenograft (PDX), Related to the STAR Methods section. Cells with high metastatic efficiency were derived from patients that exhibited metastases within 22 months, whereas cells with low metastatic efficiency were derived from patients that developed distant metastases within 22 to 50 months (Quintana et al., 2012).

Table S2. Genomics Variants in PDX and two cell lines. PDX-SNVs-Indel and CellLines-SNVs-Indels: Single nucleotide variants (SNVs) and Insertions/Deletions (Indel)s of high-quality variants identified were filtered for common variants in > 1% of any population in GnomAD, Related to the STAR Methods section. The information provided by the columns is as follows: Cell Type, corresponding sample labels in Table S1; Hugo Symbol, the HUGO Gene Nomenclature Committee approved gene name (symbol); Chromosome, the affected chromosome; Start, the mutation start coordinate; Variant_Classification translational effect of variant allele;

Depth, the read depth across this locus in tumor BAM; RefCt, the Read depth supporting the reference allele in tumor BAM; AltCt, read depth supporting the variant allele in tumor BAM; Tumor_MAF, mutational allele frequency (AltCt/Depth) and GT, the genotype encoded as alleles values separated by either of "/" or "|", e.g. The allele values are 0 for the reference allele (what is in the reference sequence), 1 for the ALT. PDX-CNVs and CellLines-CNVs: Copy number variants (CNVs) identified were filtered for genes mutated in > 5% of patients and > 10 patients in TCGA (Hoadley et al., 2018): The information provided by the columns is as follows: Cell Type, corresponding sample labels in Table S1; Hugo_Symbol, the HUGO Gene Nomenclature Committee approved gene name (symbol); Chromosome, the affected chromosome; Start, the mutation start coordinate; End, the mutational end position; Abberation is the type of copy number alteration as gain or loss; CN, the copy number of the gene; Score is calculated by CNV Kit as the sum of the weights of the bins supporting the CNV; Cytoband, the position on the chromosomal cytogentic band.

Table S3. Oncogenic Genomics Variants in PDX and two cell lines in commonly mutated genes (Hodis et al., 2012) , Related to the STAR Methods section. The information provided by the columns is as follows: Annotation, the oncogenic effect, Hugo_Symbol, the HUGO Gene Nomenclature Committee approved gene name (symbol); Variant Type, CNV=Copy

Number Variation, SNV=Single Nucleotide Variant and Indel= Insertion or Deletion; Variant, for SNVs and InDels, this is the HSGS protein change and is the aberration type (gain or loss) which has the predicted oncogenic effect; each following column is the Cell Type corresponding to Table S1 and the genotype or copy of the Cell Type.

Table S4. Non-oncogenic Genomics Variants in PDX and two cell lines in commonly mutated genes (Hodis et al., 2012), Related to the STAR Methods section. The information provided by the columns is as follows: Hugo_Symbol, the HUGO Gene Nomenclature Committee approved gene name (symbol); Variant Type, CNV=Copy Number Variation, SNV=Single Nucleotide Variant and Indel= Insertion or Deletion; Variant, for SNVs and InDels, this is the HSGS protein change and is the aberration type (gain or loss) which has the predicted oncogenic effect; each following column is the Cell Type corresponding to Table S1 and the genotype or copy of the Cell Type.

Video S1. Time lapse sequence of a representative field of view of high metastatic m481 PDX cells, Related to Figure 1.

Video S2. Time lapse sequence of a representative field of view of low metastatic m610 PDX cells, Related to Figure 1.

Video S3. Heterogeneous morphology and local dynamics of patient derived melanoma cells. Shown are time lapse of single cells cropped from the field of view and used as the input for the autoencoder, Related to Figure 1.

Video S4. Reconstruction evolution and convergence during autoencoder training, Related to Figure 1. Raw (top) and reconstructed (bottom) images during the autoencoder training minimizing the binary cross-entropy error between the two.

Video S5. Morphing m498 PDX cell in silico from low to high metastatic efficiency by decoding the latent cell descriptor under gradual shifts in feature #56, Related to Figure 5. The corresponding classifier's score ("ClassifierScore") and value of feature #56 in units of the z-score ("f56") are shown.

Video S6. Morphing m405 PDX cell in silico from high to low metastatic efficiency by decoding the latent cell descriptor under gradual shifts in feature #56, Related to Figure 5. The corresponding classifier's score ("ClassifierScore") and value of feature #56 in units of the z-score ("f56") are shown.

Video S7. Morphing 100 m498 cells by gradually decreasing feature #56 (increasing classifier score), Related to Figure 5.

Video S8. Time lapse of a m610 PDX cell spontaneously switching from the low to the high metastatic efficiency domain (as predicted by the classifier), Related to the Figure 5. Live imaging for 10 minutes.

Video S9. Cell morphing in silico, Related to the STAR Methods section. Following the decoded cell image gradually morphing along an interpolated linear trajectory in the latent space between two cells.

Supplementary figures

Figure S1: Motility, cell shape and latent space dimensionality, Related to Figure 1. (**A**) PDX melanoma on collagen were not migratory. Full field of view in phase contrast (left). Corresponding trajectories from 120 minutes indicate that cells are minimally motile (right). Only cells within the 70μm (dashed lines) were tracked (Methods). (**B**) Cell shape (left: area, right: eccentricity) cannot distinguish high from low metastatic efficiency. Shown distributions were calculated from all cells in call time points. (**C**) Loss and image reconstruction training error as a function of the latent space dimensionality. We selected the 56-dimensional latent vector based on minimizing loss and reconstruction error. Left: autoencoder loss (binary cross-entropy) after training, right: mean square error for image reconstruction after training.

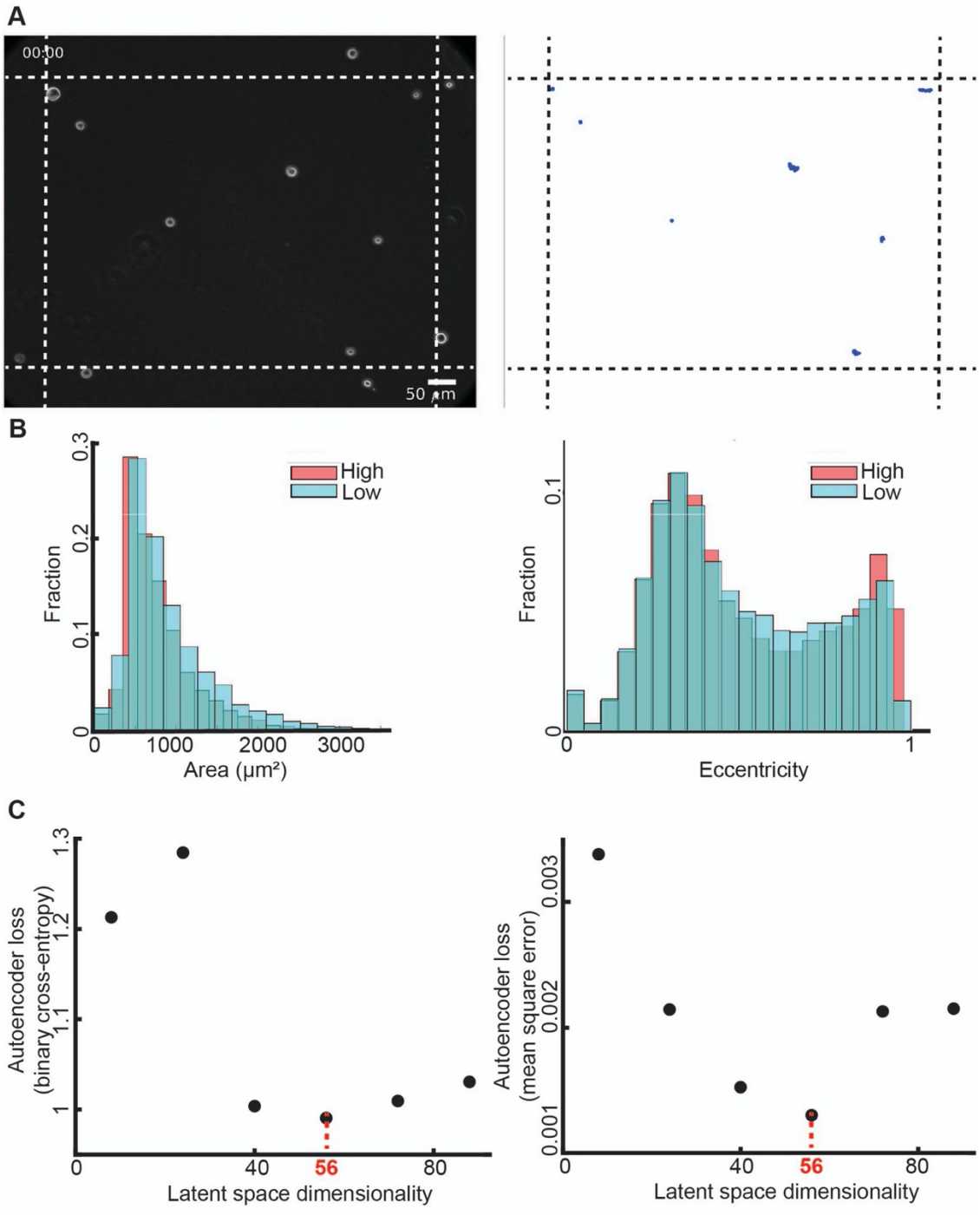
A
00:00
50 μm
B
High
Low
Fraction
0
0.1
0.2
0.3
0
1000
2000
3000
Area (μm²)
High
Low
Fraction
0
0.1
0
1
Eccentricity
C
Autoencoder loss
(binary cross-entropy)
1
1.1
1.2
1.3
0
40
56
80
Latent space dimensionality
Autoencoder loss
(mean square error)
0.001
0.002
0.003
0
40
56
80
Latent space dimensionality

Figure S2: Validation of adversarial autoencoder latent space as a quantitative measure of cell appearance, Related to the STAR Methods section. (**A**) Pipeline to test that increasing shifts in the latent vector of a cell relate to a monotonically increasing shift in cell appearances. (**B**) Increasing perturbation of a particular cell's latent space vector by Gaussian noise yields an increased deviation of the reconstructed cell image from the original image (image indicated at x = 0). For each noise level, except level 0, four representative reconstructed images are shown. Lines indicate the reconstruction error for 92 randomly selected cells from different cell types and different biological replicates. (**C**) Cell "morphing". Latent space interpolation shows that a gradual linear transition in latent space yields gradual transition in image space. By "gradual linear transition in latent space" we refer to constant size shifts in feature space for each shift. The trajectory goes from top-left (red) to bottom-right (green). (**D**) Differences of images in panel C and to the start- (red) and endpoint (green) images. (**E**) Cells are more self-similar over time than two neighboring cells at the same time. Two-dimensional histogram of the Euclidean distance between the latent space descriptors of a cell at time 0 and time 100 (x-axis) versus the distance of the same cell to its closest (in terms of distance in the physical space) neighboring cell in the same field of view, also at time 0 (y-axis).

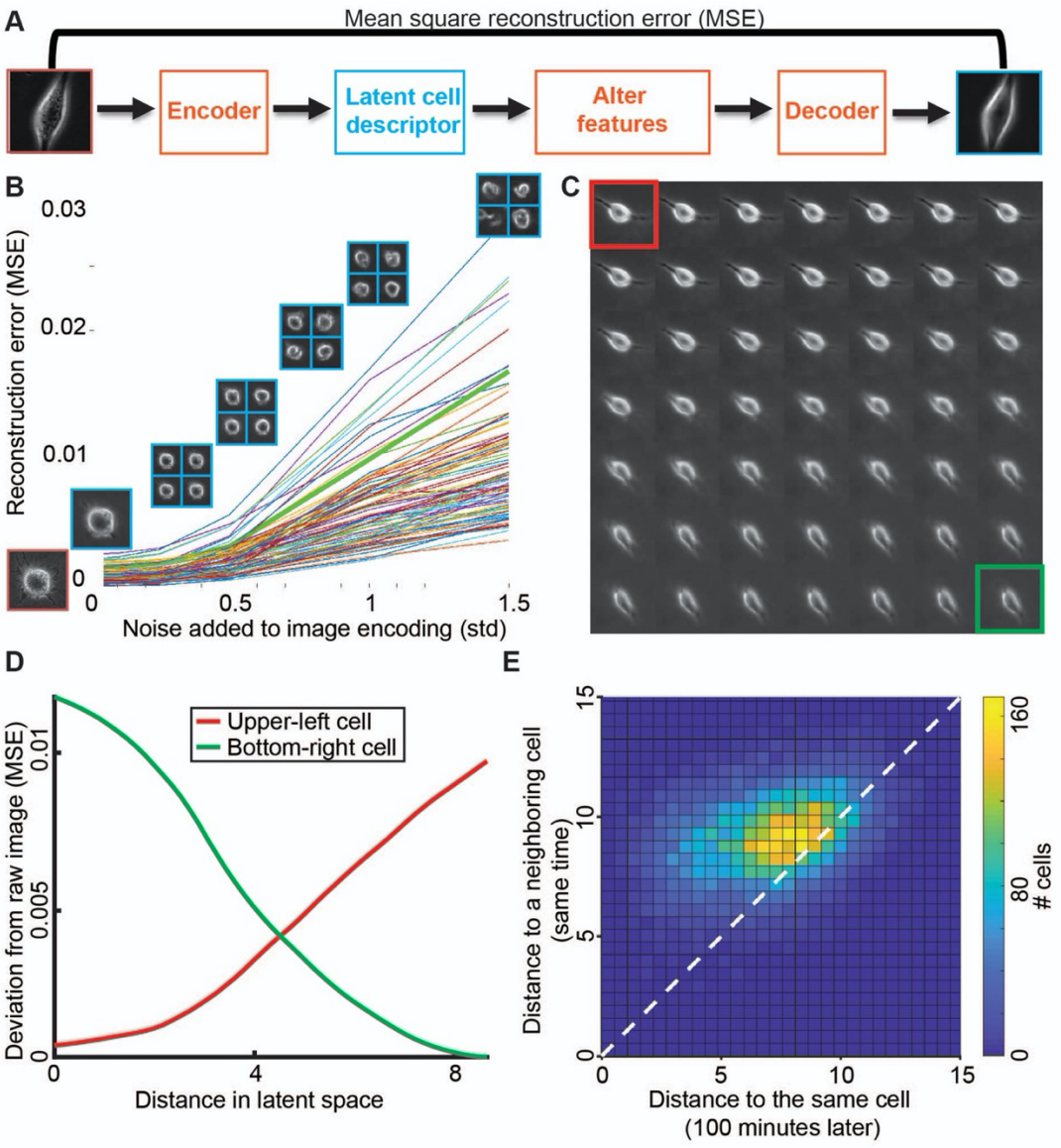
A
Mean square reconstruction error (MSE)
Encoder
Latent cell descriptor
Alter features
Decoder
B
Reconstruction error (MSE)
0.03
0.02
0.01
0
0
0.5
1
1.5
Noise added to image encoding (std)
C
D
Upper-left cell
Bottom-right cell
Deviation from raw image (MSE)
0.01
0.005
0
0
4
8
Distance in latent space
E
Distance to a neighboring cell (same time)
15
10
5
0
0
5
10
15
Distance to the same cell (100 minutes later)
160
80
0
cells

Figure S3: Determining batch effects (day-to-day variability), Related to Figure 2. Cells from four melanoma PDXs (m481, m498, m610, m634) were imaged in one batch, and this experiment was repeated on 6 different days. (**A**) Assessing the distance among different days for the same PDX versus the distance among the different PDXs imaged on the same day. (**B**) Intra-PDX/inter-day distance (x-axis) versus intra-day/inter-PDX distance (y-axis). Each dot represents the distance between the mean time-averaged latent cell descriptors averaged over all cells, arbitrary units. (**C**) tSNE projection of latent space cell descriptors of different PDXs on the same day (left) and of one PDX imaged on different days (right). (**D**) PCA projection of latent space descriptors of different PDXs on the same day (left) and of one PDX imaged on different days (right).

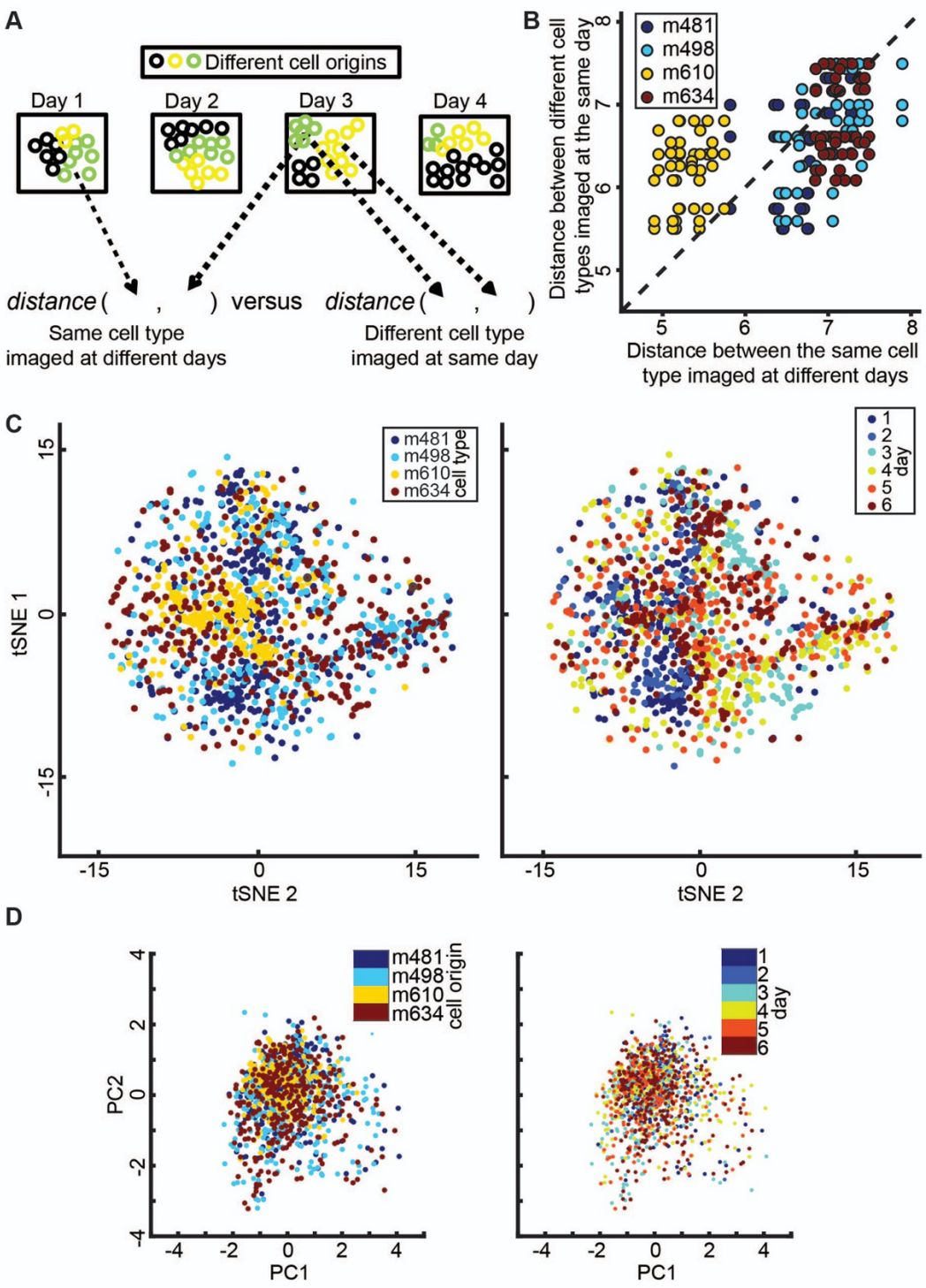
A
Different cell origins
Day 1
Day 2
Day 3
Day 4
distance (,) versus distance (,)
Same cell type imaged at different days
Different cell type imaged at same day
B
m481
m498
m610
m634
Distance between different cell types imaged at the same day
Distance between the same cell type imaged at different days
C
m481
m498
m610
m634
cell type
1
2
3
4
5
6
day
tSNE 1
tSNE 2
tSNE 2
D
m481
m498
m610
m634
cell origin
1
2
3
4
5
6
day
PC2
PC1
PC1

Figure S4: Discrimination results using classifiers that were blind to the cell type and day of imaging, Related to Figure 2. (**A**) Blinding the cell type and the day of imaging. Multiple rounds of training and testing were performed. In each round, all cells of one cell type imaged in one day were used as the test dataset. The training set consisted of the remainder of the data, excluding the cell type at test and data from the same day of imaging. Thus, the trained model was completely blind to the test set. The model classified each cell in the test set, the overall mean classification accuracy for a specific cell type and imaging day was reported. The classifier's score of every cell was recorded and accumulated for all cell type + imaging day pair for Receiver Operating Characteristic analysis. Besides excluding batch-effects by blinding the classifier to the day of imaging, this provided us with an increased number of observations (cell type, day) at the cost of a reduced number of cells per observation. (**B-C**) Discriminating melanoma cell lines from melanocyte lines. (**B**) Receiver Operating Characteristic (ROC) curve. AUC = 0.635. (**C**) Accuracy in predicting the label 'cell lines' for a single cell as opposed to the label 'melanocytes'. Each data point indicates the outcome (fraction of cells classified as 'cell line') of testing the cells of one melanoma cell line or melanocyte line on a particular day. N = 24: 18 cell lines, 6 melanocyte lines. 19/24 successfully predicted observations. Wilcoxon rank-sum test $p = 0.026$. Binomial statistical test $p < 0.003$, see Methods for justification of the statistical tests. (**D-E**) Discriminating melanoma cell lines from clonally expanded cell lines. (**D**) Receiver Operating Characteristic (ROC) curve. AUC = 0.65. (**E**) Accuracy in predicting the label 'cell lines' for a single cell as opposed to the label 'clonal'. Each data point indicates the outcome of testing the cells of one melanoma cell line or clonal expansion line on a particular day. N = 29: 18 cell lines, 11 clonal expanded cells. 22/29 successfully predicted observations. Wilcoxon rank-sum test $p = 0.0032$. Binomial statistical test $p < 0.0041$. (**F-G**) Discriminating melanoma cell lines versus PDXs. (**F**) Receiver Operating Characteristic (ROC) curve. AUC = 0.686. (**G**) Accuracy in predicting the label 'cell lines' for a single cell as opposed to the label 'PDXs'. Each data point indicates the outcome of testing the cells of one melanoma cell line or PDX on a particular day. N = 75: 18 cell lines, 75 PDXs. 63/75 successful predicted observations. Wilcoxon rank-sum test $p < 0.0001$. Binomial statistical test $p < 0.0001$. (**H**) Pairwise discrimination of cell types. Discriminating two cell types from one another. Each data point indicates the AUC value for predicting the cell type label for single cells. Multiple rounds of training and testing were performed for each pairwise classification. In each round, data from one cell type imaged in one day was used as the test dataset, while the training set consisted of the remainder of the data, excluding data from the same day of imaging. Note that here the classifiers were blind to the day of imaging, but not to the cell type at test. The green dashed line is the mean AUC = 0.66. The blue dashed line indicates the AUC level of a random classifier. p-value < 0.0001 (Wilcoxon sign-rank test) rejecting the null hypothesis that pairs of different cell types cannot be discriminated.

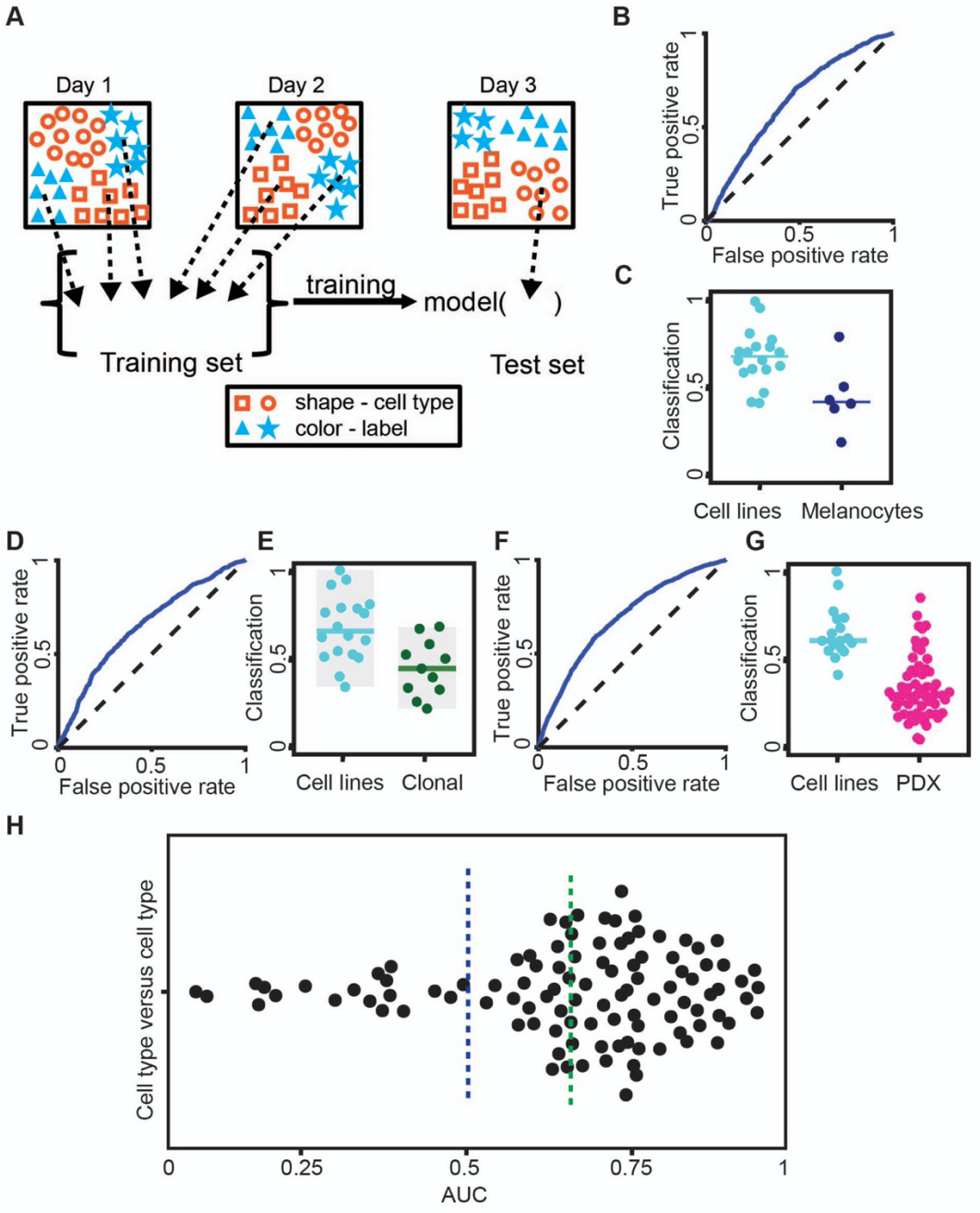
A
Day 1
Day 2
Day 3
training
model( )
Training set
Test set
shape - cell type
color - label
B
True positive rate
False positive rate
C
Classification
Cell lines
Melanocytes
D
True positive rate
False positive rate
E
Classification
Cell lines
Clonal
F
True positive rate
False positive rate
G
Classification
Cell lines
PDX
H
Cell type versus cell type
AUC

Figure S5: Discriminating cell lines from PDXs using cell shape and temporal information, Related to Figure 2 and to the STAR Methods section. (**A-B**) Single cell segmentation in phase-contrast images by LEVER. (**A**) Examples of successful segmentation. The region outside the segmentation mask is colored black. (**B**) Examples of failed segmentations. (**C**) Three scenarios of incorporating temporal information in a cell descriptor applied to either cell shape-based features or latent space cell descriptors. (**D**) Accuracy in predicting the label 'cell lines' for a single cell as opposed to the label 'PDXs'. Each data point indicates the outcome of testing the cells of one melanoma cell line or PDX on a particular day (Fig. S4A). Classifiers derived from cell shape-based features could not discriminate between the two labels, regardless of the mode of incorporating temporal information. In contrast, the latent space cell descriptors slightly improved with explicit consideration of temporal information and all classifier modes significantly outperformed shape-based classifiers (*** - p-value < 0.0001, nonparametric Wilcoxon sign-rank test. N = 65 experiments of one cell type imaged in one day. The green line is the median. The dashed red horizontal line represents the random model.). (**E**) The latent cell descriptor outperforms shape features. Matrix visualization of the comparison of the different encodings. Fold (left), p-value (middle), log p-value (right, -3 corresponds to the p-value of 0.05). The average latent cell descriptor classification accuracy surpasses other cell encoding schemes. Stat - static, Avg. - average, BOW - bag of words. (**F**) Mean squared displacement analysis (MSD) analysis of single cell trajectories averaged over each cell type did not show discrimination between cell lines and PDXs. Maximal time lag of 60 frames (=minutes).

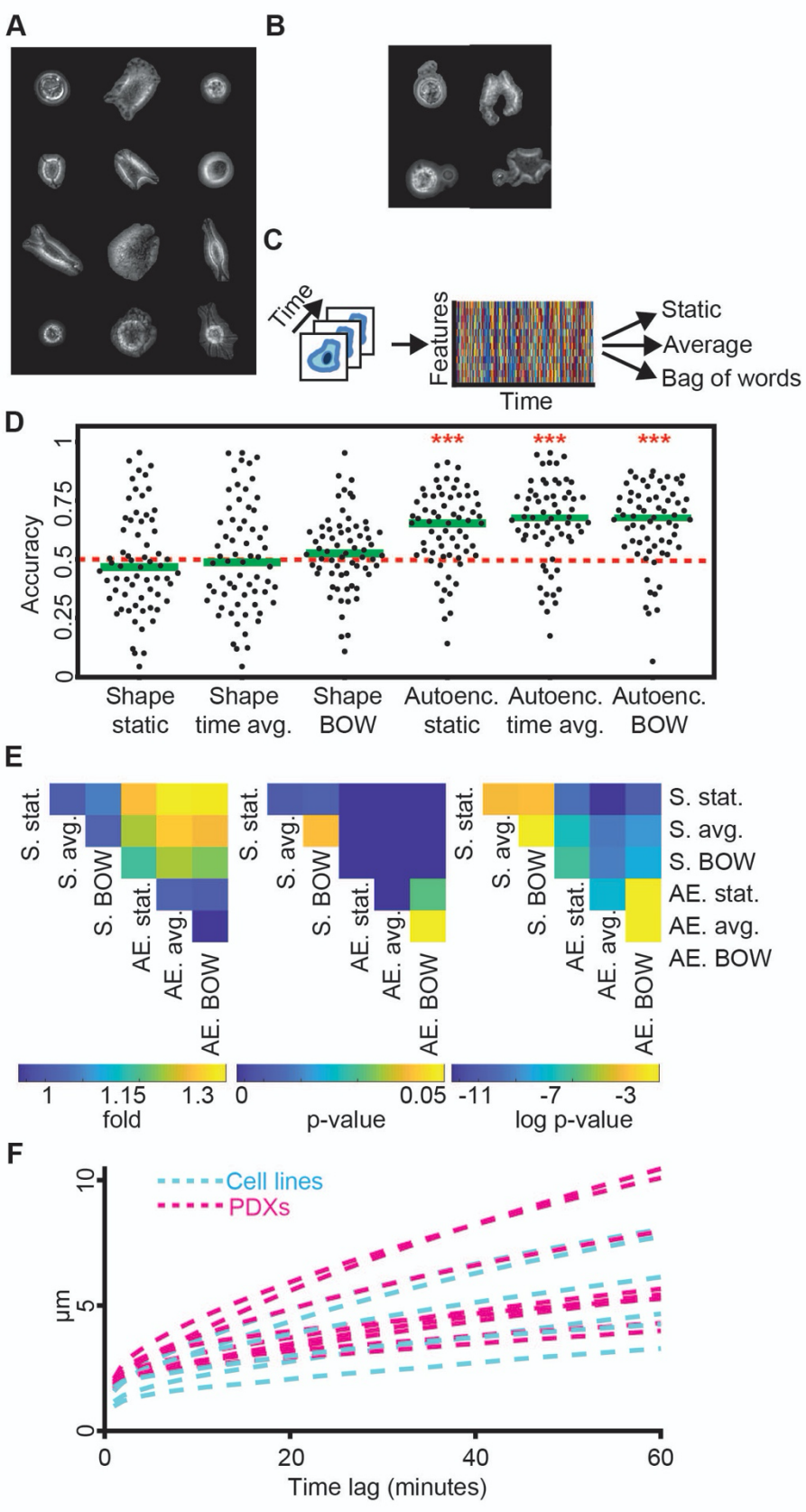
A
B
C
Time
Features
Time
Static
Average
Bag of words
D
Accuracy
0
0.25
0.5
0.75
1
***
***
***
Shape static
Shape time avg.
Shape BOW
Autoenc. static
Autoenc. time avg.
Autoenc. BOW
E
S. stat.
S. avg.
S. BOW
AE. stat.
AE. avg.
AE. BOW
1
1.15
1.3
fold
0
0.05
p-value
-11
-7
-3
log p-value
F
Cell lines
PDXs
µm
0
5
10
0
20
40
60
Time lag (minutes)

Figure S6: Discriminating high versus low metastatic efficient PDXs using cell shape and temporal information, Related to Figure 3. (**A**) Accuracy of classifiers derived from shape based features and from latent space cell descriptors in predicting the label 'low efficiency' for a single cell. The classifiers include various modes of incorporating temporal information (Fig. S5). The 0.5 horizontal line reference the accuracy of a random classifier. Shape-based classifiers could not discriminate between PDXs with high and low metastatic efficiency. Classifiers derived from latent space cell descriptors performed significantly better than random ** - p-value < 0.01 (0.0053 for Autoenc. static, 0.0056 for Autoenc. time avg.), nonparametric Wilcoxon sign-rank test. N = 40 experiments of PDX imaged in one day. Green lines indicate medians of accuracy distributions. (**B**) Mean squared displacement (MSD) analysis of single trajectories averaged over each PDX could not distinguish between high and low metastatic efficiency. Max time lag of 60 frames (=minutes). (**C**) MSD analysis for a longer duration of 8 hours could not distinguish (p-value not significant in 100, 200, 300 and 480 minutes) between m498 (low metastatic efficiency, N = 30 cells) versus m481 (high metastatic efficiency, N = 30 cells).

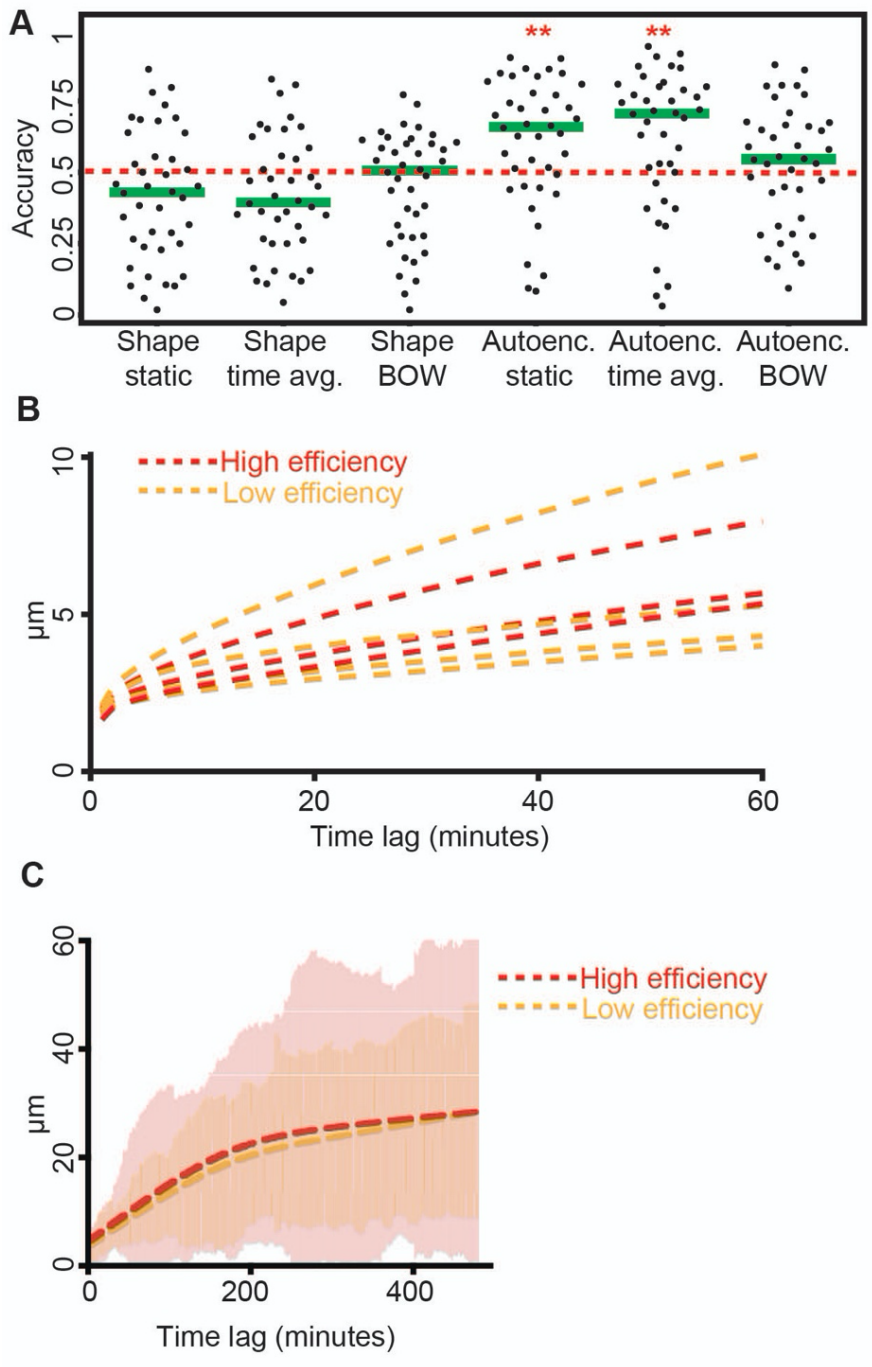
A
Accuracy
0
0.25
0.5
0.75
1
**
**
Shape static
Shape time avg.
Shape BOW
Autoenc. static
Autoenc. time avg.
Autoenc. BOW
B
High efficiency
Low efficiency
µm
0
5
10
0
20
40
60
Time lag (minutes)
C
µm
0
20
40
60
0
200
400
Time lag (minutes)
High efficiency
Low efficiency

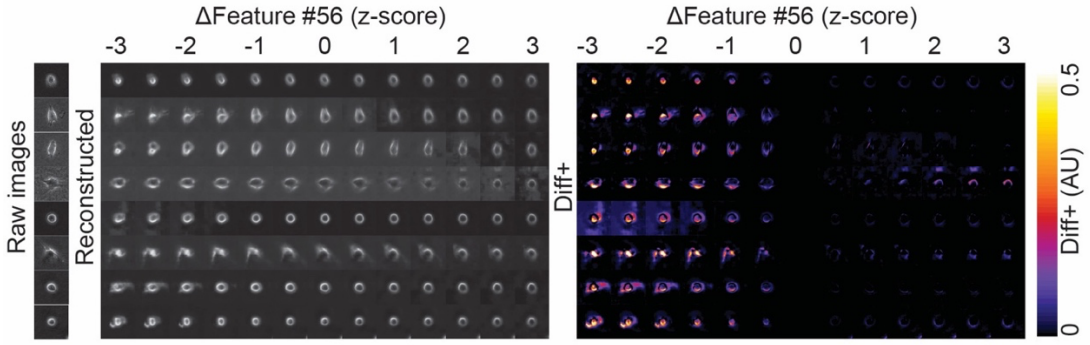

Figure S7: Panel of in silico cells generated by decoding a representative PDX cells' latent space cell descriptor under gradual shifts in feature #56, Related to Figure 5. Raw images (left), reconstructed images (middle), the positive values of the intensity differences between consecutive virtual cells (right).

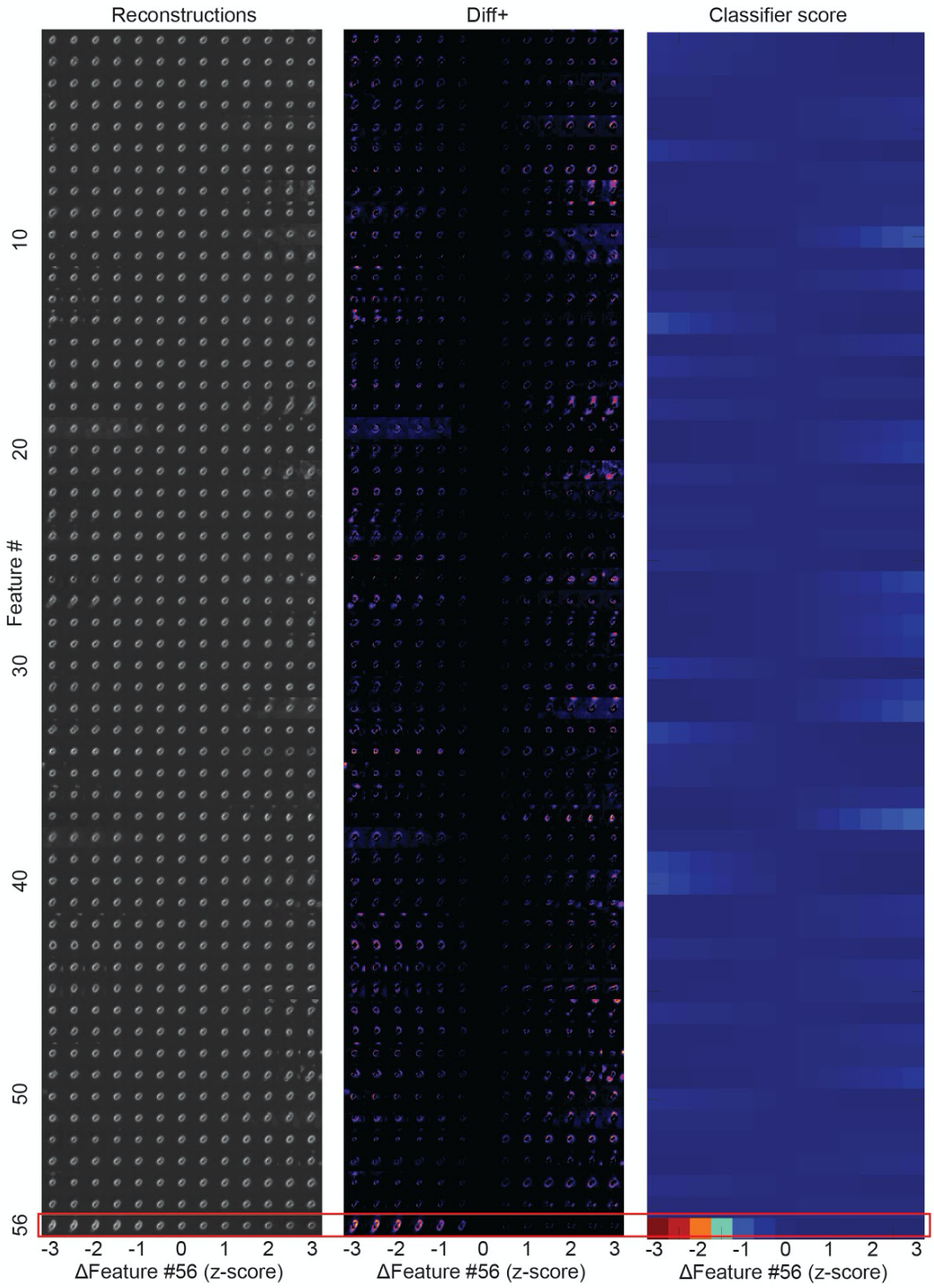

Figure S8: Visualization of in silico cells by altering each feature highlight the unique properties of feature #56, Related to Figure 5. Reconstructed images (left), the positive values of the intensity differences between cells with different values in feature #56 (middle), the classifiers' predicted scores (right).

Figure S9: Generalized high-dimensional generative modeling for linear classifiers applied for cell lines versus PDXs discrimination. N = 6 melanoma cell lines, 9 PDXs, Related to Figure 5. (**A-B**) Multiple features are classification-driving for discriminating cell lines from PDXs. (**A**) Correlation values between all 56 features (y-axis) and the classifier scores for different cell types (x-axis). The correlation was calculated based on all cells from each cell type. (**B**) Normalized correlation values (Z-scores). (**C**) LDA coefficients trained to discriminate cell lines from PDXs (y-axis) for different cell types (x-axis). (**D**) LDA coefficients are correlated with feature-to-classifier-score-correlation. Each dot represents one features' correlation with the classifier (x-axis) and its corresponding LDA coefficient (y-axis). (**E**) Panel of in silico cells generated by decoding a representative PDX cells' latent space cell descriptor under gradual shifts along the 56-dimensional latent space weighted according to the LDA coefficients of cell lines versus PDX classification. Left-to-right describe the transition from PDX to cell line. These are the same cells used in Fig. S7. The red arrow highlights a cell where traversal of the feature space outside the natural range of data variation artificially fractionates the cell image.

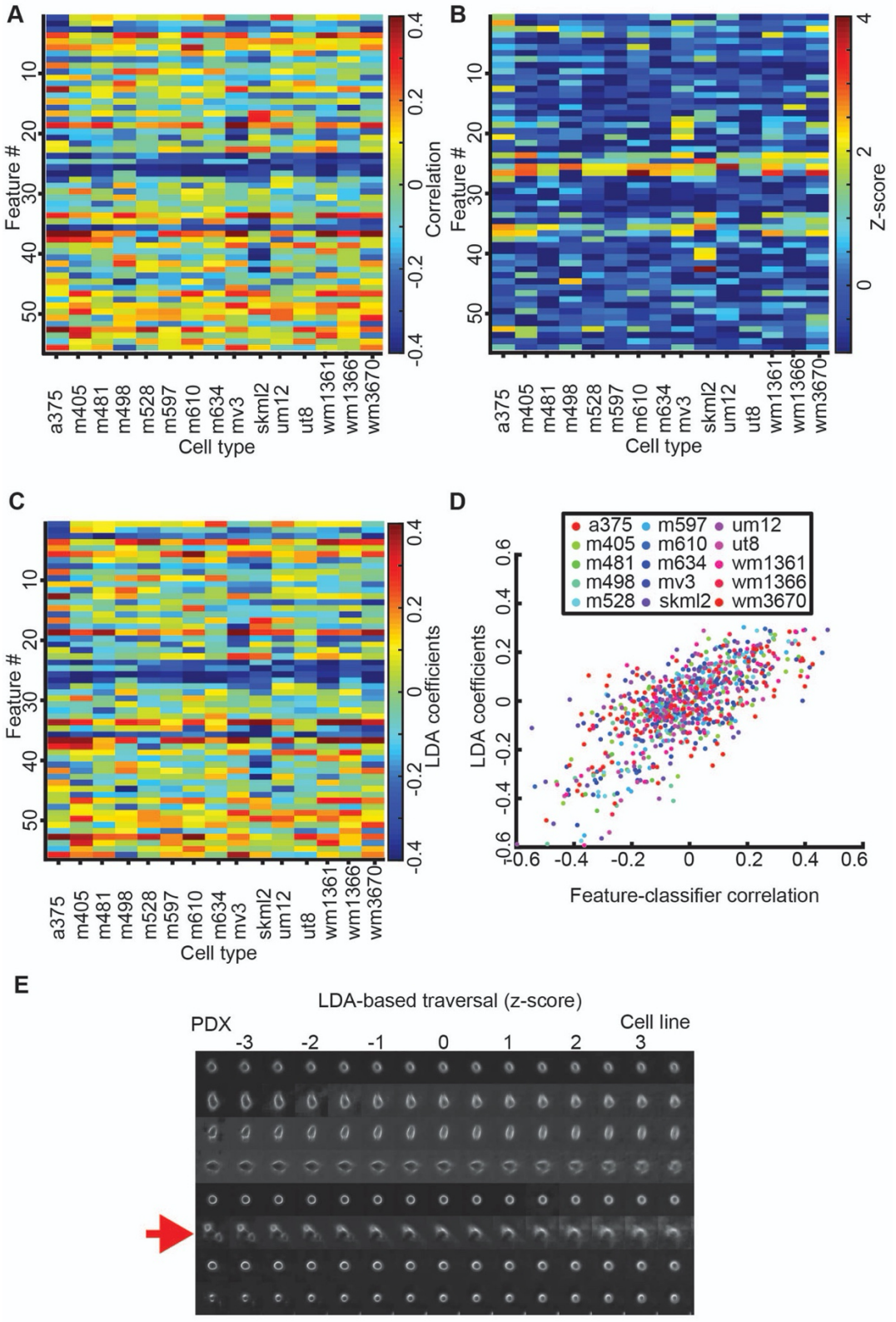
A
Feature #
Correlation
Cell type
a375
m405
m481
m498
m528
m597
m610
m634
mv3
skml2
um12
ut8
wm1361
wm1366
wm3670
B
Z-score
C
LDA coefficients
D
LDA coefficients
Feature-classifier correlation
E
LDA-based traversal (z-score)
PDX
Cell line

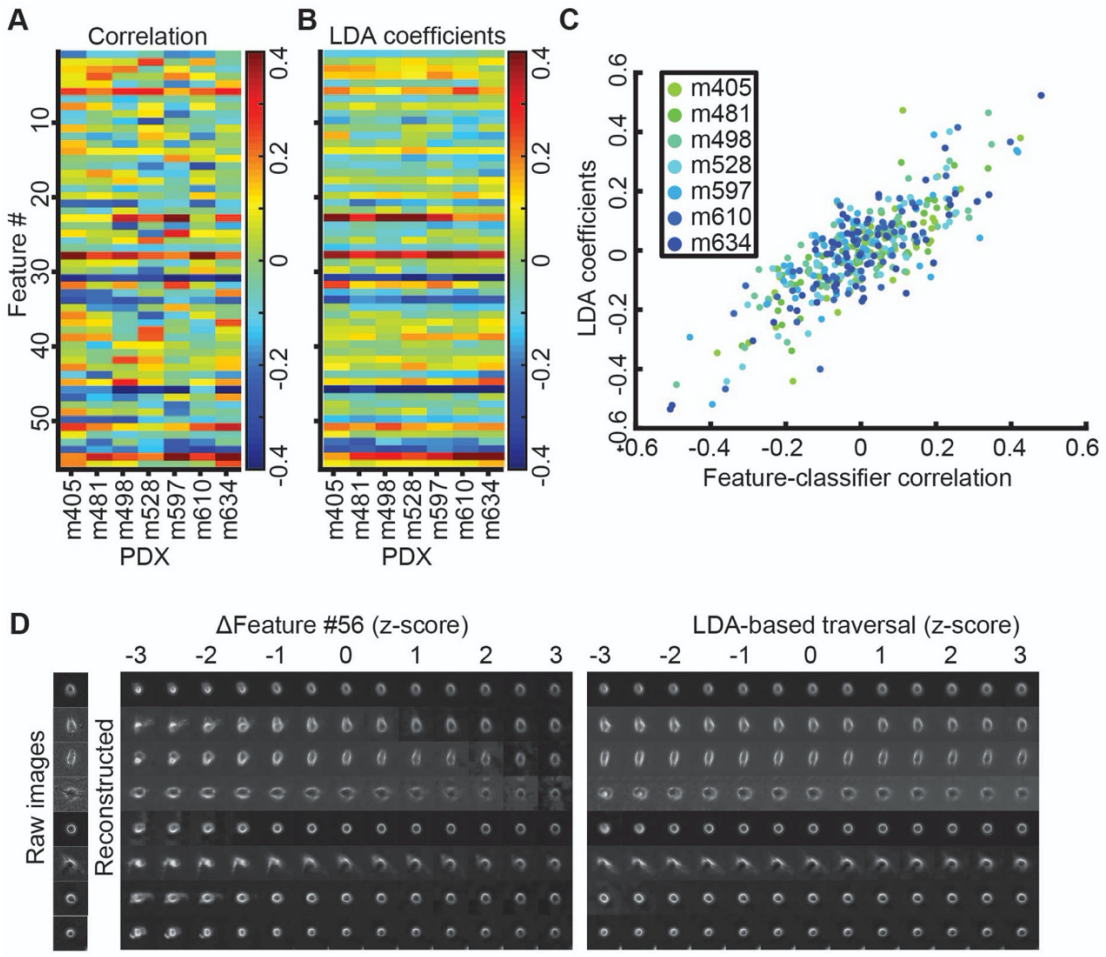

Figure S10: High-dimensional generative modeling for linear classifiers applied for high versus low metastasis PDXs discrimination, Related to Figure 5. (**A**) Multiple features are classification-driving for discriminating high from low metastatic PDXs using latent cell descriptors derived from a second adversarial autoencoder network that was independently trained on the same dataset. (**B**) LDA coefficients trained to discriminate high from low metastatic PDXs (y-axis) for different PDXs (x-axis). (**C**) LDA coefficients are correlated with feature-to-classifier-score-correlation. Each dot represents one features' correlation with the classifier (x-axis) and its corresponding LDA coefficient (y-axis). (**D**) Panel of in silico cells generated by decoding a representative PDX cells' latent space cell descriptor under gradual shifts along feature #56 of the first network (left) and the 56-dimensional latent space weighted according to the LDA coefficients of the second network (right). Left-to-right describe the transition from high to low metastatic efficiency. These are the same cells used in Fig. S7.

Figure S11: Genomic markers could not distinguish between high and low metastatic efficiency. Distance measures between pairs of different cell types were compared between image-based (classifier scores) and genomic-mutational based information, Related to Figure 6. (**A-D**) Distance matrices between pairs of cell-types. Red sub-matrices indicate the distances between PDXs (and the A375 cell line) classified as highly metastatic. Orange sub-matrices indicate the distances between PDXs (and the MV3 cell line) classified as highly metastatic. (**A**) Distance matric derived from image based classifier scores. Individual distances were computed based on the Jensen-Shannon divergence of the classifier score distributions for single cells in each of the compared cell types. The sub-matrices of cell types with similar levels of metastatic efficiency show low distances compared to matrix bins comparing cell types with differing metastatic efficiency. (**B-D**) Distance matrices derived from the genomic profiles of cell types cannot distinguish between high and low metastatic efficiency. (**B**) Distances calculated based on the Jaccard index of the mutational state of the oncogenic mutations in the 20 top mutated genes in melanoma. (**C**) Distances calculated based on the Jaccard index of the non-oncogenic mutations from those same genes. (**D**) Distances calculated by application of the alignment-free method MASH to the sequences from the entire 1400 gene panel. (**E-G**) Distances derived from image-based versus genomics-based cell-type to cell-type distinction are not correlated. Each datum holds the matched pair classifier- and genomic- distances between two cell types. E, F, and G correspond to the matrices in B, C and D, each correlating with the distance matrix in A. No correlation was found to be statistically significant.

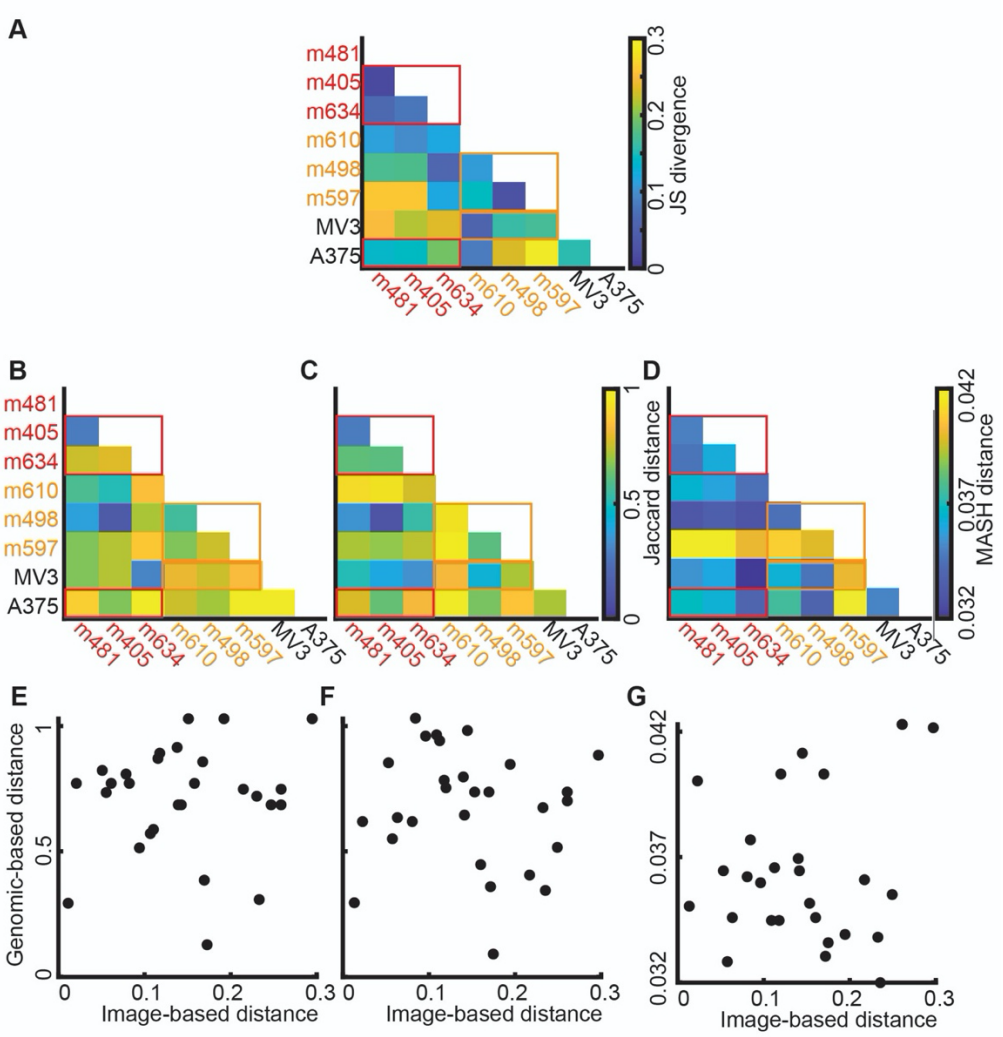
A
m481
m405
m634
m610
m498
m597
MV3
A375
JS divergence
0
0.1
0.2
0.3
B
C
D
Jaccard distance
0
0.5
1
MASH distance
0.032
0.037
0.042
E
F
G
Genomic-based distance
Image-based distance
0
0.1
0.2
0.3
0.5
1
0.032
0.037
0.042

Chapter 3

Dissecting the connection between metastatic phenotypes and Telomerase promoter mutations

Andres J. Nevarez[1,3], Anusorn Mudla[1], Yishaia Zabary[2], and Nan Hao[1*]

[1]Section of Molecular Biology, Division of Biological Sciences, University of California SanDiego, 9500 Gilman Drive, La Jolla, CA 92093, USA

[2]Department of Software and Information Systems Engineering, Ben-Gurion University of the Negev, Beer-Sheva, 84105, Israel

[3]@technicolordres

[*]Corresponding author: N. Hao

Keywords: telomerase promoter mutations, metastasis, cellular morphology, quantitative imaging, light microscopy, machine learning, deep learning

Abstract

While we have made enormous progress regarding our understanding of Melanoma, it is still a leading cause of skin cancer deaths worldwide. The cause of this high lethality is primarily due to the metastatic stage of the disease. Sequencing patients' metastatic tumors have revealed two

monoallelic Telomerase promoter mutations (TPMs), C228T and C250T. TPMs occur early in melanoma development but become enriched in metastatic tumor sites; this clonal evolution suggests a functional role of TPMs in metastatic progression. C228T occurs at a higher frequency than C250T; however, in Melanoma, C250T occurs nearly equal to C228T compared to all other cancers. To dissect the effect of TPMs on in vitro metastatic phenotypes without the plethora of background mutations found in Melanoma, we engineered isogenic clonal cell lines with monoallelic TPMs and expression reporters under both alleles' endogenous promoter of Telomerase. Single-allele single-cell imaging reveals that, contrary to consensus, C228T and C250T mutations are not equal. C250T displays increased allele expression heterogeneity, healing rate, spatiotemporal collection cell dynamics, and morphological differences over the C228T TPM and the WT cell lines. This work quantitatively identifies sources of functional metastatic advantages of TPMs, which may positively compound in vivo fitness for increased metastatic dissemination.

Introduction

Increased Telomerase expression is a hallmark of cancer, reactivating in most cancer diagnoses to enable replicative immortality (Kim, Piatyszek et al. 1994, Hanahan and Weinberg 2011). Telomerase promoter mutations

(TPMs), initially found in Melanoma, are found in over 90% of aggressive cancers (Huang, Bai et al. 2003, Horn, Figl et al. 2013, Bell, Rube et al. 2015). Melanoma is known for its high mortality rate due to its ability to metastasize and intrinsic drug resistance (Eggermont, Spatz et al. 2014). Metastatic and therapy-resistant cells share many common properties; metastasis and, therefore, therapy resistance is the last frontier of cancer treatment (Fares, Fares et al. 2020). Since then, TPMs correlate with poor prognosis and an increased rate of metastasis in Melanoma patients (Hugdahl, Kalvenes et al. 2018). The majority of Melanoma related deaths are due to the metastatic stage of the disease; metastasis occurs when cells from the primary tumor leave the local environment and colonize a distant organ (Bogenrieder and Herlyn 2003, Gupta and Massagué 2006), Chiang and Massagué (2008), (Hanahan and Weinberg 2011, Reddy, Lim et al. 2012, Dillekås, Demicheli et al. 2016).

There are multiple variants of TPMs, but the most common are located at positions -124 (C228T) and -146 (C250T) base pairs upstream of the translational start site (Heidenreich, Rachakonda et al. 2014, Chiba, Lorbeer et al. 2017). The C228T and C250T mutations are mutually exclusive and almost always are heterozygous in patients (Griewank, Murali et al. 2014). Both C228T and C250T create an identical 11 base pair sequence

"CCCGGAAGGGG", making a new de novo ETS binding motif for ETS transcription factors to activate Telomerase expression. C228T occurs at a higher frequency than C250T; however, in Melanoma, C250T occurs at a near equal frequency to C228T compared to all other cancers (Huang, Hodis et al. 2013, Hafezi and Perez Bercoff 2020). Because C228T and C250T are the most common TPMs, it suggests that these TPMs are selected early in melanoma development (Heidenreich, Rachakonda et al. 2014, Shain, Yeh et al. 2015, Torrecilla, Sia et al. 2017). Despite being an activating mutation, TPMs do not increase Telomere length despite increasing Telomerase expression in Melanoma to varying magnitudes (Ceccarelli, Barthel et al. 2016, Nagore, Heidenreich et al. 2016, Hayward, Wilmott et al. 2017) especially in aggressive metastatic tumors (Viceconte, Dheur et al. 2017).

Meta-analysis of metastatic potential and penetrance in tumors harboring TPMs

A clonal composition change in cancer progression from primary to metastatic disease enriches cells harboring the TPMs (Griewank, Murali et al. 2014). This clonal evolution suggests a functional advantage for metastatic potential and penetrance correlating to TPM status. To quantify metastatic potential and penetrance of TPMs in vivo, we turned to the large-scale pan-cancer study MetMap (Ershov et al., 2021). MetMap does not include the

TPM statuses of their cell lines; however, we mined cell databases and primary literature to identify the TPM statuses of cell lines. While the N of our C228T and C250T samples used in the subsequent analysis is nowhere near the 500 cell lines used in the MetMap study. We are limited because TPM status is identified using whole-genome or Sanger sequencing. Often, clinics and research groups will use exome sequencing for cancer mutation profiling; however, this is changing. We could not stratify C250T and C228T by cancer type due to a lack of TPM information for many of the 500 cell lines used in the MetMap study. We found that C250T had higher penetrance and potential than the C228T pan-cancer and in all organs (**Fig 3.1A and G**). Breaking down metastatic potential and penetrance by each organ for TPMs shows that C250T has significantly higher penetrance in the Lung, Liver, and Brain (**Fig 3.1B-D**). At the same time, the Kidney and Bone show no difference.

In contrast, C250T has significantly higher potential in the Lung and Liver than in the Kidney, Bone, and Brain, which show no difference. We found that TPMs do not correlate with aneuploidy, mutational burden, or replication rate of the samples used. Using the MetMap database, we could not interrogate metastatic potential and penetrance in Melanoma specifically. However, it should be noted that the difference in the

metastatic potential of TPMs in Melanoma was corroborated by a recent study using interpretable, deeply learned models to identify high and low-efficiency metastatic melanoma single-cell properties (Zaritsky et al., 2021). The interpretable deep learned model predicted A375, which harbors the C250T mutation (Heidenreich et al., 2014), to have higher metastatic potential This was confirmed in the metastatic mouse model established by the landmark study of metastatic Melanoma (Quintana et al., 2012). While it is the consensus that TPMs genetically and functionally are identical, these results suggest that TPMs are not similar in vivo. Furthermore, since C250T occurs in higher frequency in Melanoma, a cancer type known for its aggressive metastatic stage (Tracey and Vij 2019), C250T may impact metastatic phenotypes. This meta-analysis shows pan-cancer tumors harboring the C250T TPM have higher metastatic potential and penetrance. However, we are not extending this to claim C250T is solely causative in increasing metastatic potential and penetrance over C228T.

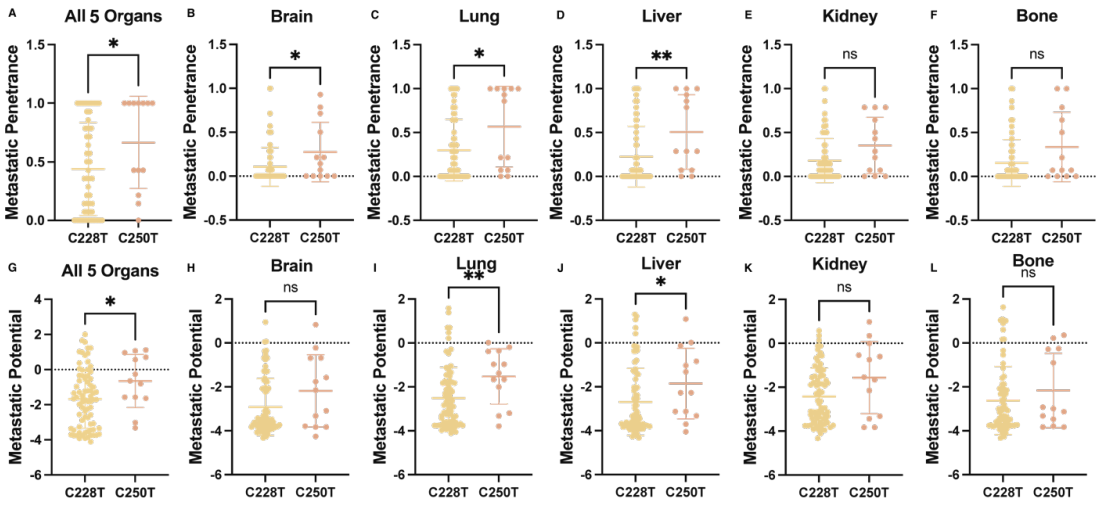

Figure 3.1 Metanalysis of mined information from MetMap database for quantified metastatic potential and penetrance of cell lines harboring Telomerase Promoter Mutations stratified by C228T and C250T. C228T n = 76, and C250T n = 13. **(A)** Metastatic Penetrance comparison of C228T and C250T aggregated by all organs used in the MetMap database, p =0.0330. **(B, C, D, E, F)** Metastatic Penetrance comparison of C228T and C250T separated by organ Brain p = 0.0240, Lung p = 0.0326, Liver p =0.0055, Kidney p = 0.0615, and Bone p = 0.0766. **(G)** Metastatic Potential comparison of C228T and C250T aggregated by all organs used in the MetMap database, p = 0.0326. **(H, I, J, K, L)** Metastatic Potential comparison of C228T and C250T separated by organ Brain p = 0.1555, Lung p = 0.0099, Liver p = 0.0347, Kidney p = 0.0819, and Bone p = 0.3706. All p values from Mann-Whitney test.

Isogenic cells harboring TPMs increase mean expression and stochastic expression variance

To dissect the effect of each TPM on metastatic phenotypes in vitro, we chose 293T cells due to minimal mutational burden and unlimited replicative ability other than through the Telomerase pathway. To this end, 293T $TERT^{WT/WT}$, $TERT^{C228T/WT}$, and $TERT^{C250T/WT}$ single-cell clones were engineered with spectrally distinct fluorescent expression reporters on each allele under the endogenous promoter and at the endogenous loci **(Fig 3.2A and B)**. We first confirmed the mean expression of the TPM allele increased

~1.4x over the corresponding WT allele **(Fig 3.2C)**, as other groups have shown before (Huang, Bai et al. 2003, Horn, Figl et al. 2013). However, there is a statistical increase in the mean expression of the C250T over the C228T TPM allele, which has not been seen using endogenous reporter systems before. There were significant differences between the three populations regarding the WT allele. C250T, and to a minor degree C228T, had increased mean expression over the corresponding WT allele **(Fig 3.2D)**. Since we have an allelic resolution of Telomerase, we quantified the impact of TPMs on the gene expression variance seen in the scatter plot **(Fig 3.2E)** of cells using the Fano Factor (Sanchez, Garcia et al. 2011). C250T had the highest expression variance, while C228T showed a moderate increase in variance, and the corresponding WT allele had the slightest variance in the Fano Factors **(Fig 3.2F)**. When looking at only the WT allele, we see the double WT cell line has an increased expression variance over C228T, while C250T has the highest variance about the Fano Factors **(Fig 3.2G)**. This is not seen in other studies, as all have focused solely on the mutated allele. We posit that this may be due to the three-dimensional architecture of the nucleus allowing for alleles to be near each other (Quinodoz, Ollikainen et al. 2018) and possibly sharing transcriptional machinery.

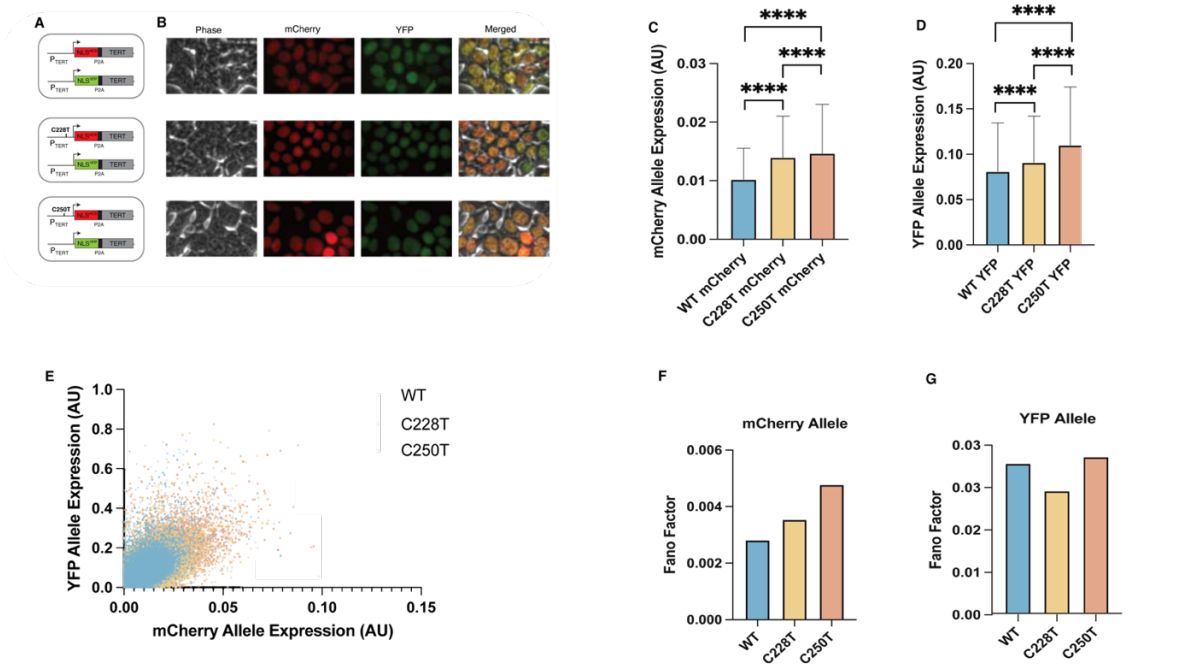

Figure 3.2 TPMs increase mutant allele expression and clonal variance. (A) Schematic of the engineered genomic structure of the cell lines. **(B)** False-colored image montage of representative cells for Telomerase promoter mutants, C228T, C250T, and WT cell lines. Telomerase gene expression separated by allele for n = 67,000 cells. **(C)** The bar graph shows the difference in mean mCherry Allele expression of the mutant allele containing the control WT allele and the promoter mutation C228T and C250T, respectively. WT displayed significantly lower expression than C228T p <0.0001 and C250T <0.0001. While C228T showed significantly lower expression than C250T <0.0001 (unpaired t-tests). **(D)** The bar graph shows the difference in mean YFP Allele expression of the WT allele containing the control WT allele and the WT allele of the mutant C228T and C250T, respectively. WT displayed significantly lower expression than C228T p <0.0001 and C250T <0.0001. While C228T showed significantly lower expression than C250T <0.0001 (unpaired t-tests). **(E)** scatter plot overlaying the WT, C228T, and C250T allele expression. **(F)** Bar graph showing the allele expression variance for the mCherry allele quantified using the Fano Factor calculation. **(G)** Bar graph showing the allele expression variance for the YFP Allele quantified using the Fano Factor calculation.

Here we investigated cell-to-cell variance in the expression of TPMs against WT cell lines. TPMs are heterozygous and kept in epigenetically distinct allelic states, potentially contributing to increased stochastic gene expression (Stern, Paucek et al. 2017). C250T has the highest expression and variance and the most significant metastatic potential and penetrance

seen in the MetMap study, followed by C228T. Stochastic gene expression has been shown to drive diversity and allow clonal populations to exhibit phenotypic heterogeneity, possibly aiding in metastatic dissemination (Raj and van Oudenaarden 2008, Matak, Lahiri et al. 2018, Kumar, Cramer et al. 2019, Deshmukh and Saini 2020). Although there has not been a strong connection between Telomerase expression and overall survival (Pópulo, Boaventura et al. 2014), the increase in mean expression and variance could be a barrier to effective therapy (Guinn, Wan et al. 2020), which assumes that the population will react homogeneously to the treatment and support the metastatic ability to survive multiple stressors in metastatic dissemination. This may be due partly to Telomerase's non-canonical roles, one of which is protection against reactive oxygen species by translocating to the mitochondria (Ling, Wen et al. 2012). While metastatic melanomas harboring TPMs do not necessarily have long telomeres or active telomere maintenance programs (Viceconte, Dheur et al. 2017), many speculate on other non-canonical roles Telomerase may have, especially in resistant and metastatic tumors.

Machine learned classifiers can discriminate TPMs vs. WT with low false positives

We next investigated multiple cellular measurements beyond the mean intensity and other metrics such as nuclear shape and texture of the phase channel for 290 metrics. These single-cell measurements were used to train interpretable and noninterpretable machine-learned classifier models to discriminate between WT, C228T, and C250T cell lines. Using interpretable methods such as Random Forest, we found the top features related to the expression and variance of the mutant allele, which yielded an overall accuracy of 77.06% **(Fig 3.3A)** with F1 scores of 0.83 for WT, 0.72 for C228T, 0.76 for C250T **(Fig 3.3B)**. Using noninterpretable methods such as a shallow Perceptron Neural Network, we achieved an overall accuracy of 80.64% **(Fig 3.3C)** with F1 scores of 0.83 for WT, 0.76 for C228T 0.82 for C250T **(Fig 3.3D)**. However, when we group the categories as WT vs. TPM (C228T and C250T), our classification accuracy and F1 scores improved. Again, using Random Forest, we found the top features related to the expression of the mutant allele, which yielded an overall accuracy of 87.81% **(Fig 3.3E)** with F1 scores of 0.83 for WT, 0.90 for TPM **(Fig 3.3F)**. Using noninterpretable methods such as a shallow Perceptron Neural Network, we achieved an overall classification accuracy of 86.61% **(Fig 3.3G)** with F1 scores of 0.81 for WT, 0.90 for TPM **(Fig 3.3H)**. Since reducing the multidimensional feature for 2D

visualization for all methods was highly similar, we have included PCA and tSNE plots for the Random Forest models **(Fig 3.3I-L)**. There is a significant overlap between the cell lines in the tSNE and PCA space since there is only a base pair difference between these cell lines. We have shown that the features relating to the mutant allele expression hold the most discriminative power, with low false positives, as seen by the high F1 scores, between the isogenic cell lines in 2D cell culture. However, it is valuable for the community to identify label-free cell features that can be used to discriminate between TPMs and WT cells. Towards this, not only does this allow other genes of interest to be reported with the fluorescent proteins used in this study. Furthermore, identifying biopsy samples for which genetic engineering can be toxic or alter the cell state is highly valuable.

Interrogation of 2D label-free cell features for the discrimination of TPMs and WT cells

As highlighted in Chapter 1, subtle changes in metastatic cell states should manifest themselves in detectable phenotypic changes. This is due to the morphological connection to the cytoskeleton changes necessary for invasion in the metastatic cascade. Cell appearance is a reliable monitor of cell signaling pathways (Bakal, Aach et al. 2007, Yin, Sadok et al. 2013, Goodman and Carpenter 2016, Gordonov, Hwang et al. 2016, Pascual-

Vargas, Cooper et al. 2017, Sero and Bakal 2017, Scheeder, Heigwer et al. 2018) due to the strong connection to the cytoskeleton (Moujaber and Stochaj 2020), which is readout metastatic expression profiles (Nguyen, Yoshida et al. 2016), and a cell's ability to invade (Minn, Kang et al. 2005).

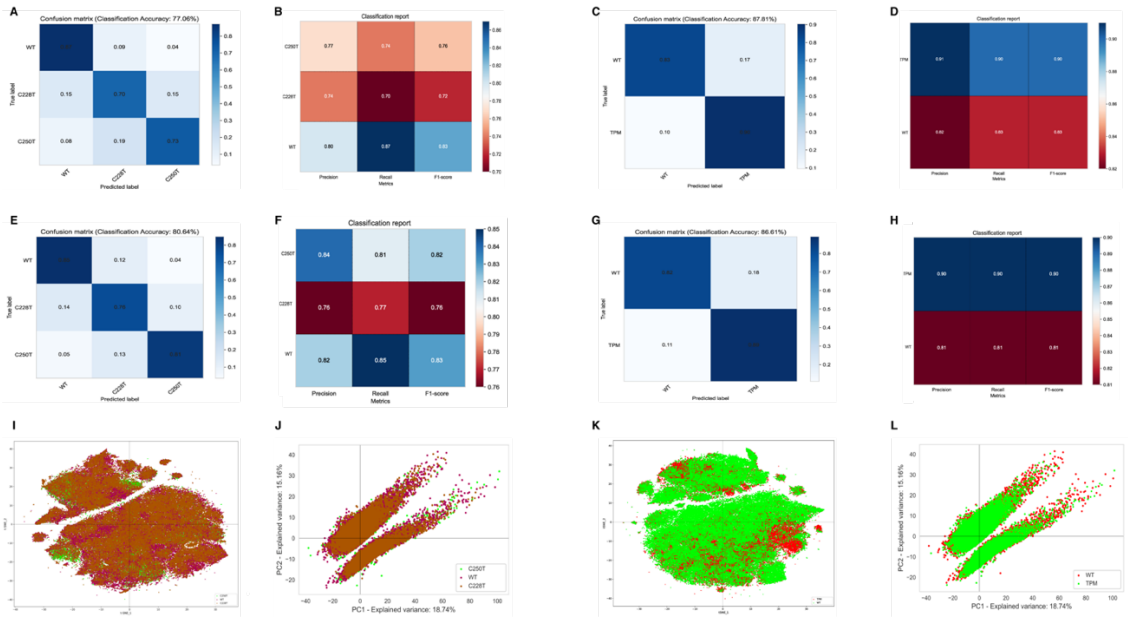

Figure 3.3 Machine learning discriminates between clonal cell lines. Confusion matrix and classification report containing precision, recall, and F1-score for WT vs. C228T vs. C250T using **(A and B)** Random Forest and **(C and D)** Perceptron Neural Net and WT vs. TPM using **(E and F)** Random Forest, and **(G and H)** using Perceptron Neural Net. Dimensionality reduction visualization of the feature sets used in the Random Forest classification model for WT vs. C228T vs. C250T using **(I)** tSNE and **(J)** PCA and WT vs. TPM using **(K)** tSNE and **(L)** PCA.

Recent studies have shown explicitly that cell appearance phenotypes have a solid connection to the metastatic phenotype (Cooper, Sadok et al. 2015, Lyons, Alizadeh et al. 2016, Wu, Gilkes et al. 2020). Morphological changes to identify invasive cancers stem from recognizing

the epithelial to mesenchymal transition (EMT) (Li and Balazsi 2018, Lu and Kang 2019). Increased Telomerase expression has been shown to be connected to EMT (Liu, Li et al. 2013). Not only this, but pathologists often see gross morphological changes from primary to metastatic site biopsy samples, which have long been used for disease staging and grading (Lee, Hodi et al. 2020).

Using two-dimensional (2D) cell culture has taught us the value of cell appearance and its relation to metastatic ability. Recently the role of mechanotransduction's effect on metastasis as readout by 2D cell shape has shown to be an opportunistic avenue to assay metastatic potential (Holenstein, Horvath et al. 2019, Riehl, Kim et al. 2021). Based on these previous works and our work in Chapter 2, we wanted to see the differences in cell appearances between WT and C228T and C250T isogenic cell lines in a typical culture setting. Due to how the cell lines grew in vitro, it was difficult to get whole cell segmentation using phase-contrast images, and our reporters were localized to the nucleus. Therefore, we used the nuclear mask to gather information in the phase-contrast images. Whether in tissue or single cells, previous studies of cancer have exploited light microscopy images using texture metrics to classify parts of the tissues or single cells for

metastatic properties (Kather, Weis et al. 2016, Rahman, Mahanta et al. 2020).

While traditional Haralick Texture features are intensity-based on grayscale coefficient matrix, which can introduce biases due to day to day, well to well, position to position within well variability, we used an updated version of Haralick texture that is intensity invariant (Löfstedt, Brynolfsson et al. 2019), which is based on the original Haralick features (Haralick, Shanmugam et al. 1973), to circumvent these biases. We quantified the Haralick intensity invariant texture features, Haralick Texture statistics of the grayscale matrix, and Local Binary Patterns (Ojala, Pietikainen et al. 1994) of 67,000 single cell phase-contrast images to train machine-learned classifiers. We present the LDA models, which yielded the best classification results for WT vs. TPM classes. We visualized the overlap of features used for LDA classification using the stand deviation of parallel coordinates for Haralick Texture intensity invariant features **(Fig 3.4A)**, Haralick Texture statistics **(Fig 3.4C)**, and Local Binary Patterns **(Fig 3.4E)**. Using LDA classifier we achieved a classification score of 80.6% for TPMs and 34.0% for WT using Haralick Texture intensity invariant features **(Fig 3.4B)**; 83.6% for TPMs and 29.7% for WT using Haralick Texture statistics features **(Fig 3.4D)**; 84.9% for TPMs and 36.4% for WT using Local Binary Patterns **(Fig 3.4F)**. For the LDA models, the receiver operator

curves (ROC) with the area under the curve (AUC) are shown for Haralick Texture intensity invariant features **(Fig 3.4G and H)**, Haralick Texture statistics features **(Fig 3.4I and J)**, and Local Binary Patterns **(Fig 3.4K and L)**. We reduced the dimensionality of each feature set using the t-SNE method **(Fig 3.4M-O)**. We show that using Haralick Texture intensity invariant features; there is significant overlap between the two populations. Haralick Texture statistics features and Local Binary Patterns show greater separation; however, none show a clear separation between the populations. These texture feature differences between the isogenic populations show that the LDA classifier has morphological differences to classify all populations over 50%. While not the best classification results and not nearly enough power for clinical application, there is promise here for classification, albeit not using 2D phase-contrast cell culture images atop plastic dishes. It should be noted that 2D cell culture atop plastic dishes homogenizes cell appearance (Duval, Grover et al. 2017, Kapałczyńska, Kolenda et al. 2018). We noted similar differences between the populations visualized using tSNE with a classification accuracy using LDA. While these results show there is not much difference in cell appearance with the introduction of TPMs in isogenic cell lines, there are multiple background mutations that co-occur with TPMs specific to different cancer types that may yield striking differences in the cell appearance. These results were replicated with more granular labeling

of TPMs into C228T and C250T labels to highlight a loss of classification accuracy. At the same time, the reduced feature space is identical **(Fig 3.5)**.

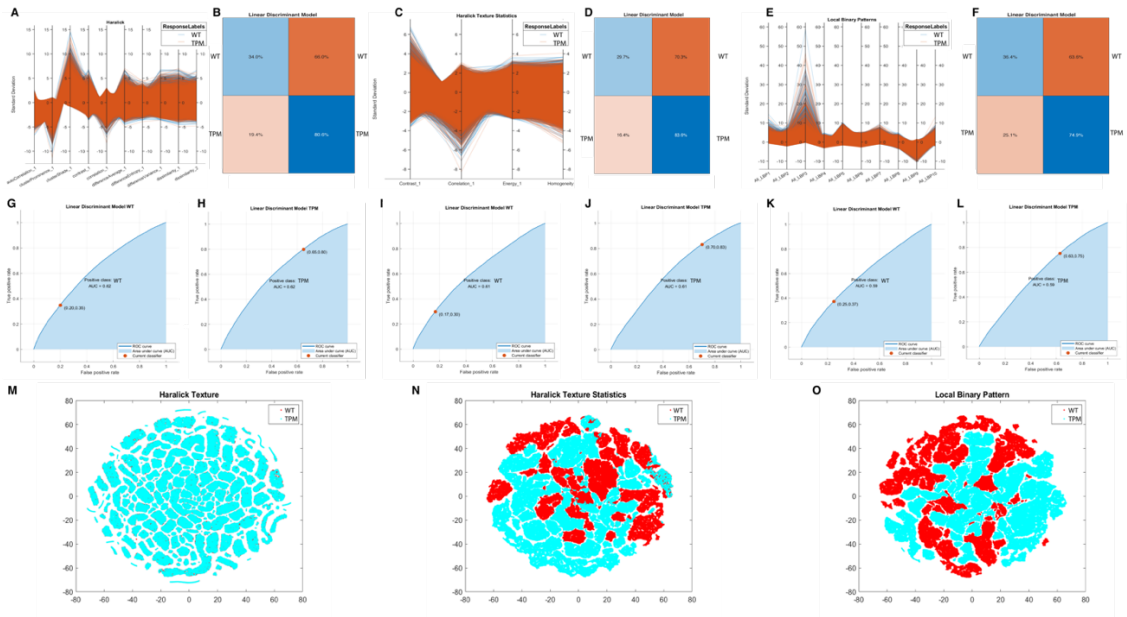

Figure 3.4 Label-free intensity invariant features do not discriminate between clonal cell lines. Linear Discriminant Analysis model **(A)** Parallel coordinates of the standard deviation of computed Haralick features, and **(B)** confusion matrix. **(C)** Parallel coordinates of the standard deviation of computed Haralick statistics features, and **(D)** confusion matrix. **€** Parallel coordinates of the standard deviation of computed Local Binary Patterns and **(F)** confusion matrix. Receiver Operator Curves with Area under the curve for Haralick features of **(G)** WT and **(H)** TPMs; Haralick statistics features **(I)** WT and **(J)** TPMs; and Local Binary Patterns **(K)** WT and **(L)** TPMs. We visualized the dimensionality using t-SNE of **(M)** Haralick Texture, **(N)** Haralick Texture Statistics, and **(O)** Local Binary Patterns.

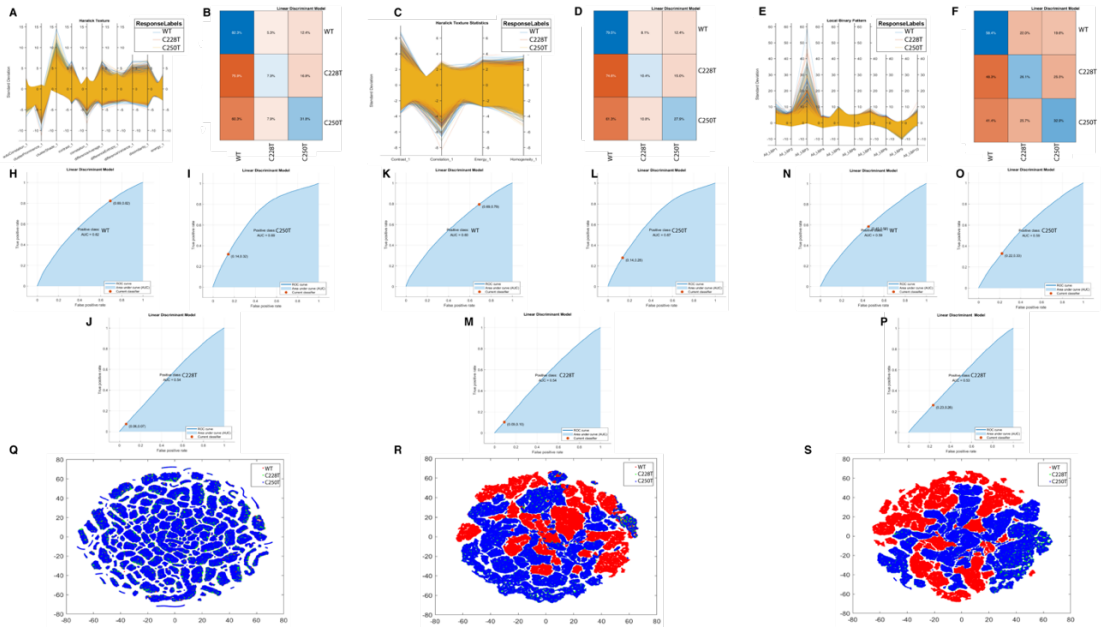

Figure 3.5 Label-free intensity invariant features do not discriminate between WT and TPM cell lines. Linear Discriminant Analysis model **(A)** Parallel coordinates of the standard deviation of computed Haralick features, and **(B)** confusion matrix. **(C)** Parallel coordinates of the standard deviation of computed Haralick statistics features, and **(D)** confusion matrix. **€** Parallel coordinates of the standard deviation of computed Local Binary Patterns and **(F)** confusion matrix. Receiver Operator Curves with Area under the curve for Haralick features of **(G)** WT and **(H)** TPMs; Haralick statistics features **(I)** WT and **(J)** TPMs; and Local Binary Patterns **(K)** WT and **(L)** TPMs. We visualized the dimensionality using t-SNE of **(M)** Haralick Texture, **(N)** Haralick Texture Statistics, and **(O)** Local Binary Patterns.

TPMs are discriminated using label-free images from imaging flow cytometry

The pairing of deep learning and machine learning with different imaging technologies such as Imaging Flow Cytometry (IFC) can interrogate the metastatic stage in primary samples as part of the pathology pipeline. IFC simulates an ex vivo circulating tumor cell (CTCs) environment and may display increased cell appearance changes. Using IFC for label-free imaging has advantages over engineered cells. Given that these samples can be fragile and genetic engineering can perturb the cell state, IFC can probe

the cell using cell light scatter and brightfield images, both of which require no labels and have been used for cancer classification with deep and machine learning (Hennig, Rees et al. 2017, Doan, Vorobjev et al. 2018, Doan, Barnes et al. 2021, Edgar, Tarhini et al. 2021). Here we leverage the power of the ImageStreamX imaging flow cytometry platform and the Amnis AI deep learning software platform, which utilizes a modified U-Net model to identify subtle differences between the TPMs. Here we show that using brightfield images alone; we can discriminate between the three cell lines with high accuracy and probability of predicting the correct class **(Fig 3.6A and B)** with low false positives **(Fig 3.6C)**. We could identify WT cells with 100% precision, 99.68% recall, and 99.84% F1 score, indicating low false positives. Whereas we could identify C228T cells with 86.16% precision, 85.23 % recall, and 85.69% F1-score and C250T with 69.31% precision, 71.04% recall, and 70.16% F1-score. However, we could not discriminate between the cell lines using side light scatter images alone using this model. The normalized probability of correct predicted class confusion matrixes **(Fig 63.D and E)** was low with many false positives, as indicated by the F1-score **(Fig 3.6F)**.

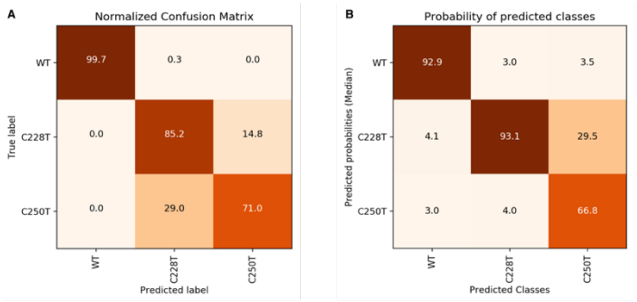

C

Class	Precision (%)	Recall (%)	F1 (%)	Support
WT	100.00	99.68	99.84	5041
C228T	86.16	85.23	85.69	17239
C250T	69.31	71.04	70.16	8096
weighted avg	83.96	83.85	83.90	30376

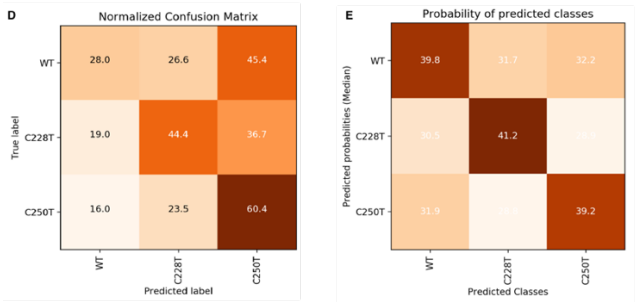

F

Class	Precision (%)	Recall (%)	F1 (%)	Support
WT	37.19	27.95	31.92	11763
C228T	46.35	44.37	45.34	14254
C250T	50.44	60.45	54.99	17794
weighted avg	45.55	46.49	45.66	43811

Figure 3.6 Brightfield and light scatter images discriminate between clonal cell lines using deep neural networks. (A) Normalized confusion matrix of WT vs. C228T vs. C250T using brightfield images. **(B)** The median probability of predicted classes using brightfield images. **(C)** Class-wise metrics of precision, recall, and F1 for brightfield images. **(D)** Normalized confusion matrix of WT vs. C228T vs. C250T using side scatter images. **(F)** The median probability of predicted classes using side scatter images**. €** Class-wise metrics of precision, recall, and F1 for side scatter images.

The future use of this technology and deployment of trained deep learned models can rapidly identify metastatic cell states, which in turn can allow the physician to make treatment decisions, especially for the detection of CTCs in liquid biopsies; CTCs are rare, but metastatic cells would be part of this population. It is imperative to identify cells with TPMs that would potentially colonize a distant organ, as they are highly correlated with the aggressive stage of metastasis and resistance.

TPMs display higher collective migration with monolayer spatiotemporal variations

We next investigated the effect of TPMs have on functional phenotypes such as collective cell migration after wound healing. Wounds are essentially a breach in cells that are typically linked tightly to form a protective barrier that is suddenly separated. Similarly, cells detach from their neighbors in metastasis and adopt a migratory behavior to reach new locations. It is suspected that the wound repair program equips both types of cells to survive this anchorless state Ganesh, K, et al. (2020). This allows cells to move into the breach and make new tissues, enabling metastatic cells to detach and colonize new destinations. Increased Telomerase expression has been shown to promote the epithelial to mesenchymal transition and three-dimensional invasion through Matrigel in vitro (Liu, Li et al. 2013). Additionally, Telomerase and WNT/β-Catenin pathway is connected to invasiveness and stemness in cancer (Fang, Yuan et al. 2018).

Using previously published software, we investigated spatiotemporal dynamics of collective cell migration between the three clonal cell lines via in vitro wound healing (Zaritsky et al., 2015). We first segment each image into cellular (foreground) and background regions and calculate the velocity fields. We then calculate kymographs that capture the experiment's

spatiotemporal dynamics. Next, we extract features vectors from the kymographs and calculate the principal components. The WT cell line had a significantly lower healing rate between C228T and C250T. C250T showed a substantially higher healing rate over C228T **(Fig 3.7A)**. Overall distance migrated showed similar results, with WT having significantly lower distances between C228T and C250T, while C250T migrated further than C228T **(Fig 3.7B)**. We examined the averaged speed and directionality of the kymographs across experiments. We found the speed was significantly lower for WT, while directionality showed no difference between WT and C228T. This differed for WT than C250T, where speed and directionality were substantially higher. C250T showed significantly higher speed and directionality **(Fig 3.7C and D)**. We then investigated the speed in each of the 12 features of the kymographs individually. The 12 features encode acceleration at the wound edge (features 1-4), 60 -12 microns in the wound interior (features 5-8), and spatial variation in migration at later stages (9-12). We found that WT compared to C250T was significantly different in all 12 features and C228T compared to C250T differed significantly in all 12 features for directionality **(Fig 3.7E and F)**. Whereas WT compared C228T showed differences in only 6/12 features. We next examined the speed of each 12 features. WT compared to C228T displayed significant differences in 10/12 features. While WT compared to C250T were significantly different in all 12

features for speed. C228T compared to C250T were statistically different in features 1-6, whereas features 7-12 also had significant differences **(Fig 3.7G and H)**. We have shown that C250T has a considerable advantage in healing rate and overall distance covered in an in vitro wound-healing assay, followed by C228T, while WT is the slowest and covered the least distance.

Furthermore, C250T has considerable spatiotemporal differences in speed and directionality propagating from the wound edge into the monolayer compared to WT and C228T. C228T lags behind C250T in all metrics but is still significantly faster and migrated further, with significant spatiotemporal differences in nearly all 12 features. This follows the same trend seen with allele expression and variance and MetMap differences in the metastatic potential and penetrance.

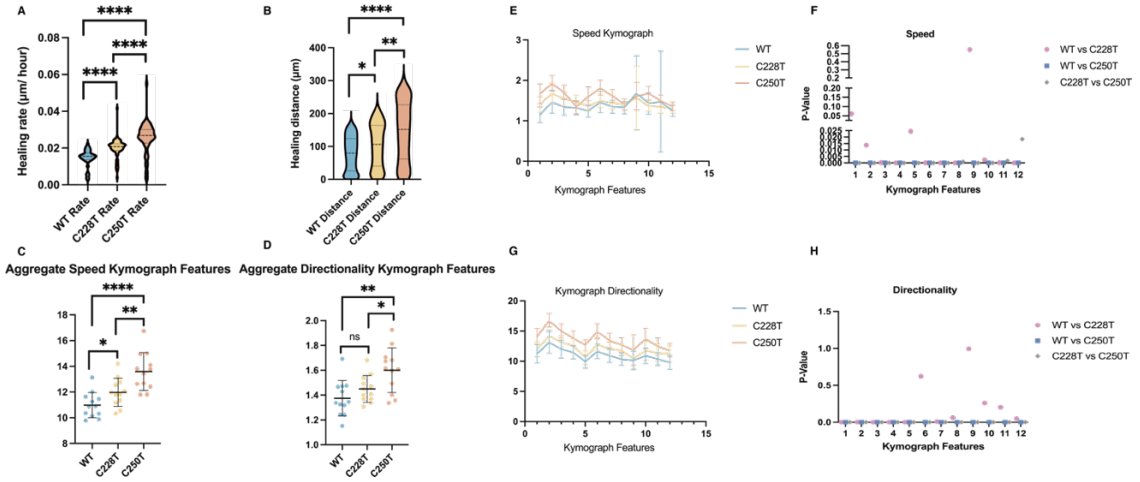

Figure 3.7 C250T increases healing rate, distance, and information propagation from wound edge to interior of monolayer. n = 38 movies for each cell line. **(A)** Violin plot comparison of healing rates across cell lines. WT compared to C228T p <0.0001, WT compared to C250T p <0.0001, and C250T compared to C228T p <0.0001. **(B)** Total distance in microns the leading edge covered throughout the movies. WT compared to C228T p = 0.0175, WT compared to C250T p = 0.0047, and C250T compared to C228T p <0.0001. Aggregate comparisons of the average of each of the 12 kymograph features for all movies across cell lines. **(C)** Speed of each of the 12 averaged figures. WT compared to C228T p = 0.1600, WT compared to C250T p = 0.0036, and C250T compared to C228T p = 0.0332. **(D)** Directionality of each of the 12 averaged figures. WT compared to C228T p = 0.0242, WT compared to C250T p <0.0001, and C250T compared to C228T p = 0.0083. **(E)** Graph showing the speed of individual 12 kymographs features averaged among the 38 movies with SD error bars. **(F)** Graph depicting p-values from multiple Mann-Whitney tests for speed features. WT compared to C228T were significantly different in features 2-8 and 10-12 with p values 0.013734, 0.000344, 0.000010, 0.024413, 0.000085, 0.000010, <0.000001 and 0.002214, 0.000359, and 0.000014 respectively. While features 1 and 9 were not significantly different with p values of 0.061604 and 0.550616, respectively. WT compared to C250T were significantly different in all 12 features, p <0.000001. C228T compared to C250T differed significantly in all features with corresponding p values of <0.000001, <0.000001, <0.000001, 0.000012, <0.000001, <0.000001, 0.000006, 0.000887, 0.000008, 0.000003, 0.001708, 0.018402. **(G)** Graph showing the directionality of individual 12 kymographs features averaged among the 38 movies with SD error bars. **(H)** WT compared to C228T differed significantly in directionality features 1-5, and 7 with p values <0.000001, 0.001646, 0.000027, 0.000670, 0.000093, and 0.008123 respectively. While features 6 and 8-12 were not significantly different with corresponding p values of 0.621746, 0.060135, 0.993789, 0.260206, 0.203475, and 0.048283. WT compared to C250T were significantly different in all 12 features, p <0.000001. C228T compared to C250T differed significantly in all 12 features p <0.000001. All p values from Mann-Whitney tests.

Conclusions

Through the meta-analysis of the MetMap atlas, we found that tumors harboring C250T TPM have more metastatic potential and penetrance in the organs used in the study than tumors bearing the C228T TPM. We then engineered isogenic cell lines harboring either C228T or C250T TPMs on the endogenous locus under the endogenous promoter to dissect the effect TPMs have on metastatic phenotypes in vitro. While monitoring the differential expression using spectrally distinct fluorophores, we found that the C250T TPM increases mean expression and stochastic gene expression variance over C228T TPM. Unexpectedly, the WT allele in the TPM cell lines displayed increased expression. WT alleles in the C250T TPM cell line showed the most increase in expression.

Furthermore, using interpretable and uninterpretable machined learned models using over 200 cell features, we could discriminate between C250T and C228T with high accuracy and low false positives. However, the most discriminative power was grouping TPMs against WT cell lines. This is very promising for identifying cells harboring TPMs in tumors; however, it would be ideal to have label-free, non-genetic engineering fluorescent models to identify cells bearing TPMs.

We investigated differences in the 2D cell appearance of C228T and C250T cells. However, using the 2D cell culture model, we could not discriminate between the TPMs and WT cells. We investigated previously described cell appearance differences between metastatic melanoma biopsies using imaging flow cytometry. We found that using brightfield images and a deeply learned model, we could accurately and with low false positives identify TPMs. This shows the promise of using label-free features to identify cells harboring TPMs in biopsy samples; however, biopsy samples are needed to train a clinically relevant model. This study highlights a pattern where C250T correlates with a more significant increase of various metastatic metrics over the C228T TPM, also increasing over WT. This increase in each phenotype may compound in vivo and relate to the increased metastatic potential and penetrance in our MetMap results.

Methods

Cell culture and origin

HEK293T were ordered from ATCC (ATCC CRL-11268) and tested negative for Mycoplasma using Mycoplasma detection kit (Southern Biotech). HEK293T cells were cultured in Dullbecco minimal essential medium (DMEM: Thermo Scientific HyClone #SH30022FS) supplemented with 10% fetal bovine serum, 4 mM L-glutamine, 100 I.U./ml penicillin and 100 mg/ml streptomycin at 37℃, 5% CO2 and 90% humidity.

Transfection

The transfections were performed with 1 mg DNA: 2 ml Fugene HD (Promega E2311) ratio. Cells were seeded at 300,000 cells/well in six-well plate for 18 hrs before transfection. Two days after transfection puromycin was added to the medium at 1 mg/ml, and cells were selected for 2 days. Survival cells were grown for another 7 days before sorted with FACS into 96-well and expanded into monoclonal cell lines. We plated 300,000 cells/well in 6-well plate overnight. Transfect with 1.25 ug gRNA and 1.25 ug linearized donor with 5 ul FugeneHD in 100 ul final volume in Opti-MEM.

Construct designs and homogenous clonal cell line creation

We followed the CRISPR/Cas9 protocol (Ran et al., 2013) to construct the reporter cell line. In general, the gRNAs were designed by online CRISPR tool (http://crispr.mit.edu) and the DNA oligos were ordered from Eurofins Genomics, annealed and cloned into pSpCas9(BB)□2A-Puro (Addgene #48139) vector plasmids. gRNA plasmids were transfected into HEK293T cells and tested for gRNA efficiency using the T7 endonuclease assay. Only the most efficient gRNA was used with the donor DNA. The donor plasmids were constructed using Gibson assembly method. We used site-directed in-vitro mutagenesis to make synonymous substitution in the donor plasmids to avoid gRNA recognition and Cas9 cutting of the linearized donor DNA. In more detail, we first developed a nuclear marker cell line by inserting the nuclear localization signal followed by two copies of infrared fluorescent protein (NLS-2xiRFP) (Ogrodnik et al., 2014) under the endogenous actin promoter followed by a P2A spacer in HEK293T cells. This cell line ensured a constitutive expression without introducing exogeneous strong constitutive promoter and greatly assisted cell segmentation and tracking. Briefly, the gRNA and the linearized donor DNA were transfected into HEK 293T cells and the transfected cells were screened with 1 mg/ml puromycin for 2 days. The cells were allowed to grow for additional 5 days before sorted by FACS. The fluorescently positive cells were sorted as single cell into 96-well plate. We

collected at least 500 single cells. We grew the cells for additional 3 weeks to obtain homogenous clones. On average, about 30% of cells formed colonies and all were screened for fluorescent signal with the microscope. A minimal of 10 clones were then genotyped and checked for homozygosity and correct integration using at least three pairs of primers and confirmed with sequencing. Positive clones were further validated with western blot to ensure correct protein expression. After construction and validation, the engineered single-clonal cell line was assigned a unique identification number, entered in our electronic data- base, and stored in liquid nitrogen with a cryoprotectant. The same procedure was performed for CRISPR-based tagging the other allele of Telomerase. Cells were screened with puromycin and sorted by FACS to generate monoclonal cell lines.

Flow cytometry and single cell sorting

To create cell populations "cloned" from a single cell, cells were released via trypsinization and passed filtered through a cell strainer (Fischer; 07-201-430), to ensure single-cell solution, cells were resuspended in HBH and analyzed using a benchtop BD FACSAria Fusion flow cytometer (BD Biosciences, Franklin Lakes, NJ). For single cell clone generation of WT and TPM cell lines, were then sorted using Fluorescent Activated Cell Sorting into 96-well plates. Acquired flow cytometry data were all analyzed with FlowJo

software (Tree Star). All cells were gated on FSC, SSC, iRFP, and then mCherry, and YFP taking cells from bulk of the populations and not the outliers. Single cells were identified via phase contrast and fluorescence microscopy. Once confluent within the well, the clonal populations were released via trypsinization inside the well, transferred to individual cell culture dishes, and allowed to expand until confluency.

Live cell imaging

The imaging medium is phenol red free DMEM (Life Technology-Gibco) with the same supplements as the regular culture medium. Live cell phase contrast and fluorescence imaging was performed on a Nikon Ti microscope equipped with an environmental chamber held at 37oC and 5% CO2 in 20x magnification (pixel size of 0.803μm). Cells were seeded in 24-well polystyrene dish in 4 mL of phenol-red free DMEM per dish. The dish was then placed in a 37°C incubator for 24 hours to allow cells to recover from trypsinization before imaging. Snapshot images were taken before time-lapse. Time-lapse imaging was performed for 3-4 days to allow for multiple cell divisions.

Collective cell migration

Cells were grown in a 2-well culture insert until a cell monolayer was established using Phenol-red free DMEM. The insert was removed and 1ml medium was added while monolayer positions were imaged every 10 minutes over 24 hours. Each time-lapse movie was inspected for quality over the 24 hours. If the movie time needed to be cropped due to monolayers colliding, we removed these time frames as to not affect analysis. Code availability is here: (https://github.com/assafZaritskyLab/SpatiotemproalQuantificationMonolayerCellMigrationPipeline). The plots were generated using PRISM 9.

Allele expression quantification

Background correction was performed using ImageJ's Rolling ball background subtraction algorithm with 15-pixel radius (Schneider, Rasband et al. 2012). We took advantage of the popular CellProfiler platform (Stirling, Swain-Bowden et al. 2021) for automated nuclear segmentation using the nuclear marker iRFP reporter, followed by exclusion of non-cell objects by size and shape selection (CellProfiler Pipeline with representative images are attached in Supplemental Figure 2). Cell segmentations were then subject to manual inspection, and segmented objects that did not correspond to cells were then eliminated. For each data set, automated segmentation

parameters were chosen such that the fraction of incorrectly identified cells was minimized.

Imaging flow cytometry acquisition

To image single cells, cells were released via trypsinization and passed filtered through a cell strainer (Fischer; 07-201-430), to ensure single-cell solution, cells were resuspended in HBH and analyzed using a benchtop ImageStream X platform to capture images of live HEK 293T cells. For each cell, we captured images of brightfield and side scatter images. After image acquisition, we used the IDEAS analysis tool (this is software that accompanies the ImageStream X software) to discard multiple cells or debris, omitting them from further analysis. Typical ImageStream settings: Sample volume: 2.6 ml (extracted from the 100 ml loaded). Flow diameter: 7 mm. Velocity of flow: 44 m s 1. Resolution: 0.5 mm. Magnification: 60. Camera sensitivity: 256 on all channels. Camera gain: 1. Brightfield LED intensity: 88 mW. Darkfield laser intensity: 1 mW.

IFC configuration and acquisition

All samples were run on an ImageStream$^{®X}$ Mark II dual CCD camera system (Luminex Corporation, Seattle, WA, USA) at 40X magnification with the 405 nm laser set to 15 mW. For all samples, a data acquisition template

described previously[26] was used to eliminate small and large debris, unfocused imagery events.

Amnis® AI (AAI) software description

The AAI software (v1.0) uses the Keras Application Programming Interface version 2.1.5 with TensorFlow version 1.7.0 library. The convolutional neural network (CNN) architecture used for training and classification is pre-configured based on the VGG16 network to work optimally on image data acquired on Amnis® IFCs. All pixel values in each image are normalized to the range [0 1]. Once the ground truth data has been populated, the AAI software splits the data into training, validation, and test sets using an 80/10/10 ratio – the validation and test data sets are never seen by the CNN during training. Class balancing and data augmentation are also performed to control classification bias and enhance the robustness of trained models.

Quantification and statistical analysis of Metastatic potential and penetrance

TPM status was determined by the mining of cell databases and primary papers. Plots were made in PRISM 9®.

General Image Analysis

All computations were performed on an AMD Ryzen 5 3600 CPU @ 4.1 GHz machine with an NVIDIA® RTX® 3060 GPU running Windows 10 Professional. This machine was built as a moderate machine/deep learning workstation that is accessible to most research and clinical budgets.

Author contributions

Andres Nevarez, Conceptualization, Formal analysis, Investigation, Methodology, Funding acquisition, Writing - original draft, Writing - review and editing; Anusorn Mudla- Cell line creation; Yishaia Zabary Migration Analysis Developement; Nan Hao, Conceptualization, Resources, Formal analysis, Supervision, Funding acquisition, Investigation, Methodology, Writing - original draft, Project administration, Writing - review and editing

Acknowledgments

Chapter 3, in part is currently being prepared for submission for publication of the material. Nevarez, Andres; Mudla, Anusorn; Zabary, Yishaia; Hao, Nan. The dissertation author was the primary investigator and author of this material.

Author ORCIDs

Andres Nevarez https://orcid.org/0000-0002-8337-6454

Anusorn Mudla https://orcid.org/0000-0003-1132-2307

Yishaia Zabary https://orcid.org/0000-0002-9029-4115

Nan Hao https://orcid.org/0000-0003-2857-4789

References

Bakal, C., J. Aach, G. Church and N. Perrimon (2007). "Quantitative morphological signatures define local signaling networks regulating cell morphology." science **316**(5832): 1753-1756.

Bell, R. J., H. T. Rube, A. Kreig, A. Mancini, S. D. Fouse, R. P. Nagarajan, S. Choi, C. Hong, D. He and M. Pekmezci (2015). "The transcription factor GABP selectively binds and activates the mutant TERT promoter in cancer." Science **348**(6238): 1036-1039.

Bogenrieder, T. and M. Herlyn (2003). "Axis of evil: molecular mechanisms of cancer metastasis." Oncogene **22**(42): 6524-6536.

Ceccarelli, M., F. P. Barthel, T. M. Malta, T. S. Sabedot, S. R. Salama, B. A. Murray, O. Morozova, Y. Newton, A. Radenbaugh and S. M. Pagnotta (2016). "Molecular profiling reveals biologically discrete subsets and pathways of progression in diffuse glioma." Cell **164**(3): 550-563.

Chiang, A. C. and J. Massagué (2008). "Molecular basis of metastasis." New England Journal of Medicine **359**(26): 2814-2823.

Chiba, K., F. K. Lorbeer, A. H. Shain, D. T. McSwiggen, E. Schruf, A. Oh, J. Ryu, X. Darzacq, B. C. Bastian and D. Hockemeyer (2017). "Mutations in the promoter of the telomerase gene TERT contribute to tumorigenesis by a two-step mechanism." Science **357**(6358): 1416-1420.

Cooper, S., A. Sadok, V. Bousgouni and C. Bakal (2015). "Apolar and polar transitions drive the conversion between amoeboid and mesenchymal shapes in melanoma cells." Molecular biology of the cell **26**(22): 4163-4170.

Deshmukh, S. and S. Saini (2020). "Phenotypic Heterogeneity in Tumor Progression, and Its Possible Role in the Onset of Cancer." Frontiers in Genetics **11**.

Dillekås, H., R. Demicheli, I. Ardoino, S. A. Jensen, E. Biganzoli and O. Straume (2016). "The recurrence pattern following delayed breast reconstruction after mastectomy for breast cancer suggests a systemic effect of surgery on occult dormant micrometastases." Breast cancer research and treatment **158**(1): 169-178.

Doan, M., C. Barnes, C. McQuin, J. C. Caicedo, A. Goodman, A. E. Carpenter and P. Rees (2021). "Deepometry, a framework for applying supervised and weakly supervised deep learning to imaging cytometry." Nature Protocols **16**(7): 3572-3595.

Doan, M., I. Vorobjev, P. Rees, A. Filby, O. Wolkenhauer, A. E. Goldfeld, J. Lieberman, N. Barteneva, A. E. Carpenter and H. Hennig (2018). "Diagnostic Potential of Imaging Flow Cytometry." Trends in Biotechnology **36**(7): 649-652.

Duval, K., H. Grover, L.-H. Han, Y. Mou, A. F. Pegoraro, J. Fredberg and Z. Chen (2017). "Modeling physiological events in 2D vs. 3D cell culture." Physiology **32**(4): 266-277.

Edgar, R. H., A. Tarhini, C. Sander, M. E. Sanders, J. L. Cook and J. A. Viator (2021). "Predicting Metastasis in Melanoma by Enumerating Circulating Tumor Cells Using Photoacoustic Flow Cytometry." Lasers Surg Med **53**(4): 578-586.

Eggermont, A. M., A. Spatz and C. Robert (2014). "Cutaneous melanoma." The Lancet **383**(9919): 816-827.

Fang, Y., Y. Yuan, L.-L. Zhang, J.-W. Lu, J.-F. Feng and S.-N. Hu (2018). "Downregulated GBX2 gene suppresses proliferation, invasion and angiogenesis of breast cancer cells through inhibiting the Wnt/β-catenin signaling pathway." Cancer Biomarkers **23**: 405-418.

Fares, J., M. Y. Fares, H. H. Khachfe, H. A. Salhab and Y. Fares (2020). "Molecular principles of metastasis: a hallmark of cancer revisited." Signal Transduction and Targeted Therapy **5**(1): 28.

Goodman, A. and A. E. Carpenter (2016). "High-throughput, automated image processing for large-scale fluorescence microscopy experiments." Microscopy and Microanalysis **22**(S3): 538-539.

Gordonov, S., M. K. Hwang, A. Wells, F. B. Gertler, D. A. Lauffenburger and M. Bathe (2016). "Time series modeling of live-cell shape dynamics for image-based phenotypic profiling." Integrative Biology **8**(1): 73-90.

Griewank, K. G., R. Murali, J. A. Puig-Butille, B. Schilling, E. Livingstone, M. Potrony, C. Carrera, T. Schimming, I. Möller and M. Schwamborn (2014). "TERT promoter mutation status as an independent prognostic factor in cutaneous melanoma." JNCI: Journal of the National Cancer Institute **106**(9).

Guinn, M. T., Y. Wan, S. Levovitz, D. Yang, M. R. Rosner and G. Balázsi (2020). "Observation and Control of Gene Expression Noise: Barrier Crossing Analogies Between Drug Resistance and Metastasis." Frontiers in Genetics **11**.

Gupta, G. P. and J. Massagué (2006). "Cancer metastasis: building a framework." Cell **127**(4): 679-695.

Hafezi, F. and D. Perez Bercoff (2020). "The Solo Play of TERT Promoter Mutations." Cells **9**(3): 749.

Hanahan, D. and R. A. Weinberg (2011). "Hallmarks of cancer: the next generation." cell **144**(5): 646-674.

Haralick, R. M., K. Shanmugam and I. H. Dinstein (1973). "Textural features for image classification." IEEE Transactions on systems, man, and cybernetics(6): 610-621.

Hayward, N. K., J. S. Wilmott, N. Waddell, P. A. Johansson, M. A. Field, K. Nones, A.-M. Patch, H. Kakavand, L. B. Alexandrov and H. Burke (2017).

"Whole-genome landscapes of major melanoma subtypes." Nature **545**(7653): 175-180.

Heidenreich, B., P. S. Rachakonda, K. Hemminki and R. Kumar (2014). "TERT promoter mutations in cancer development." Curr Opin Genet Dev **24**: 30-37.

Hennig, H., P. Rees, T. Blasi, L. Kamentsky, J. Hung, D. Dao, A. E. Carpenter and A. Filby (2017). "An open-source solution for advanced imaging flow cytometry data analysis using machine learning." Methods **112**: 201-210.

Holenstein, C. N., A. Horvath, B. Schär, A. D. Schoenenberger, M. Bollhalder, N. Goedecke, G. Bartalena, O. Otto, M. Herbig, J. Guck, D. A. Müller, J. G. Snedeker and U. Silvan (2019). "The relationship between metastatic potential and in vitro mechanical properties of osteosarcoma cells." Molecular Biology of the Cell **30**(7): 887-898.

Horn, S., A. Figl, P. S. Rachakonda, C. Fischer, A. Sucker, A. Gast, S. Kadel, I. Moll, E. Nagore, K. Hemminki, D. Schadendorf and R. Kumar (2013). "TERT promoter mutations in familial and sporadic melanoma." Science **339**(6122): 959-961.

Huang, F. W., E. Hodis, M. J. Xu, G. V. Kryukov, L. Chin and L. A. Garraway (2013). "Highly Recurrent TERT Promoter Mutations in Human Melanoma." Science **339**(6122): 957-959.

Huang, J., Y. X. Bai, S. W. Han, S. S. Ng, D. D. Jing, B. C. Wong, C. F. Huang, H. F. Kung and M. C. Lin (2003). "A human TERT C-terminal polypeptide sensitizes HeLa cells to H2O2-induced senescence without affecting telomerase enzymatic activity." Biochem Biophys Res Commun **301**(3): 627-632.

Hugdahl, E., M. B. Kalvenes, M. Mannelqvist, R. G. Ladstein and L. A. Akslen (2018). "Prognostic impact and concordance of TERT promoter mutation and protein expression in matched primary and metastatic cutaneous melanoma." British journal of cancer **118**(1): 98-105.

Kapałczyńska, M., T. Kolenda, W. Przybyła, M. Zajączkowska, A. Teresiak, V. Filas, M. Ibbs, R. Bliźniak, Ł. Łuczewski and K. Lamperska (2018). "2D and 3D cell cultures–a comparison of different types of cancer cell cultures." Archives of medical science: AMS **14**(4): 910.

Kather, J. N., C.-A. Weis, F. Bianconi, S. M. Melchers, L. R. Schad, T. Gaiser, A. Marx and F. G. Zöllner (2016). "Multi-class texture analysis in colorectal cancer histology." Scientific Reports **6**(1): 27988.

Kim, N. W., M. A. Piatyszek, K. R. Prowse, C. B. Harley, M. D. West, P. L. Ho, G. M. Coviello, W. E. Wright, S. L. Weinrich and J. W. Shay (1994). "Specific association of human telomerase activity with immortal cells and cancer." Science **266**(5193): 2011-2015.

Kumar, N., G. M. Cramer, S. A. Z. Dahaj, B. Sundaram, J. P. Celli and R. V. Kulkarni (2019). "Stochastic modeling of phenotypic switching and chemoresistance in cancer cell populations." Scientific Reports **9**(1): 10845.

Lee, A. H., Z. Hodi, I. Soomro, V. Sovani, A. Abbas, E. Rakha and I. O. Ellis (2020). "Histological clues to the diagnosis of metastasis to the breast from extramammary malignancies." Histopathology **77**(2): 303-313.

Li, C. and G. Balazsi (2018). "A landscape view on the interplay between EMT and cancer metastasis." npj Systems Biology and Applications **4**(1): 34.
Ling, X., L. Wen and Y. Zhou (2012). "Role of Mitochondrial Translocation of Telomerase in Hepatocellular Carcinoma Cells with Multidrug Resistance." International Journal of Medical Sciences **9**(7): 545-554.

Liu, Z., Q. Li, K. Li, L. Chen, W. Li, M. Hou, T. Liu, J. Yang, C. Lindvall, M. Björkholm, J. Jia and D. Xu (2013). "Telomerase reverse transcriptase promotes epithelial–mesenchymal transition and stem cell-like traits in cancer cells." Oncogene **32**(36): 4203-4213.

Löfstedt, T., P. Brynolfsson, T. Asklund, T. Nyholm and A. Garpebring (2019). "Gray-level invariant Haralick texture features." PLOS ONE **14**(2): e0212110.
Lu, W. and Y. Kang (2019). "Epithelial-Mesenchymal Plasticity in Cancer Progression and Metastasis." Dev Cell **49**(3): 361-374.

Lyons, S. M., E. Alizadeh, J. Mannheimer, K. Schuamberg, J. Castle, B. Schroder, P. Turk, D. Thamm and A. Prasad (2016). "Changes in cell shape are correlated with metastatic potential in murine and human osteosarcomas." Biology open **5**(3): 289-299.

Matak, A., P. Lahiri, E. Ford, D. Pabst, K. Kashofer, D. Stellas, D. Thanos and K. Zatloukal (2018). "Stochastic phenotype switching leads to intratumor heterogeneity in human liver cancer." Hepatology **68**(3): 933-948.

Minn, A. J., Y. Kang, I. Serganova, G. P. Gupta, D. D. Giri, M. Doubrovin, V. Ponomarev, W. L. Gerald, R. Blasberg and J. Massagué (2005). "Distinct organ-specific metastatic potential of individual breast cancer cells and primary tumors." The Journal of clinical investigation **115**(1): 44-55.

Moujaber, O. and U. Stochaj (2020). "The Cytoskeleton as Regulator of Cell Signaling Pathways." Trends Biochem Sci **45**(2): 96-107.

Nagore, E., B. Heidenreich, S. Rachakonda, Z. Garcia-Casado, C. Requena, V. Soriano, C. Frank, V. Traves, E. Quecedo and J. Sanjuan-Gimenez (2016). "TERT promoter mutations in melanoma survival." International journal of cancer **139**(1): 75-84.

Nguyen, A., M. Yoshida, H. Goodarzi and S. F. Tavazoie (2016). "Highly variable cancer subpopulations that exhibit enhanced transcriptome variability and metastatic fitness." Nature communications **7**(1): 1-13.
Ojala, T., M. Pietikainen and D. Harwood (1994). Performance evaluation of texture measures with classification based on Kullback discrimination of distributions. Proceedings of 12th International Conference on Pattern Recognition.

Pascual-Vargas, P., S. Cooper, J. Sero, V. Bousgouni, M. Arias-Garcia and C. Bakal (2017). "RNAi screens for Rho GTPase regulators of cell shape and YAP/TAZ localisation in triple negative breast cancer." Scientific data **4**(1): 1-13.

Pópulo, H., P. Boaventura, J. Vinagre, R. Batista, A. Mendes, R. Caldas, J. Pardal, F. Azevedo, M. Honavar and I. Guimaraes (2014). "TERT promoter mutations in skin cancer: the effects of sun exposure and X-irradiation." Journal of Investigative Dermatology **134**(8): 2251-2257.

Quinodoz, S. A., N. Ollikainen, B. Tabak, A. Palla, J. M. Schmidt, E. Detmar, M. M. Lai, A. A. Shishkin, P. Bhat, Y. Takei, V. Trinh, E. Aznauryan, P. Russell, C. Cheng, M. Jovanovic, A. Chow, L. Cai, P. McDonel, M. Garber and M. Guttman (2018). "Higher-Order Inter-chromosomal Hubs Shape 3D Genome Organization in the Nucleus." Cell **174**(3): 744-757.e724.

Rahman, T. Y., L. B. Mahanta, H. Choudhury, A. K. Das and J. D. Sarma (2020). "Study of morphological and textural features for classification of oral squamous cell carcinoma by traditional machine learning techniques." Cancer Reports **3**(6): e1293.

Raj, A. and A. van Oudenaarden (2008). "Nature, nurture, or chance: stochastic gene expression and its consequences." Cell **135**(2): 216-226.
Reddy, B. Y., P. K. Lim, K. Silverio, S. A. Patel, B. W. Won and P. Rameshwar (2012). "The microenvironmental effect in the progression, metastasis, and dormancy of breast cancer: a model system within bone marrow." International journal of breast cancer **2012**.

Riehl, B. D., E. Kim, T. Bouzid and J. Y. Lim (2021). "The Role of Microenvironmental Cues and Mechanical Loading Milieus in Breast Cancer Cell Progression and Metastasis." Frontiers in Bioengineering and Biotechnology **8**.

Sanchez, A., H. G. Garcia, D. Jones, R. Phillips and J. Kondev (2011). "Effect of Promoter Architecture on the Cell-to-Cell Variability in Gene Expression." PLOS Computational Biology **7**(3): e1001100.

Scheeder, C., F. Heigwer and M. Boutros (2018). "Machine learning and image-based profiling in drug discovery." Current opinion in systems biology **10**: 43-52.

Sero, J. E. and C. Bakal (2017). "Multiparametric analysis of cell shape demonstrates that β-PIX directly couples YAP activation to extracellular matrix adhesion." Cell systems **4**(1): 84-96. e86.

Shain, A. H., I. Yeh, I. Kovalyshyn, A. Sriharan, E. Talevich, A. Gagnon, R. Dummer, J. North, L. Pincus and B. Ruben (2015). "The genetic evolution of melanoma from precursor lesions." New England Journal of Medicine **373**(20): 1926-1936.

Stern, J. L., R. D. Paucek, F. W. Huang, M. Ghandi, R. Nwumeh, J. C. Costello and T. R. Cech (2017). "Allele-Specific DNA Methylation and Its Interplay with Repressive Histone Marks at Promoter-Mutant TERT Genes." Cell Reports **21**(13): 3700-3707.

Torrecilla, S., D. Sia, A. N. Harrington, Z. Zhang, L. Cabellos, H. Cornella, A. Moeini, G. Camprecios, W.-Q. Leow and M. I. Fiel (2017). "Trunk mutational events present minimal intra-and inter-tumoral heterogeneity in hepatocellular carcinoma." Journal of hepatology **67**(6): 1222-1231.
Tracey, E. H. and A. Vij (2019). "Updates in Melanoma." Dermatologic Clinics **37**(1): 73-82.

Viceconte, N., M. S. Dheur, E. Majerova, C. E. Pierreux, J. F. Baurain, N. van Baren and A. Decottignies (2017). "Highly Aggressive Metastatic Melanoma Cells Unable to Maintain Telomere Length." Cell Rep **19**(12): 2529-2543.

Wu, P.-H., D. M. Gilkes, J. M. Phillip, A. Narkar, T. W.-T. Cheng, J. Marchand, M.-H. Lee, R. Li and D. Wirtz (2020). "Single-cell morphology encodes metastatic potential." Science advances **6**(4): eaaw6938.

Yin, Z., A. Sadok, H. Sailem, A. McCarthy, X. Xia, F. Li, M. A. Garcia, L. Evans, A. R. Barr and N. Perrimon (2013). "A screen for morphological complexity identifies regulators of switch-like transitions between discrete cell shapes." Nature cell biology **15**(7): 860-871.